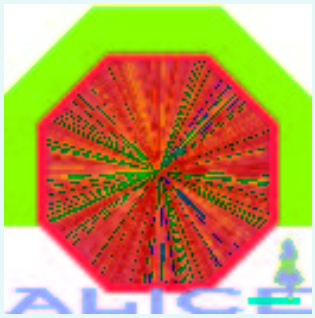

CERN/LHCC 99-13
LHCC/P3-Addendum 2
7 May 1999

A Transition Radiation Detector

for

Electron Identification

within the ALICE Central Detector

ADDENDUM to ALICE PROPOSAL

CERN/LHCC 99-13

LHCC/P3-Addendum 2

7 May 1999

A Transition Radiation Detector

for

Electron Identification within the ALICE Central Detector

ADDENDUM to ALICE PROPOSAL

ALICE Collaboration

Alessandria, Italy, Facoltà di Scienze dell'Università:
G. Dellacasa, L. Ramello, E. Scalas, M. Sitta and C. Soave.

Aligarh, India, Physics Department, Aligarh Muslim University:
N. Ahmad, S. Ahmad, T. Ahmad, W. Baritak, M. Irfan and M. Zafar.

Athens, Greece, Nuclear and Particle Physics Division, University of Athens:
A.L.S. Angelis, A. Kapogiannis, G. Mavromanolakis and A.D. Panagiotou.

Athens, Greece, Institute of Nuclear Physics, NRC Demokritos:
K. Kalfas.

Bari, Italy, Dipartimento di Fisica dell'Università and Sezione INFN:
N. Colonna, D. Cozza, D. Dell'Olio, D. Di Bari, D. Elia, R.A. Fini, B. Ghidini, V. Lenti, L. Liberti, R. Loconsole, V. Manzari, E. Nappi[1)], F. Navach, F. Posa, S. Stucchi and G. Tomasicchio.

Bari, Italy, Politecnico and Sezione INFN:
F. Corsi, D. De Venuto, M. Di Ciano, R. Dinapoli, G. Gramegna, A. Grimaldi, P. Lamanna, C. Marzocca, G. Matarrese and E. Monno.

Beijing, China, China Institute of Atomic Energy:
H. Guo, X. Li, S. Lu, Z. Lu, B. Sa, H. Wang, J. Zhou, S. Zhou and X. Zhu.

Bergen, Norway, Department of Physics, University of Bergen:
H. Helstrup, A. Klovning, O.A. Maeland, O.H. Odland, D. Röhrich, R. Rongved and T.F. Thorsteinsen.

Bhubaneswar, India, Institute of Physics:
A.K. Dubey, D.P. Mahapatra and S.C. Phatak.

Birmingham, United Kingdom, School of Physics and Space Research, University of Birmingham:
I.J. Bloodworth, D. Evans, G.T. Jones, P. Jovanović, J.B. Kinson, A. Kirk, O. Villalobos Baillie and M.F. Votruba.

Bologna-Salerno, Italy, University/INFN:
F. Anselmo, P. Antonioli, G. Bari, M. Basile, L. Bellagamba, D. Boscherini, L. Brocco, A. Bruni, G. Bruni, G. Cara Romeo, D. Casadei, E. Cerron, L. Cifarelli, F. Cindolo, N. Coppola, M. Corradi, B. Cozzoni, A. De Caro, S. De Pasquale, P. Giusti, B. Guasina, D. Hatzifotiadou, N.Y. Kim, G. Laurenti, A. Lavorato, M.L. Luvisetto, A. Margotti, T. Massam, D. Migani, R. Nania, F. Palmonari, A. Pesci, F. Pierella, A. Polini, J. Quartieri, G. Sartorelli, A. Seganti, A. Semek, G. Valenti, D. Vicinanza, M.C.S. Williams and A. Zichichi.

Bratislava, Slovakia, Faculty of Mathematics and Physics, Comenius University:
J. Braciník, V. Černý, J. Ftáčnik, V. Hlinka, M. Ivanov, R. Janik, R. Lietava, M. Pikna, J. Pišút, N. Pišútová, B. Sitar, P. Strmeň and I. Szarka.

Bucharest, Romania, National Institute for Physics and Nuclear Engineering:
A. Andronic, V. Catanescu, M. Ciobanu, M. Dorin, M. Duma, M. Petrovici, V. Simion, C. Staii and G. Stoicea.

Budapest, Hungary, KFKI Research Institute for Particle and Nuclear Physics, Hungarian Academy of Sciences:
E. Denes, B. Eged, Z. Fodor, G. Harangozo, T. Kiss, G. Palla, G. Rubin, J. Sulyan, L. Szendrey, J. Sziklai, D.L. Tarjan, Z. Varga, B.N. Vissy and J. Zimanyi.

Cagliari, Italy, Dipartimento di Fisica dell'Università and Sezione INFN:
C. Cicalo, A. De Falco, M.P. Macciotta-Serpi, A. Masoni, S. Mauro, G. Puddu, P. Randaccio, S. Serci, E. Siddi and G. Usai.

Calcutta, India, Saha Institute of Nuclear Physics:
P. Bhattacharya, S. Bose, Sukalyan Chattopadhyay, N. Majumdar, A. Sanyal, S. Sarkar, P. Sen, S.K. Sen and B.C. Sinha.

Calcutta, India, Variable Energy Cyclotron Centre:
Subhasis Chattopadhyay, M.R. Dutta Majumdar, M.S. Ganti, T.K. Nayak, R.N. Singaraju, M.D. Trivedi and Y.P. Viyogi.

Catania, Italy, Dipartimento di Fisica dell'Università and Sezione INFN:
A. Badalà, R. Barbera, U. Becciani, C. Caligiore, M. Gulino, S. Ingrassia, A. Insolia, F. Librizzi, D. Lo Presti, D. Nicotra, A. Palmeri, S. Panebianco, G.S. Pappalardo, L. Pappalardo, C. Petta, N. Randazzo, S. Reito, F. Riggi, A.C. Russo, G.V. Russo, M. Russo, G. Saccà and A. Sciuto.

CERN, Switzerland, European Laboratory for Particle Physics:
J. Bächler, A. Bajeli[2)], J.A. Belikov[3)], V. Berejnoi[4)], J.-C. Berset, R. Brun, M. Burns, J. Buytaert, M. Campbell, E. Cantatore, W. Carena, F. Carminati, J. Christiansen, D. Collados, C. D'Ambrosio, M. Davenport, J. de Groot, A. Di Mauro, R. Divià, C. Eisenberg, C. Engster, J. Espirito Santo, M. Fageda, H.G. Fischer, M. Flammier, F. Formenti, D. Fraissard, E. Futo[5)], E. Gaumann, M. Goossens, B. Goret, T. Grassi, C. Gregory, M. Hoch, P.G. Innocenti, A. Jacholkowski, W. Klempt, A. Kluge, K. Knudson, G. Lecoeur, J.C. Legrand, L. Leistam, P. Lenoir, Y. Lesenechal, C. Lourenço, A. Malinine, P. Martinengo, M. Mast, T. Meyer, H. Milcent, R. Monnin, M. Morel, A. Morsch, M. Mota, L. Musa, B. Perrin, L. Pigni, F. Piuz, E. Quercigh, J. Raynaud, H. Renshall, A. Rivetti, K. Šafařík, J.-C. Santiard, J. Schukraft, E. Schyns, W. Snoeys, P. Sonderegger, M. Spegel, D. Swoboda, P. Szymanski, G. Tabary, J. van Beelen, H. van der Velde, P. Vande Vyvre, A. Vascotto, D. Vranic, S. Wenig, P. Wertelaers, T. Williams and K. Zelazowski.

Chandigarh, India, Physics Department, Panjab University:
M.M. Aggarwal, A.K. Bhatia, V.S. Bhatia, R. Chugh and V. Vashisht.

Clermont-Ferrand, France, Université Blaise Pascal and IN2P3:
J.P. Alard, A. Baldit, N. Bastid, G. Blanchard, M. Brossard, J. Castor, T. Chambon, P. Crochet, F. Daudon, A. Devaux, P. Dupieux, B. Espagnon, J. Fargeix, P. Force, L. Lamoine, F. Manso, S. Mayade, V. Ramillien, G. Roche, O. Roig, L. Royer, P. Saturnini and G. Savinel.

Coimbra, Portugal, Departamento de Física, Faculdade de Ciências e Tecnologia:
R. Ferreira Marques, P. Fonte[1)] and A. Policarpo.

Columbus, U.S.A., Department of Physics, Ohio State University:
T.J. Humanic, M. Lisa, G. Lo Curto, B.S. Nilsen, G. Paić, D.M. Reichhold and E. Sugarbaker.

Copenhagen, Denmark, Niels Bohr Institute:
I. Bearden, H. Bøggild, J. Gaardhøje and B. Nielsen.

Cracow, Poland, Henryk Niewodniczanski Institute of Nuclear Physics, High Energy Physics Department:
J. Bartke, E. Gładysz-Dziaduś, E. Górnicki, M. Kowalski, A. Rybicki, P. Stefański and Z. Wlodarczyk[6)].

Darmstadt, Germany, Gesellschaft für Schwerionenforschung (GSI):
A. Andronic, R. Averbeck, C. Blume, P. Braun-Munzinger, A. Deusser, A. Devismes, J. Eschke, P. Foka, C. Garabatos, B. Kolb, J. Lühning, U. Lynen, A.M. Marin, D. Miskowiec, W.F.J. Müller, C. Neyer, A. Sandoval, H. Sann, H.R. Schmidt, H. Stelzer, W. von Rüden and A. Wörner.

Frankfurt, Germany, Institut für Kernphysik, Johann-Wolfgang Göthe Universität:
C. Bormann, P. Buncic, M. Gaździcki, J. Günther, S. Lange, R. Renfordt, G. Roland, R. Stock and H. Ströbele.

Gatchina, Russia, St. Petersburg Nuclear Physics Institute:
V. Guersenchtein, B. Komkov, V. Mylnikov, V. Nikouline, V. Samsonov, S. Volkov and A. Vorobiev.

Heidelberg, Germany, Max-Planck-Institut für Kernphysik:
F. Ceretto, C. Fuchs, J. Rak and J.P. Wurm.

Heidelberg, Germany, Institut für Hochenergiephysik, Ruprecht-Karls Universität:
F.O. Lesser, V. Lindenstruth and A.G.E. Mass.

Heidelberg, Germany, Physikalisches Institut, Ruprecht-Karls Universität:
H. Appelshäuser, S. Esumi, K. Filimonov, P. Glässel, B. Lenkeit, N. Herrmann, M.J. Richter, W. Schmitz, J. Stachel, H. Tilsner, J.P. Wessels, T. Wienold and B. Windelband.

Ioannina, Greece, University of Ioannina, Department of Physics:
X. Aslanoglou.

Jaipur, India, Physics Department, University of Rajasthan:
A. Bharti, S.K. Gupta, R. Raniwala and S. Raniwala.

Jammu, India, Physics Department, Jammu University:
S.K. Badyal, A. Bhasin, A. Gupta, V.K. Gupta, L.K. Mangotra, B.V.K.S. Potukuchi, N.K. Rao and S.S. Sambyal.

JINR, Russia, Joint Institute for Nuclear Research:
P.G. Akichine, V.A. Arefiev, V.I. Astakhov, A.A. Baldine, A.M. Baldine, V.D. Bartenev, B.V. Batiounia, I.V. Boguslavsky, M. Bondila, Z.V. Borissovskaia, P. Bylinkine, A.V. Chabounov, G.S. Chabratova, I.A. Chichov, V. Danilov, V.I. Datskov, V.K. Dodokhov, L.G. Efimov, A.G. Fedounov, O.A. Golubitsky, B.N. Guouskov, O.I. Iouldachev, V.G. Kadychevsky, I.E. Karpunina, A.D. Kovalenko, A. Lioubimtsev, V.L. Lioubochits, V.I. Lobanov, G.I. Lykasov, E.A. Matiouchevski, K.V. Mikhailov, D.P. Mikhalev, I. Minaev, P.V. Nomokonov, A.N. Parfenov, I.V. Pouzynin, V.N. Pozdnyakov, A.B. Sadovski, S.V. Semashko, A.E. Senner, I.A. Shelaev, A.V. Sidorov, N.V. Slavine, R.V. Slepnev, G.P. Tsvineva, A.S. Vodopianov, M.B. Yuldasheva, S. Zaporozhets and A.I. Zintchenko.

V. Diomkin[7)], V. Kuznetsov[7)], V. Shestakov[7)], A. Vasiliev[7)] and A. Zhakovksy[7)].

Ts. Baatar[8)], B. Khurelbaatar[8)] and R. Togoo[8)].

K.G. Akhobadze[9)], A.K. Djavrishvili[9)], T. Grigalashvili[9)], E.S. Ioramashvili[9)], A.V. Kharadze[9)], L. Khizanishvili[9)], T.V. Khuskivadze[9)], L.V. Shalamberidze[9)] and N. Shubitidze[9)].

V. Djordjadze[10)], N. Grigalashvili[10)], Z. Menteshashvili[10)], M. Nioradze[10)], M. Tabidze[10)] and Y. Tevzadze[10)].

D. Felea[11)], A. Gheata[11)], M. Gheata[11)], M. Haiduc[11)], D. Hasegan[11)], R. Marginean[11)], R.I. Nanciu[11)] and S.I. Zgura[11)].

Jyvaskyla, Finland, Department of Physics, University of Jyvaskyla and University of Helsinki:
J. Aysto, V. Ruuskanen and W. Trzaska.

Kharkov, Ukraine, National Scientific Centre 'Kharkov Institute of Physics and Technology':
G.L. Bochek, V.F. Boldyshev, I.F. Chervonny, A.N. Dovbnya, V.I. Kulibaba, N.I. Maslov, S.M. Potin, I.M. Prokhorets and A.F. Starodubtsev.

Kharkov, Ukraine, Scientific and Technological Research Institute of Instrument Engineering:
V.N. Borshchov, S.K. Kiprich, O.M. Listratenko, G. Protsay, V.E. Starkov and M. Zamirets.

Kiev, Ukraine, Department of High Energy Density Physics, Bogolyubov Institute for Theoretical Physics, National Academy of Sciences of Ukraine:
T. Hryn'ova, D.E. Kharzeev, V. Palshin, O. Pavlenko, A. Velytsky and G. Zinovjev.

Košice, Slovakia, Institute of Experimental Physics, Slovak Academy of Sciences and Faculty of Science P.J. Šafárik University:
J. Fedoršin, M. Hnatič, A. Jusko, B. Kocper, I. Králik, A. Kravčáková, F. Kriváň, I. Kuľková, M. Lupták, G. Martinská, B. Pastirčák, L. Šándor, J. Urbán, S. Vokál and J. Vrláková.

Legnaro, Italy, Laboratori Nazionali di Legnaro:
R.A. Ricci.

Lisbon, Portugal, Departamento de Física, Instituto Superior Técnico:
J. Barbosa, P. Branco, R. Carvalho, J. Seixas and R. Vilela Mendes.

Lund, Sweden, Division of Cosmic and Subatomic Physics, University of Lund:
L. Carlen, S.I.A. Garpman, H.-A. Gustafsson, P. Nilsson, A. Oskarsson, L. Osterman, I. Otterlund, D. Silvermyr and E.A. Stenlund.

Lyon, France, Institut de Physique Nucléaire de Lyon (IPNL), IN2P3-CNRS et Université Claude Bernard Lyon-I:
M.Y. Chartoire, M. Chevallier, B. Cheynis, D. Essertaize, E. Galichet, E. Gangler, M. Goyot, J.Y. Grossiord, R. Guernane, A. Guichard, D. Guinet, G. Jacquet, P. Lautesse, M. Miguet and S. Tissot.

Marburg, Germany, Fachbereich Physik, Philipps Universität:
F. Eckhardt, V. Friese and F. Pühlhofer.

Mexico City, Mexico, Centro de Investigación y de Estudios Avanzados:
R. Hernández Montoya, G. Herrera Corral, L. Magana, H. Mendez and L.M. Montaño.

Minsk, Belarus, Institute for Nuclear Problems, State University:
A.A. Lobko.

Moscow, Russia, Institute for Nuclear Research, Academy of Science:
K.A. Chileev, S.N. Filippov, M.B. Goloubeva, F.F. Gouber, T.L. Karavitcheva, A.B. Kourepin, A.I. Maevskaia, V.I. Razine, A.I. Rechetine and N.S. Topilskaia.

Moscow, Russia, Institute for Theoretical and Experimental Physics:
A.N. Akindinov, S.V. Boiarinov, V. Golovine, I.G. Grichouk, A.B. Kaidalov, M.M. Kats, I.T. Kiselev, S.M. Kisselev, E. Lioublev, M. Martemianov, A.N. Martemiyanov, P.A. Polozov, S.A. Pozdniakov, V.S. Serov, A.V. Smirnitski, M.M. Tchoumakov, I.A. Vetlitski, K.G. Volochine, L.S. Vorobiev and B.V. Zagreev.

Moscow, Russia, Russian Research Center 'Kurchatov Institute':
V. Antonenko, S. Beliaev, R. Cherbatchev, I. Doubovik, S. Fokine, M. Ippolitov, K. Karadjev, A.L. Lebedev, V. Lebedev, V.I. Manko, G. Mguebrichvili, T. Moukhanova, A. Nianine, S. Nikolaev, S. Nikouline, O. Patarakine, D. Peressounko, I. Sibiriak, A. Vasiliev, A. Vinogradov and M. Volkov.

Moscow, Russia, Moscow Engineering Physics Institute:
V. Grigoriev, V. Kapline, V. Loguinov and M. Strikhanov.

Münster, Germany, Institut für Kernphysik, Westfälische Wilhelms Universität:
D. Bucher, T. Peitzmann, K. Reygers, R. Santo, H. Schlagheck and M. Wahn.

Nantes, France, Laboratoire de Physique Subatomique et des Technologies Associées:
L. Aphecetche, T. Bernier, A. Boucham, S. Bouvier, L. Conin, J.P. Cussonneau, H. Delagrange, D. D'Enterria, B. Erazmus, S. Giliberto, B. Guillet, H.H. Gutbrod, M.S. Labalme, P. Lautridou, F. Lefèvre, M. Le Guay, L. Luquin, L. Martin, G. Martinez, V. Métivier, M.J. Mora, P. Pichot, A. Rahmani, O. Ravel, T. Reposeur, F. Retiere, P. Rivoalan, C.S. Roy, D. Roy, Y. Schutz and A. Tournaire.

NIKHEF, The Netherlands, National Institute for Nuclear and High Energy Physics:
M. Botje[12)], A. Buijs[13)], J.J.F. Buskop[12)], A.P. De Haas[13)], P.K.A. De Witt Huberts[12,13)], R. Kamermans[12,13)], P.G. Kuijer[12,13)], G. Nooren[12)], C.J. Oskamp[13)], A. Van Den Brink[13)], N. Van Eijndhoven[13)] and J. Visschers[12)].

Novosibirsk, Russia, Budker Institute for Nuclear Physics:
A.R. Frolov, I.N. Pestov and M.A. Tiounov.

Oak Ridge, U.S.A., Instrumentation and Controls Division, Oak Ridge National Laboratory:
C.L. Britton, W.L. Bryan, J.W. Walker and A.L. Wintenberg.

Orsay, France, Institut de Physique Nucléaire, Université de Paris-Sud:
L. Bimbot, P.F. Courtat, R. Douet, B. Genolini, H. Harroch, D. Jouan, L. Kharmandarian, Y. Le Bornec, M. Mac Cormick, J. Peyré, J. Pouthas, R. Sellem and N. Willis.

Oslo, Norway, Department of Physics, University of Oslo:
A.K. Holme, L.M. Ingebrigtsen, G. Løvhøiden, B. Skaali, T.S. Tveter and D. Wormald.

Padua, Italy, Dipartimento di Fisica dell'Università and Sezione INFN:
F. Antinori, F. Brandolini, N. Carrer, M. Morando, A. Pepato, F. Scarlassara, G. Segato, F. Soramel and E. Zanoni.

Prague, Czech Republic, Institute of Physics, Academy of Science:
J. Mareš, E. Mihoková, M. Nikl, K. Píška, K. Polák and P. Závada.

Protvino, Russia, Institute for High Energy Physics:
A.M. Blik, M. Bogolyubsky, G. Britvitch, S. Erine, G.V. Khaoustov, I.V. Kharlov, V.N. Kolossov, V. Lichine, S.A. Sadovski, V.D. Samoilenko, P.A. Semenov, V.I. Suzdalev, V. Tikhonov and A. Zviagine.

Řež u Prahy, Czech Republic, Academy of Sciences of Czech Republic, Nuclear Physics Institute:
V. Hanzal, J. Hošek, I. Hřivnáčová, V. Kuschpil, A. Kugler, V. Petráček, M. Šumbera, A. Tlustý, V. Wagner and D. Zákoucký.

Rome, Italy, Dipartimento di Fisica dell'Università 'La Sapienza' and Sezione INFN:
S. Di Liberto, M.A. Mazzoni, F. Meddi, D. Prosperi and G. Rosa.

Saclay, France, Centre d'Etudes Nucléaires, DAPNIA/SPhN:
A. Baldisseri, H. Borel, I. Chevrot, J. Gosset, F.M. Staley and Y. Terrien.

Salerno, Italy, Dipartimento di Fisica Teorica e S.M.S.A., Università di Salerno and Sezione INFN:
G. Grella, M. Guida, G. Romano and T. Virgili.

Sarov, Russia, Russian Federal Nuclear Center (VNIIEF):
S. Abramovitch, V. Basmanov, V. Ianowski, R. Ilkaev, L. Ilkaeva, A. Ivanov, A. Khlebnikov, E. Kolokolnikov, V. Matiev, S. Nazarenko, V. Pounine, S. Poutevskoi, I. Selin, M. Tarasov, I. Vinogradov, S. Zhelezov and A. Zhitnik.

St. Petersburg, Russia, Institute for Physics of St. Petersburg State University, Mendeleev Institute for Metrology and Meson Scientific Association:
L.Y. Abramova, V.S. Alexandrov, V.M. Baratov, A.A. Bolonine, M.A. Braun, V.M. Dobulevitch, G.A. Feofilov, O.N. Godissov, S. Guerassimov, S.N. Igolkine, M.I. Ioudkine, A.A. Kolojvari, V. Kondratiev, I.A. Novikov, S.V. Potapov, O.I. Stolyarov, T.A. Toulina, F.A. Tsimbal, F.F. Valiev, V.V. Vetchernine, L.I. Vinogradov and L.F. Vitouchkine.

Strasbourg, France, Institut de Recherches Subatomiques:
L. Arnold, M. Ayachi, J. Baudot, J.D. Berst, J.P. Blondé, D. Bonnet, J.P. Coffin, W. Dulinski, M. Germain, G. Guillaume, L. Hebrard, Y. Hu, F. Jundt, C. Kuhn, J. Lutz, A. Michalon, F. Rami, C. Suire and A. Tarchini.

Trieste, Italy, Dipartimento di Fisica dell'Università and Sezione INFN:
V. Bonvicini, A. Gregorio, A. Rachevski, A. Vacchi, L. Valentincic and N. Zampa.

Turin, Italy, Dipartimenti di Fisica dell'Università and INFN:
B. Alessandro, R. Arnaldi, S. Beolé, G. Bonazzola, E. Botta, L. Busso, P.G. Cerello, E. Chiavassa, P. Cortese, F. Daudo, N. De Marco, A. Feliciello, M. Gallio, G. Giraudo, P. Giubellino, A. Marzari-Chiesa, M. Masera, G. Mazza, P. Mereu, B. Minetti, O. Morra, A. Musso, D. Nouais, A. Piccotti, G. Piragino, L. Riccati, E. Scomparin, F. Tosello, E. Vercellin and A. Werbrook.

Warsaw, Poland, Soltan Institute for Nuclear Studies:
D. Czerwinski, A. Deloff, K. Karpio, S. Kozak, L. Lukaszek, H. Malinowski, T. Siemiarczuk, G. Stefanek, L. Tykarski and G. Wilk.

Warsaw, Poland, University of Technology, Institute of Physics:
J. Buryk, J. Grabski, P. Kindziuk, A. Kisiel, P. Leszczynski, A.M. Maliszewski, J.M. Mazur, T.J. Pawlak, W.S. Peryt, J. Pluta, M. Przewlocki, S. Radomski, A.M. Roszczewski, M. Sarzynski, P. Skowronski, P. Stepien and P. Szarwas.

Wuhan, China, Institute of Particle Physics, Huazhong Normal University:
X. Cai, Y. Hu, F. Liu, L. Liu, H. Wang and D. Zhou.

Yerevan, Armenia, Yerevan Physics Institute:
R. Asatryan, M. Atayan, R. Avakian, V. Danielyan, V. Gavalian, A. Grigorian, S. Grigoryan, H. Gulkanyan, R. Hakobyan, V. Kakoyan, S. Mehrabyan, L. Parlakyan, R. Shahoyan and H. Vardanyan.

Zagreb, Croatia, Ruder Bošković Institute:
D. Ferenc, A. Ljubičić and T. Tustonic.

Spokesperson: J. Schukraft, e-mail Jurgen.Schukraft@cern.ch
Deputy: H. Gutbrod, e-mail GUTBROD@VXWA80.CERN.CH

[1] Also at CERN, Geneva, Switzerland
[2] On leave from Seasoft, Catania, Italy.
[3] On leave from JINR, Dubna, Russia.
[4] On leave from IHEP, Protvino, Russia.
[5] On leave from Budapest University, Hungary.
[6] Institute of Physics, Pedagogical University, Kielce, Poland.
[7] Research Centre for Applied Nuclear Physics (RCANP), Dubna, Russia.
[8] Institute of Physics and Technology, Mongolian Academy of Sciences, Ulaanbaatar, Mongolia.
[9] Institute of Physics, Georgian Academy of Sciences, Tbilisi, Georgia.
[10] High Energy Physics Institute, Tbilisi State University, Tbilisi, Georgia.
[11] Institute of Space Sciences, Bucharest, Romania.
[12] Foundation of Fundamental Research of Matter in The Netherlands.
[13] Utrecht University, Utrecht, The Netherlands.

Contents

1 Introduction

This document is an addendum to the ALICE Proposal [1] with the aim to propose an extension of the present central detector to allow a comprehensive investigation of electron pair physics as well as studies of open charm and open beauty production in nucleus-nucleus collisions at LHC energy. The ALICE detector and its physics capabilities are described in detail in the proposal and the addendum for the forward muon spectrometer [2]. The addition of a Transition Radiation Detector (TRD) to the central ALICE barrel will provide, in conjunction with data from the Time Projection Chamber (TPC) and Inner Tracking System (ITS) detectors, sufficient electron identification to measure, in the di-electron channel, the production of light and heavy vector meson resonances for Pb+Pb collisions at the LHC as well as to study the dilepton continuum. In addition, the excellent electron identification at relatively large transverse momenta ($p_{\mathrm{t}} > 1$ GeV/c) can be used in conjunction with the impact parameter determination of electron tracks in the ITS to determine the overall amount of open charm and open beauty produced in the collision. With a similar technique one can also separate directly produced J/Ψ mesons from those resulting from B decay. The latter could potentially mask the expected J/Ψ suppression due to quark-gluon plasma formation and their measurement is, therefore, of crucial importance. Furthermore, since the TRD is a fast tracker, it can be used as an effective trigger for high transverse momentum electrons. This can be used to considerably enhance yields for Υ detection, for the measurement of the high mass part of the dilepton continuum, and for J/Ψ detection at high transverse momentum.

2 Physics motivation

The physics case for the measurement of dilepton pairs has already been made in some detail in the ALICE Proposal and the muon arm addendum. Here we focus on what is specific for di-electrons in the central region and on recent developments in this area. As will become clear, the di-electron physics we propose here is unique and complementary to the physics capabilities which were opened up by the addition of the forward muon detector to ALICE.

To start the discussion we present, in Fig. 1, a schematic view of the expected di-electron mass spectrum in the mass range $0 < m_{e^+e^-} < 5$ GeV/c^2 for Pb+Pb collisions at LHC energy, i.e. with 8000 charged particles per unit of rapidity, and under the assumption of perfect particle identification. This spectrum is dominated by combinatorial background from electrons resulting from the (Dalitz) decays of light mesons (π^0, η) and the semileptonic decays of the copiously produced D and B mesons. The Drell-Yan continuum and any possible thermal continuum are not visible on this scale but all vector meson resonances (except the very broad ρ meson) are still measurable, although the light ones (ω and ϕ) only with a signal/background ratio of the order of 5%. The spectrum is calculated assuming perfect electron identification. Therefore, any pions misidentified as electrons will deteriorate the situation.

The spectrum clearly identifies the main challenges of di-electron measurements at LHC: the detector has to provide excellent electron identification, has to be constructed such that one can deal with or reduce the large combinatorial background from Dalitz and semileptonic D and B decays, and has to have sufficient resolution and granularity to identify narrow

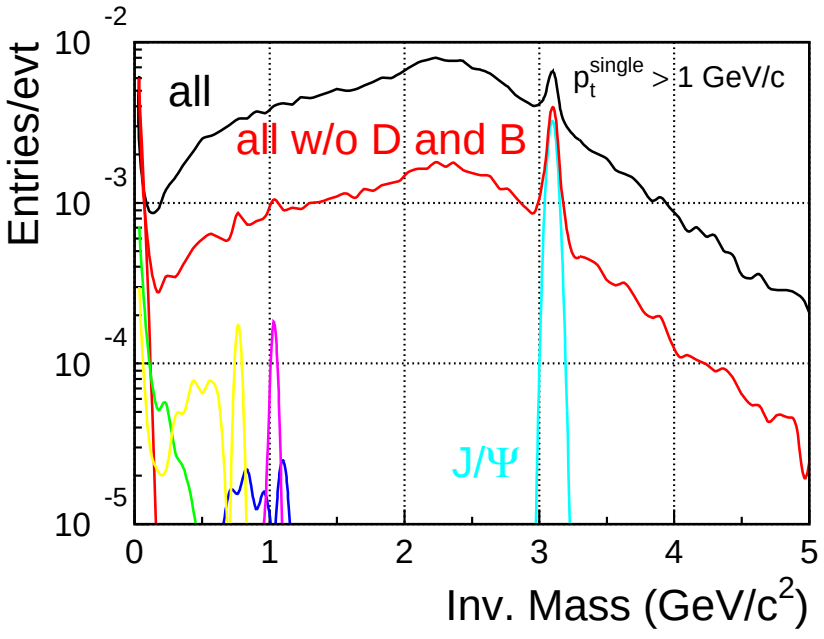

Figure 1: Invariant mass distribution of e^+e^- pairs produced in central Pb+Pb collisions at the LHC (simulation). Included are electron pairs from resonance decays (π^0, η, ρ, ω, ϕ, J/Ψ) and from Drell-Yan, as well as electrons from D and B meson decays. The corresponding combinatorial background including (excluding) the electrons from D and B meson decays is shown as the solid black (red) line.

resonances with small signal/background ratio in a very high multiplicity environment.

The physics rewards for such a challenging detector project are, however, large:

- Spectroscopy of heavy and light vector meson resonances in an environment which is most likely baryon free.
- Measurement of the open charm and open beauty cross sections through their electron decay channels.
- Identification of J/Ψ mesons resulting from B decay, a potentially serious background for measurement of "direct" J/Ψ's.
- Access to the dilepton continuum at the Drell-Yan level.
- Characterization of the event class of the di-electron events in the ALICE central detector, i.e. within the same acceptance as for the dileptons.

In the following we briefly discuss these issues. We first note that, in ALICE, the dilepton measurement in the muon channel will focus on rapidities $2.5 < y < 4$. While this has the clear advantage that the muon energies are sufficiently high for the absorber technique to be applicable, with experimental consequences for backgrounds and rates which are in detail spelled out in the muon proposal, one should realize that baryon rapidity shifts of the order of 3 or more units of rapidity are already observed in the SPS fixed target program [3]. Along the same line, recent investigations [4] indicate that, at y=4, there might be a substantial net baryon density even at LHC energies. Clearly, the region which is expected to be most baryon free is near y=0, where the proposed measurements will be performed.

The measurement of the cross sections for open charm and open beauty production is of paramount importance for understanding the role of color screening in the expected suppression of quarkonium production in Pb+Pb collisions at LHC energy. First, one should note that quarkonium production and open charm or open beauty production are intimately related [5]. The heavy quarks are dominantly produced in hard partonic scattering processes (gluon fusion). Some of these heavy quarks will eventually form quarkonia, while the large majority will end up in correlated pairs of D and B mesons. Typical numbers are about 50 $c\bar{c}$ pairs per unit of rapidity compared to 0.5 for J/Ψ mesons in central Pb+Pb collisions (see Table 4). These numbers have been obtained using a perturbative QCD approach based on the PYTHIA framework with a K-factor adjusted to reproduce B meson production in $p\bar{p}$ collisions at the Tevatron and D meson production at lower energies. Similar results have been obtained by Gavin et al. [6]. The extrapolation to nucleus-nucleus collisions is done as in [7], i.e. by the total number of nucleon-nucleon collisions. This number is calculated from the nuclear collision geometry at a given impact parameter assuming a Woods-Saxon nuclear density distributions. In the calculation the inelastic nucleon-nucleon cross section drops out and one obtains the scaling factor between the cross section in pp and the multiplicity in Pb+Pb.

One should note that these predictions are still rather uncertain. First, there are indications from the measurements of NA50 at CERN of a possible enhanced open charm production (relative to PYTHIA predictions) already in Pb+Pb collisions at SPS energy [8]. Secondly, the produced heavy quarks may suffer significant energy losses in the hot and dense fireball formed at LHC energies, leading to considerable kinematical rearrangement of the final rapidity and p_t distributions and, consequently, also to potentially drastic changes in the dilepton invariant mass spectrum from semileptonic decays [9, 10]. Thirdly, we have not accounted in our simulations for a possible nuclear shadowing of the parton distribution functions which

might lead to a factor of two reduction in cross section at LHC energies. Clearly, a direct measurement of charm and beauty would be of great value for the interpretation of the data.

Furthermore, since the quark and the gluon structure functions are likely to be different at LHC energies, one cannot use the Drell-Yan continuum as a convenient normalization for the J/Ψ measurements. In addition, the Drell-Yan cross section is expected to be completely masked by the open charm continuum (for a discussion of our sensitivity to continuum particles, see below). However, a direct measurement of the open charm yield simultaneously with the yield of quarkonia will provide a natural normalization and a gauge against which to quantify the expected suppression of quarkonia.

As already mentioned above, the decay of B mesons can produce significant numbers of J/Ψ mesons, especially at large p_t. This is demonstrated in Fig. 2, where the transverse momentum distribution for "directly produced" J/Ψ mesons is compared to the expected distribution of J/Ψ's from B decay. The calculations were performed assuming no suppression for the primary J/Ψ mesons. If one wants to be sensitive to suppression factors of 10 or more and if one wants to address the p_t dependence of the suppression, it is obvious that the B decay channel needs to be measured. The capability to do this is an important aspect of the present proposal.

Another issue is the secondary production of J/Ψ mesons from the annihilation of D mesons, i.e. the process $D+\bar{D} \rightarrow J/\Psi + \pi$. Estimates for the yield due to this process have recently been given [11, 12]. For presently discussed values of the cross section for $D+\bar{D} \rightarrow J/\Psi + \pi$ secondary production could seriously obscure the expected suppression in the plasma. It is, therefore, clear that a clean interpretation of J/Ψ production data can only be obtained through a comprehensive measurement of open charm production.

The thermal dilepton continuum is notoriously difficult to measure. On the other hand, access to the thermal radiation emitted from the hot, partonic fireball presumably formed at early times in a Pb+Pb collision at LHC energy would give access to the initial temperature and, in conjunction with a measurement of the associated (final) charged particle multiplicity, to the entropy and, thereby, to the number of degrees of freedom in the plasma. Furthermore,

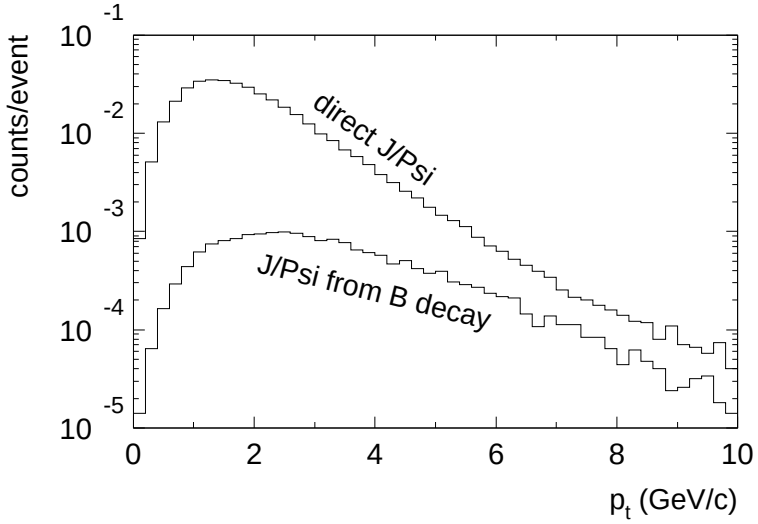

Figure 2: Transverse momentum distributions of J/Ψ's produced directly and via B decay.

the initial entropy density is so large that a fairly long lived mixed phase is expected to be formed, which also should produce a sizeable thermal continuum with a slope parameter of the transverse mass spectrum given by the critical temperature. An example of the expected temporal evolution of the partonic fireballs produced in Pb+Pb collisions at LHC energy is shown in Fig. 3. This figure illustrates that, even assuming relatively large transverse flow velocities already in the plasma, the mixed phase is expected to be a dominant feature of the evolution. Under those circumstances it is clear that all efforts should be made to try to address the continuum radiation experimentally. Predictions for the yield of thermal radiation depend sensitively on the initial temperature, the degree of chemical equilibration of gluons and quarks in the hot fireball, and on the lifetime of the mixed phase. As an ambitious goal in this area we would like the ALICE experiment to be sensitive to the di-electron continuum at the level of the dilepton yield from the Drell-Yan process. This is roughly the level of current predictions for thermal radiation excluding contributions from the mixed phase. At LHC energies the continuum is dominated, as shown in Fig. 1, by combinatorial background from correlated and uncorrelated charm and beauty decays. We will demonstrate below that electrons from semileptonic D and B meson decays can be recognized and (for this purpose)

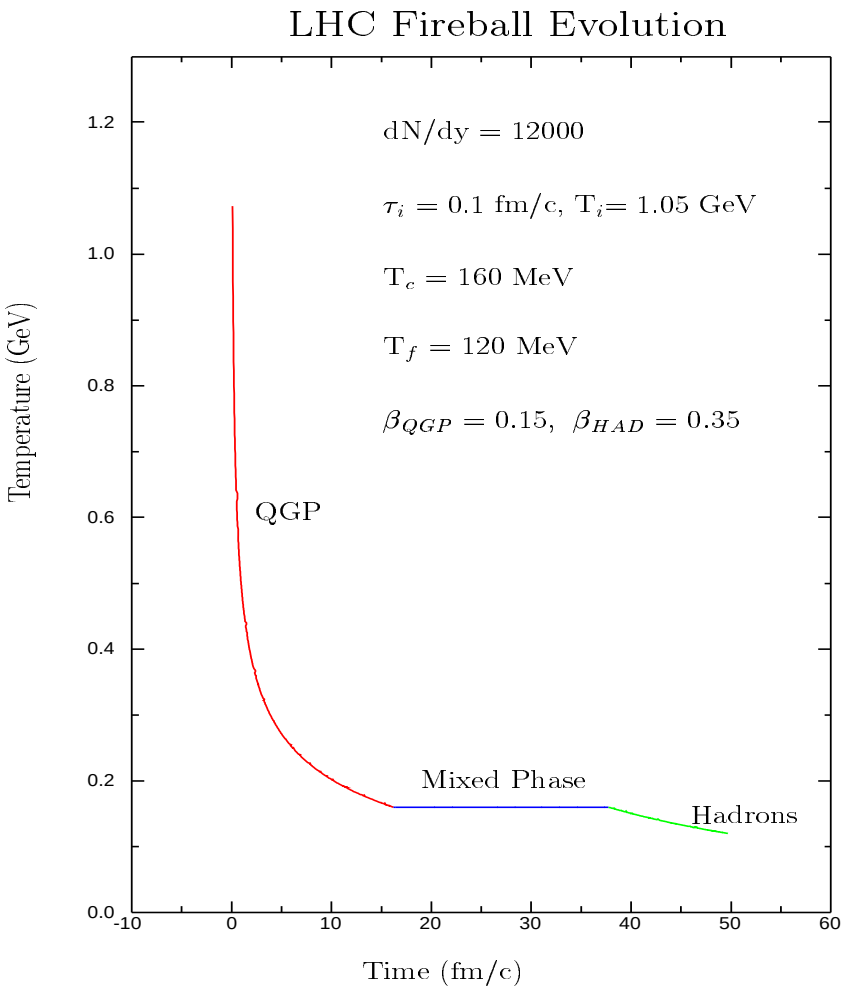

Figure 3: Expected temporal evolution of the partonic fireballs produced in Pb+Pb collisions at LHC energy (see [12]). The calculation was done assuming 12000 particles per unit rapidity, roughly corresponding to $\mathrm{d}N_{\mathrm{ch}}/\mathrm{d}y$=8000.

rejected such that the Drell-Yan continuum can be measured within ALICE, if a detector for electron identification as outlined in this addendum is added to the present set of detectors in the central region.

It is of considerable interest to be able to classify the di-electron events by their associated event shape and distribution as measured in the ALICE central detector. In that way one can, e.g., search for the dependence of J/Ψ production yields on the strangeness content of the associated events, on large hadron mean transverse momentum, or on the magnitude of elliptic flow. Such variations in global hadronic observables, especially if they happen simultaneously, are potential signals of quark-gluon plasma formation. Their connection to leptonic signals such as J/Ψ suppression is of utmost importance for the physics program planned with the ALICE detector. Note that the information from the central detector on hadron content and distributions is important for the study of short range ($\delta y < 1$) lepton-hadron correlations while the dimuon measurement at forward rapidity would be sensitive to long range correlations ($\delta y > 2$).

Another big advantage of the addition of a TRD to ALICE is the possibility to use it as an effective trigger for high transverse momentum or high mass electron pairs. Since, as described below, the TRD is devised such that tracking information is available a few microseconds after the start of an event, one can use this to select events with high momentum electron candidates and, e.g., open the gating grid of the TPC only for such events. First studies indicate that this technique addresses the luminosity limitation due to the long drift time in the TPC and could enhance the yields of high mass pairs by more than an order of magnitude.

An interesting example of the synergy between the ALICE muon arm and the proposed TRD detector is the study of electron-muon coincidences. We have performed a feasibility study for this and the results, as briefly discussed in Section 4.8, are encouraging. The main interest in such measurements is to get more information on open charm production in a channel where systematic errors are completely different from the planned measurement of displaced vertices. Furthermore, such measurements would also provide information on the rapidity dependence of open charm production, which is particularly interesting in view of the possibility of large energy losses for heavy quarks in the hot and dense LHC fireball.

The TRD detector, as outlined below, will be a barrel detector, surrounding the TPC with 6 layers of a combination of a foil stack and a Xe-filled wire chamber. The aim is to build this detector with an acceptance completely matching that of the TPC, corresponding to a pseudo-rapidity coverage of $-0.9 < \eta < 0.9$. With this full TRD scenario all physics topics discussed above can be addressed with reasonable statistics within a running period of 10^6 s corresponding to one ALICE year. To illustrate this we have evaluated (see Table 10 in Section 4.9) the expected yields for the relevant observables for a full size and half size detector. As can be seen from this table, the number of detected Υ mesons in the full size detector, e.g., is expected to be around 10^4 in minimum bias collisions and employing the electron trigger. We note, however, that the efficiency for detecting dilepton pairs with high mass and/or high transverse momentum scales approximately with the square of the detector solid angle. Reducing the TRD coverage by approximately a factor of 2 in area as is consistent with the presently accepted ALICE funding scheme and money matrix would lead to a significantly reduced physics potential for Υ and high $p_{\rm t}$ J/Ψ measurements as well as for studies of the high mass continuum. All other physics observables discussed above could be well measured also with such a reduced size detector, albeit with less statistical accuracy. More information about cost estimates and funding can be found in Section 7.

3 The Transition Radiation Detector

3.1 Introduction

For a comprehensive investigation of the physics accessible with electron pair and single electron spectroscopy in the central detector of ALICE the particle identification capabilities have to be improved. For this purpose we propose to extend the instrumentation of the central ALICE barrel by a transition radiation detector located between the TPC and the Time-Of-Flight (TOF) detector. The TRD will match the full TPC acceptance both in azimuth and in pseudorapidity ($|\eta| \leq 0.9$). With the resulting additional pion rejection factor in the order of hundred over the full acceptance of the central detector electron physics can be addressed quantitatively within ALICE as discussed in Section 4.

3.2 Design considerations

The basic operational principle of the TRD proposed here is sketched in Fig. 4. To a large extent we follow the design of the TRD developed for the PHENIX experiment at Brookhaven [13]. Transition radiation (TR) is emitted when a charged particle crosses the boundary between two media with different indices of refraction. TR becomes useful for particle detectors [14] when it can be observed in form of soft X-rays, typically in the energy range from 2 to 30 keV; this is the case for charged particles with Lorentz factors γ larger than about 1000. Therefore, TRDs are ideally suited for electron/pion separation for momenta above 0.5 GeV/c. Since the probability for soft X-ray emission is only about 1% per boundary crossing, practical TRDs use radiators with a large number of interfaces, e.g. foil stacks, fibers, or foam radiators.

Wire chambers, operated with xenon-based gas mixtures for efficient TR absorption, are commonly used to detect the produced X-rays. The typical emission angle of TR photons is $1/\gamma$. This means, the X-ray photons are practically emitted along the charged particle direction. The X-ray detector therefore usually measures the superposition of the ionization energy loss of the primary charged particle and the energy deposition of the produced X-rays. A very efficient discrimination between electrons and pions can be achieved using Time

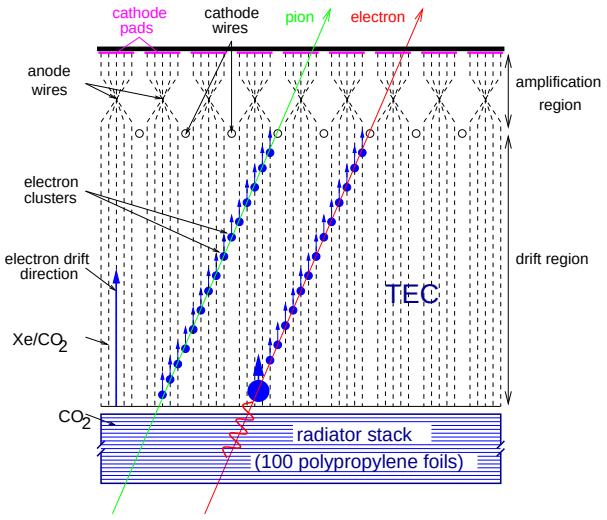

Figure 4: Basic operational principle of the proposed TRD.

Expansion Chambers (TEC) as X-ray detectors. The electron clusters produced in the gas volume of the detector drift in a homogeneous electric field towards the amplification region of the TEC. There, gas multiplication takes place at the anode wires and the corresponding signals induced on a cathode pad plane are read out. The pulse shape (in terms of electrons before the gas amplification) as a function of drift time is depicted in Fig. 5 for a collection of six typical "events", containing one electron and one pion of 3 GeV/c momentum each. It shows, for both particles, the energy loss by ionization with its fluctuations and, in case of electrons, marked by the dots, the superimposed signal due to the absorption of TR photons. These distributions have been obtained for the special case where charged particles penetrate the TEC in the drift direction. The gas gain fluctuations and the electronic noise, as well as the diffusion along the drift path, have been taken into account. No charge loss due to shaping or charge sharing was taken into account.

Since for xenon there are no measurements concerning the cluster size distribution, we were bound to use a model for the delta-ray spectrum. The photo-absorption and ionization model (PAI) [15] has been intensively used for such studies [16, 17]. For the present simulations we adopted a parameterization of ref. [16] that gives reasonable values for the average ionization energy loss. See e.g. [18] for all the details concerning drift chambers.

In xenon-rich gas mixtures the energy loss of minimum ionizing particles is of the order of a few keV/cm while the TR photons typically deposit their full energy in a very small gas volume close to the entrance window of the TEC. Note that the mean free path of typical TR X-rays with about 10 keV energy is about 10 mm in xenon. Electrons generating TR can therefore be tagged by a large signal in a short (and generally late) drift time interval, as can be seen in Fig. 5. Because the energetic delta-rays produced by the pions can mimic to a certain extent the TR signals, it is mandatory to measure the size and position of individual clusters. Obviously, this kind of cluster analysis with a TEC represents a more sophisticated approach to separate electrons from pions compared to the traditional charge or cluster

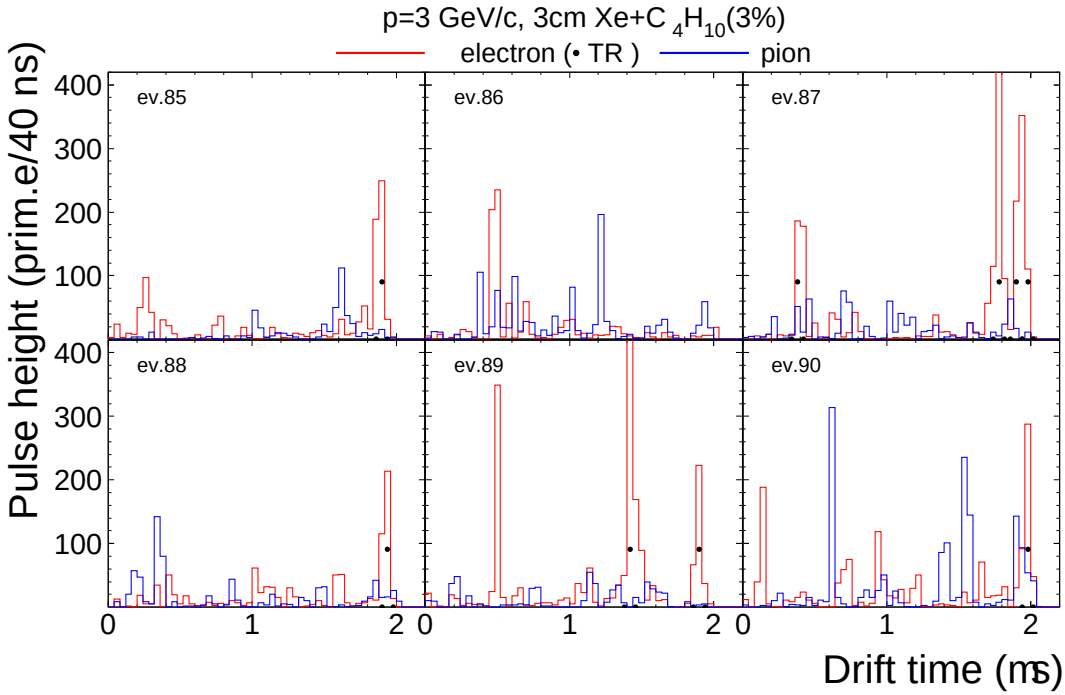

Figure 5: A sample of signals produced by electrons and pions passing one TRD layer.

counting analysis techniques. Especially in the high particle multiplicity environment at LHC we expect the cluster analysis to be more efficient than the latter methods. Furthermore, it would allow for a certain suppression of highly ionizing particles using only the information provided by the TRD itself. This may turn out to be crucial in the ALICE environment, where a significant fraction of the particles will be non-minimum ionizing.

As illustrated in Fig. 6 the performance of any TRD is strongly correlated with its overall depth. For a large variety of existing or proposed TRDs the pion misidentification probability at a fixed electron identification efficiency of 90% is shown as a function of the detector depth. From these data it is evident that a device meeting our requirements should have a minimum depth of about 60 cm.

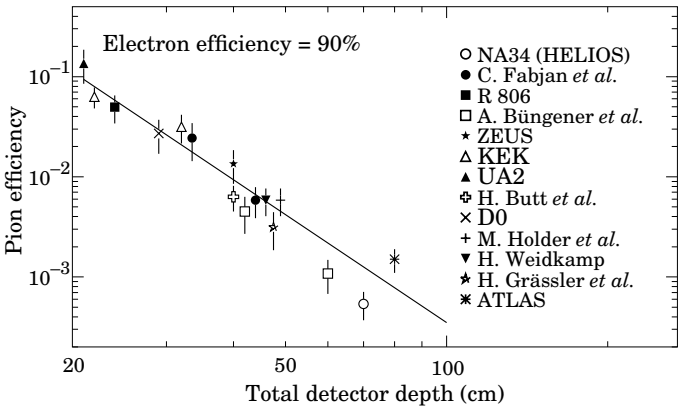

Figure 6: Pion misidentification probability as a function of the total detector depth for several existing and proposed transition radiation detectors (taken from [19]).

The performances summarized in Fig. 6 were obtained for isolated particles, while in "real life" experiments the rejection factors can be worse by as much as a factor of 10 [14]. To ensure the needed factor of about 100 for pion rejection we aim, at the simulation level, at a rejection factor close to 1000.

It is not only the depth of the detector that determines its performance, the number of layers and the method to process the signals play a significant role as well. To illustrate the last point, Fig. 7 shows as a function of the electron efficiency the pion misidentification probability derived using four methods: 1) Q - likelihood on total charge, integrated above a certain low value threshold (10 times the noise level) [20]; 2) N - likelihood on cluster number distribution. The clusters are counted if they are above a high value threshold [21]; 3) QN - likelihood on total charge in the clusters [22]; 4) QX - two dimensional likelihood taking into account the cluster charge above the threshold and cluster position in the drift time [23].

In general, a variable threshold is used. It increases as function of the distance from the radiator at which the cluster is found ("intelligent threshold" [21]), being a factor of 10 bigger at the anode wires, compared to the value at the entrance of TEC. The four panels are obtained for different values of the threshold level, $vt1$ to $vt4$ corresponding to 18, 27, 45 and 59 electrons at the entrance of TEC (long drift times, see Fig. 5). Depending on the method used, there is an optimum of the threshold value. It is also evident that the QX method gives the best result, so that from here on we use this method (for the value $vt2$ of the threshold) to derive the optimum parameters of our detector.

Since, in the momentum range of interest, only 1–2 TR photons per incident electron are produced on average in a typical radiator, a large pion rejection at 90 % electron efficiency

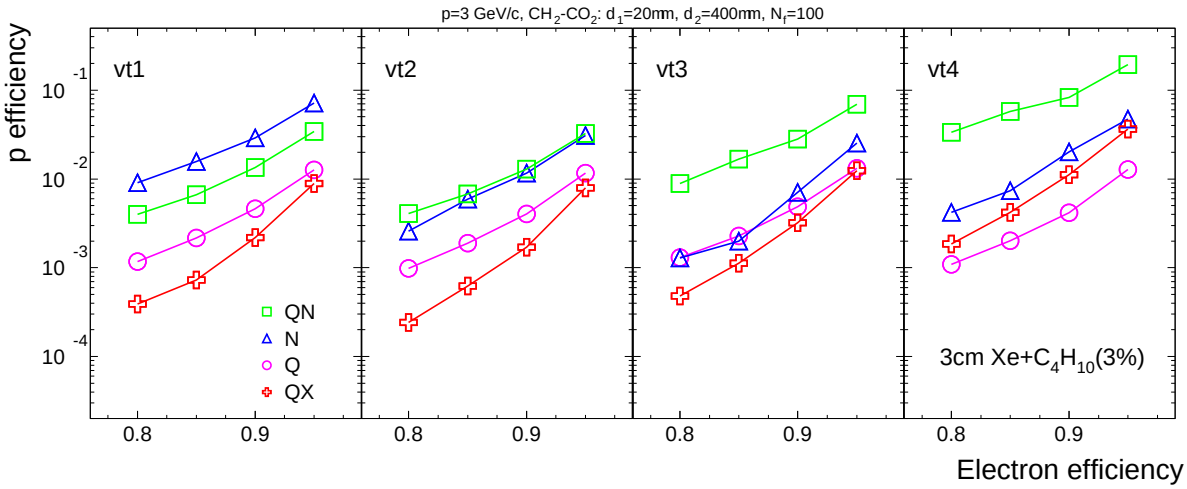

Figure 7: Pion misidentification probability as a function of electron efficiency for different methods of signal processing and four values of the threshold (see text for explanations).

cannot be obtained with a single radiator/TEC combination. The proposed TRD will therefore comprise six detector planes, each consisting of a radiator of polypropylene foils to produce transition radiation photons and a TEC operated with a xenon-based gas mixture to detect them as illustrated in Fig. 4. The material budget of the TRD has to be kept as small as possible to minimize: a) the loss of incident electrons by bremsstrahlung, b) multiple scattering of traversing charged particles, and c) the production of secondary particles, which generate background in the TRD itself and in other ALICE detectors.

In order to cope with the huge particle multiplicities, which are expected to be as high as 8000 charged hadrons per unit of rapidity for Pb+Pb collisions at maximum LHC energy, a high granularity of the TRD is mandatory. Since the number of electronics channels, dominating the overall cost of the TRD, is given by the granularity, a careful optimization of this parameter is of prime importance. A reasonable granularity can only be achieved by instrumenting the TEC with segmented cathode pad planes. A chevron-type pad shape is foreseen to achieve a good position resolution in ϕ-direction[1] with reasonable pad sizes. A good position resolution is required for an efficient and unambiguous matching of tracks reconstructed in the TPC with hits registered in the six TRD planes. Moreover, the ALICE TPC is too slow to exploit the full LHC luminosity in p+p or light ion collisions where the charged particle multiplicity will be much lower than in the case of Pb+Pb collisions. For these experiments one might consider to use the TRD, which has a drift time of only about 2 μs, as a tracking device together with the ITS. The question whether this scenario is a realistic option needs to be evaluated carefully. Clearly, a good position resolution would then be essential for a good momentum resolution. Finally, good momentum resolution by the TRD itself is also important when using the device as a trigger (see below).

In summary, the TRD design has to be optimized with respect to the following criteria:

- large pion rejection at high electron efficiency;
- full coverage of the TPC acceptance;
- minimum overall thickness in terms of radiation lengths;

[1] We use a cylindrical coordinate system with the z-direction along the beam axis.

- high granularity;
- good position resolution;
- minimal cost.

3.3 Mechanical structure

The currently envisaged mechanical design for the TRD foresees a subdivision of the detector into 540 subdetectors (18 subdivisions in the azimuth, 5 along z for a total of 6 layers). This matches the current planning for the space frame as depicted in Figs. 8, 9, and 10. In radial direction the TRD will be located between the TPC and the TOF detectors. We note that matching the geometry of all ALICE central detectors is still on-going and small changes in the geometrical arrangement could be possible in the course of this optimization procedure.

The TRD has an overall length of 734 cm in beam (z) direction. In transverse direction the inner and outer radii are 294 cm and 368 cm, respectively. In azimuth the TRD sectors are covering 20° each. In radial direction a sector consists of six detector planes as depicted in Figs. 9 and 11. The individual TRD modules consist of a combination of a foil stack as radiator and a TEC (Time Expansion Chamber) as readout chamber. To cover the full TPC acceptance ($|\eta| \leq 0.9$, corresponding to $45° \leq \Theta \leq 135°$) the width of the TRD modules in rϕ and their length in z-direction have to increase accordingly if one goes from the innermost

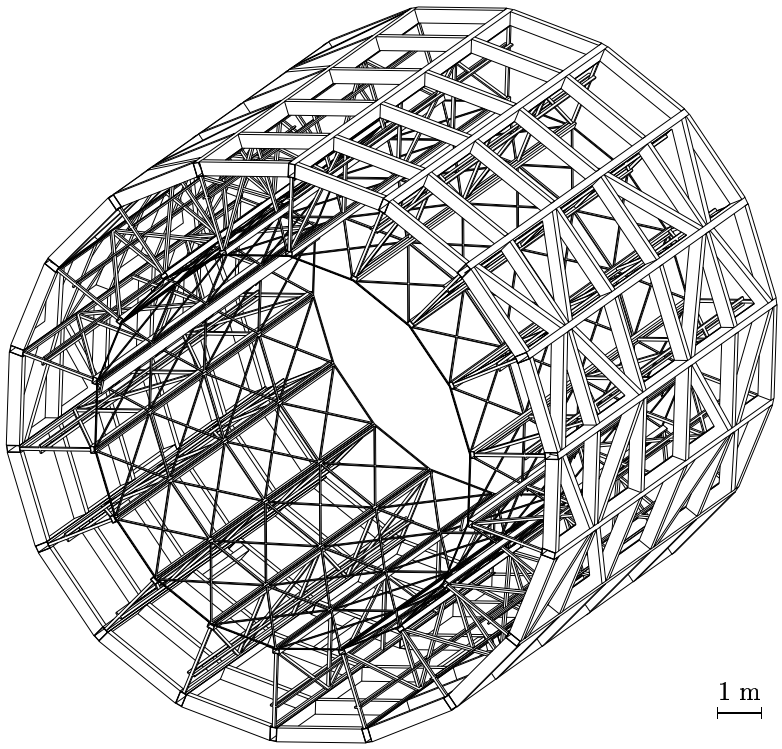

Figure 8: Sketch of the space frame for ALICE. The inner opening accommodates the TPC.

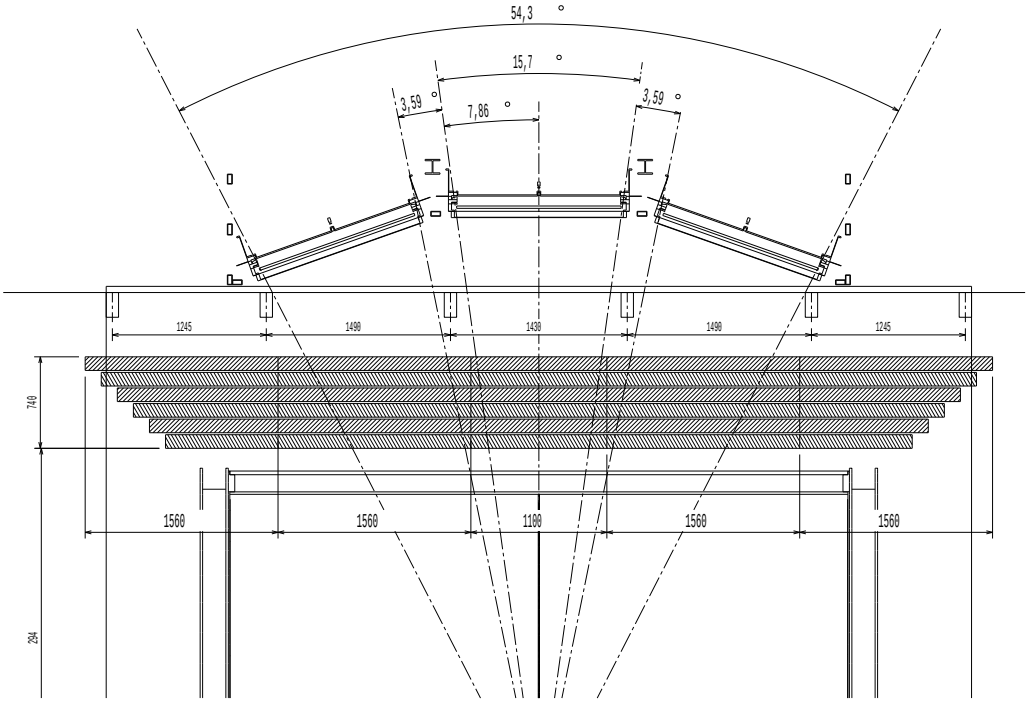

Figure 9: View of the 6 layers of the TRD in z-direction. The module boundaries of the TRD are chosen to match boundaries in the HMPID.

plane (plane 1) to the outermost plane (plane 6). The central modules (in z-direction) and the middle ones have the same length L_{i} and L_{n}, respectively, for all layers, while the length L_{o} of the two peripheral modules changes. The corresponding values are summarized in Table 1 along with the respective areas covered. Except for their width and length the TRD modules in all planes have the same mechanical structure.

The overall depth of each TRD module is 110 mm, where the radiator contributes 48 mm and the TEC together with the support structure of its cathode pad plane and the electronics fills the remaining 62 mm. Two TRD modules are separated from each other by a roughly 13 mm wide gap.

The radiator consists of 100 polypropylene foils of 20 μm thickness each with a gap of 400 μm

plane	depth [mm]	R_{in} [mm]	W [mm]	L_{i} [mm]	L_{n} [mm]	L_{o} [mm]	total area [m^2]
1	123.3	2940	996	1100	1560	910	108.3
2	123.3	3063	1041	1100	1560	1040	118.1
3	123.3	3187	1085	1100	1560	1170	128.1
4	123.3	3310	1129	1100	1560	1300	138.6
5	123.3	3433	1174	1100	1560	1430	149.6
6	123.3	3557	1218	1100	1560	1560	160.9
$\sum$	740						803.6

Table 1: Dimensions and positions R_{in} in radial direction of the individual TRD modules. The indices i, n, and o denote the inner, the two neighboring, and the outer modules of each plane, respectively. In addition, the total area covered by the TRD is given in the last row.

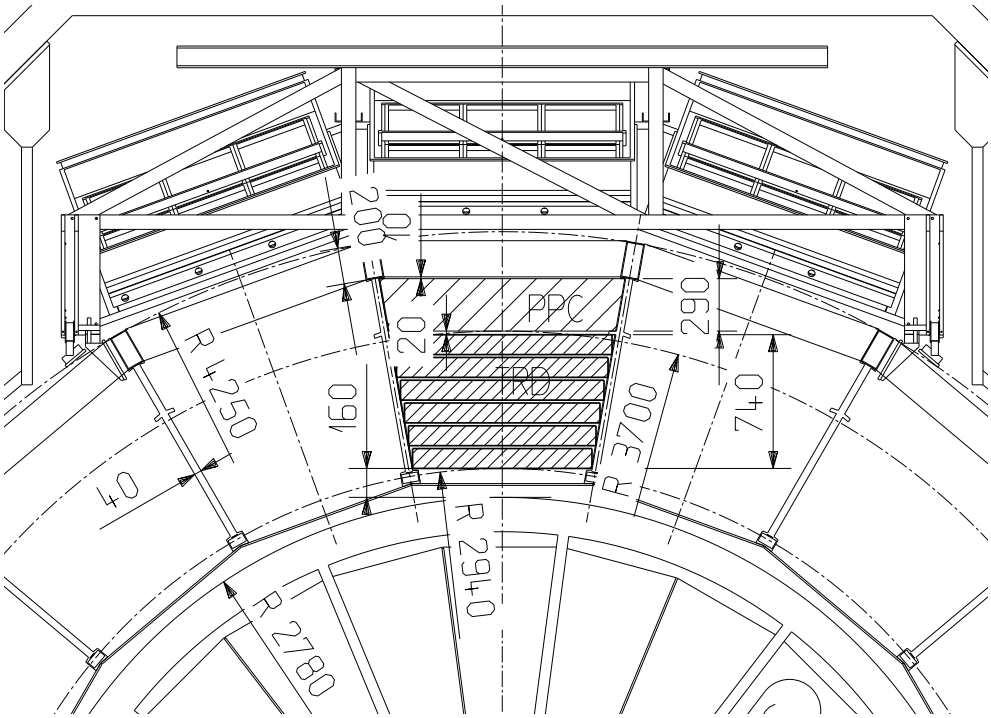

Figure 10: View of the 6 layers of the TRD in ϕ-direction. The TRD is shown together with the outer perimeter of the TPC, the PPC, and the HMPID.

between two adjacent foils. The distance between adjacent foils is kept constant through a heat imprinted structure in the foils themselves. In this way the foils need little additional stretching. To prevent sagging and to provide a gas seal of the CO_2 filled radiator volume towards the environment, it is sealed with a 5 mm plate of HEXCEL with 2 times 100 μm G10 backing. During assembly the stack is inserted from the bottom (as shown in the cross sectional cut through the readout chamber in Fig. 12). A Mylar foil of 25 μm thickness acts

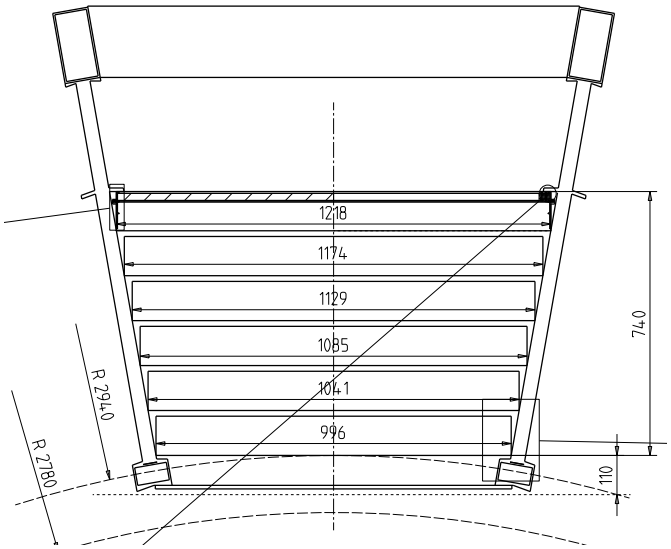

Figure 11: Cut through a stack of 6 layers of TRD detectors with some of the absolute dimensions.

as a gas barrier at the entrance window of the radiator towards the TEC. This is immediately followed by a perforated aluminum-coated Mylar foil. The perforation prevents bowing of the HV electrode and thereby prevents distortions of the electric field. In case of ideal equilibration of the pressure inside the TEC and inside the foil stack losses due to absorption in the inactive volume of the TEC will be minimal. The drift and amplification regions of the TEC have a depth of 35 mm (up to the pad plane) and are filled with the counting gas. Currently, a mixture of 97% Xe and 3% C_4H_{10} or, alternatively, 90% Xe and 10% CO_2 are foreseen (see below). The TEC comprises two wire planes inside the gas volume parallel to the entrance window and the cathode pad plane. They do not contribute significantly to the material budget and are described in detail below. The cathode pad plane consists of 10 μm thick gold-coated copper pads on a G10 layer of 100 μm thickness which, at the same time, serves as the gas barrier. To achieve the necessary rigidity of the pad plane ensuring a constant distance between the anode wires and the pad plane over the full area of the TEC, the G10 is attached to a supporting aramid fiber (NOMEX, HEXCEL) honeycomb structure of 19.6 mm thickness followed by a second 300 μm thick G10 multilayer printed circuit board. This sandwich construction should keep the distance between anodes and pads constant to better than 100 μm. Electrical contact between the backside of the pad plane and the multilayer printed circuit board is achieved by means of small gold-plated beryllium springs contained in the honeycomb structure as detailed in Fig. 13.

The multilayer PCB backing will have four conducting layers to provide analog and digital power and grounds, as well as analog and digital connections. The density of traces will amount to an equivalent of 30 μm copper. The possibility of using aluminum traces for the power and ground distribution network is currently being investigated. Taking into account the lower conductance, this would decrease the radiation thickness to roughly 10 μm copper equivalent. The front-end electronics would be mounted on the top layer of the PCB. As maximum thickness of single electronics components we assume 7 mm. The wire chamber frames still need careful engineering based on finite element calculations in order to achieve the necessary rigidity while keeping the material budget as small as possible. The same is true for the design of the support structure for the complete set of TRD modules.

The material budget of the TRD as we currently foresee it is summarized in Table 2. The

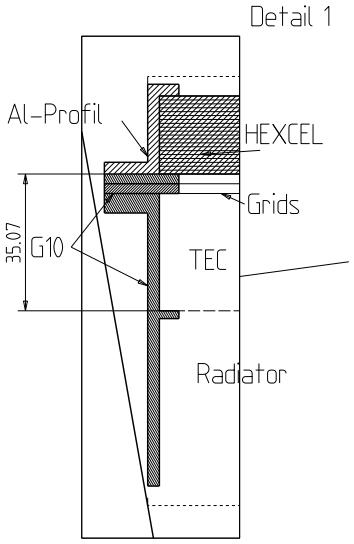

Figure 12: Cut through one side of a TRD readout chamber.

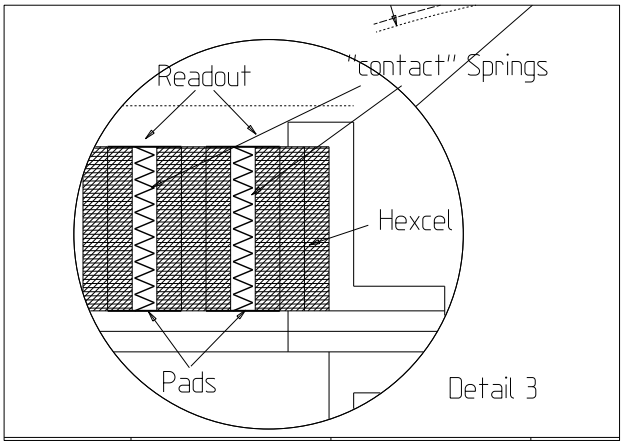

Figure 13: Cut through the backplane of the readout chamber showing the electrical contact between the two backings (pad plane and PCB) of the honeycomb material.

Element	Material	X/X_0 [%] at $\eta = 0$
radiator gas seal	G10 HEXCEL	0.18
radiator	polypropylene	0.40
radiator gas	CO_2	0.02
TEC gas	Xe + quench gas	0.23
cathode pads	Au-coated Cu	0.08
multilayer PCB	G10	0.16
FEE + signal lines	electronics + Cu	0.31
honeycomb support	NOMEX	0.25
cooling	H_2O + PE	0.07
1 TRD module		1.70
full TRD		10.20

Table 2: Material budget of the TRD. Only components contributing significantly in the detector's active area are listed.

frames of the radiator and the TEC and the support structure are not included. Choosing C_4H_{10} or CO_2 as quench gas in the TEC does not change the material budget significantly. The integrated FEE electronics will be mounted on multi-chip modules, which use standard laptop memory card edge connectors to connect to the top layer of the PCB. The size of the modules will be roughly 9 cm^2 per 72 cm^2 readout area. The total material will be equivalent to a continuous material layer of 0.25% X_0. Water cooling is foreseen for the cooling of the front-end electronics. The cooling pads will cover the chips on the multi chip modules. The pads will be flat panels of 2 layers of polyethylene of 1 mm thickness and a 1 mm water cooling channel covering about 10% of the active area of the detector. The material needed for that contributes another 0.07% X_0. A GALICE simulation has been performed to evaluate the occupancy in the TRD and to investigate the role of secondary particle production in the TRD as background source in the TRD itself and in other ALICE detector systems. In that simulation the wire planes of the TRD have been neglected. The radiator and wire chamber frames have been assumed to be carbon composite frames of 1 cm thickness and a skeleton-like support structure made of aluminum has been considered. The latter consists of profile tubes of rectangular cross section running in z-direction between the 18 TRD sectors. The dimensions of the profiles are 734 cm in z, 78 cm in r direction, and 40 mm in ϕ with a wall thickness of 5 mm. In the transverse direction we simulate the TRD support for the moment by 5 mm thick aluminum plates between the five TRD modules of each plane.

3.4 Radiators

For the radiator material one has, in general, the choice between regular foil stacks, fiber radiators, and heterogeneous foams. The latter have the advantage that they are much easier to handle and to produce compared to foil stacks where a regular spacing between the individual foils has to be maintained. This is difficult especially in the case of foil stacks covering a large area as foreseen in the TRD proposed here, since there the bending of the foils under the influence of the gravitational force cannot be neglected. Foil stack radiators, usually made of polypropylene foils, have the advantage that, if spaced regularly, produce 50% more TR photons than typical foam radiators of the equivalent thickness. This is demonstrated in Fig. 14 (taken from [21]). These data summarize results from radiator tests performed as part of the R&D program for the TEC/TRD presently being built for the PHENIX experiment at RHIC. Shown is the normalized yield of detected TR photons produced in one layer of various

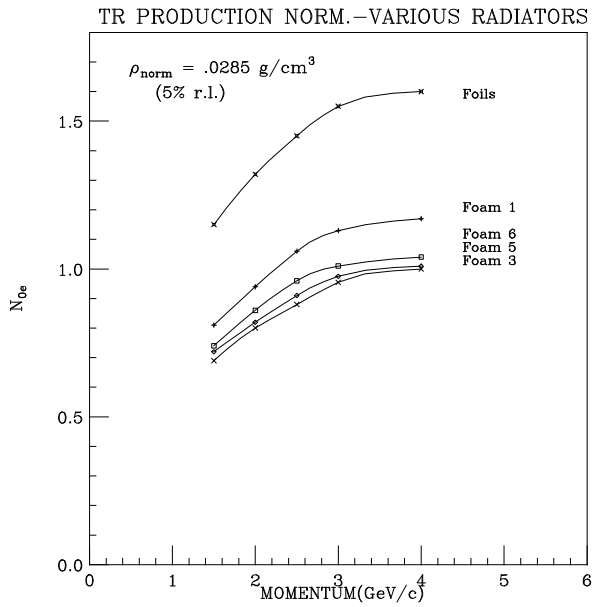

Figure 14: Normalized yield of detected TR photons produced in one layer of various radiator configurations as a function of the incident electron momentum (taken from [21]).

radiator configurations as a function of the incident electron momentum. As X-ray detector a modified version of the NA34 TRD [24] has been used. The X-ray absorbing xenon volume had a thickness of only 1 cm corresponding roughly to the mean free path of the X-rays, which means that about 30% of the produced TR photons remained undetected.

The question whether a fiber radiator, as recently chosen for the HERMES TRD [25], would meet our requirements in terms of performance and mechanical properties will be addressed in our forthcoming R&D program (see below). It has been shown already [22, 23] that the performance of such radiators can come close to that of foil stacks, but in order to minimize the material budget foils probably would be preferable.

Despite the technical difficulties mentioned above we currently foresee foil stacks as radiators for the ALICE TRD. The foil stack parameters have to be optimized in order to produce on average enough TR photons to ensure efficient pion rejection for momenta of about 1.5 GeV/c and above. Therefore, a Monte Carlo simulation, along the lines worked out in [20, 26], has been performed taking into account parameterizations of TR photon production, absorption of the X-rays in the foil stack itself and in the inactive parts of the TEC (the entrance foil of the chamber, considered to be mylar of 25 μm thickness), the energy loss of the primary charged particle in the TEC, and the detection of TR by photoabsorption in the TEC gas. Special attention has been paid to the delta-rays, as explained at the beginning of this section.

The results are summarized in Fig. 15. The left panel shows, as a function of the gap d_2 between the foils, the average number $\langle n_{\rm TR} \rangle$ of TR photons produced by electrons of 3 GeV/c momentum impinging perpendicular on a stack consisting of $N_{\rm f} = 100$ foils in a CO_2 atmosphere for three values of the foil thickness $d_1 = 15$, 20 and 25 μm. The average number of produced TR photons in one foil stack starts to saturate at a foil spacing of around 500 μm. Also visible is that changing the foil thickness from 20 to 25 μm hardly increases the TR photon yield.

The right panel of Fig. 15 shows the corresponding pion misidentification probability assuming

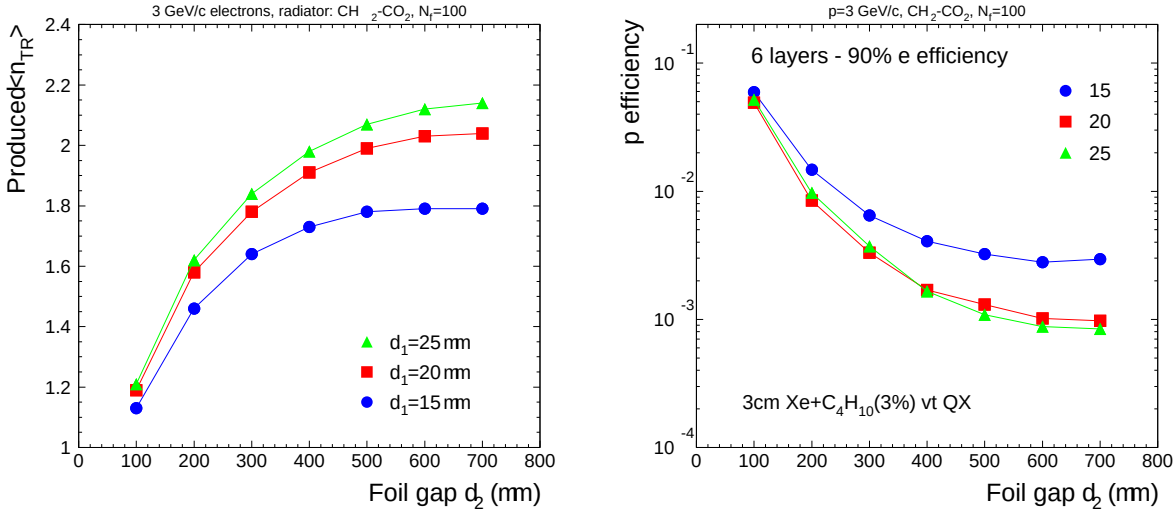

Figure 15: Simulation of the performance of a polypropylene (CH_2) foil stack in a CO_2 atmosphere.

a six layer TRD equipped with Xe/C_4H_{10}-filled TECs and applying cuts such that the electron identification efficiency is 90%. These results have been obtained using a bidimensional likelihood in cluster charge and position (QX method). One can see that choosing gaps of 600 μm between the individual foils one can still improve the pion rejection factor. However, taking into account that keeping the required regularity of the foil separation might be more difficult for such a large foil gap and that the fiber radiator option would mean a lower TR production, we used the value $d_2 = 400$ μm for the subsequent studies of the pion misidentification probability. In terms of foil thickness, $d_1 = 20$ μm is an optimum because the TR spectrum is harder for thicker foils and with increasing d_1 the chamber gets more and more transparent for the TR photons.

3.5 Time Expansion Chambers

The schematic layout of the TECs is shown in Fig. 4. In Section 3.2 the basic operation principle has been discussed and the mechanical structure is described in Section 3.3. Here we focus on the readout chamber and field configuration. The drift lines are shown for three drift cells in Fig. 16 for the actual chamber geometry and field configurations. The high voltage electrode at the entrance of the TEC ($y = 0.0$ cm in Fig. 16) is biased to -4.0 kV in case of the Xe/C_4H_{10} gas mixture and to -1.5 kV for Xe/CO_2 (see below). The drift region has a depth of 30 mm and is separated from the amplification region by a cathode wire plane consisting of copper-beryllium wires of 75 μm diameter which are connected to ground potential ($y = 3.0$ cm in Fig. 16). These wires run in ϕ-direction with a pitch of 5 mm and a distance from the cathode pad plane of 5 mm. The anode wire plane ($y = 3.25$ cm in Fig. 16) is biased to +1.6 kV. It comprises gold-plated tungsten wires of 25 μm diameter which run in ϕ-direction with 5 mm pitch and at a distance of 2.5 mm from the pad plane ($y = 3.5$ cm in Fig. 16). According to GARFIELD [27] calculations these configurations yield homogeneous drift fields of -1.36 kV/cm and -0.56 kV/cm for Xe/C_4H_{10} and Xe/CO_2, respectively, over the entire drift region. In the setup within the ALICE experiment the magnetic field of 0.2 T points in x-direction. $\vec{E} \times \vec{B}$ distortions near the wire plane are discussed below. Electron

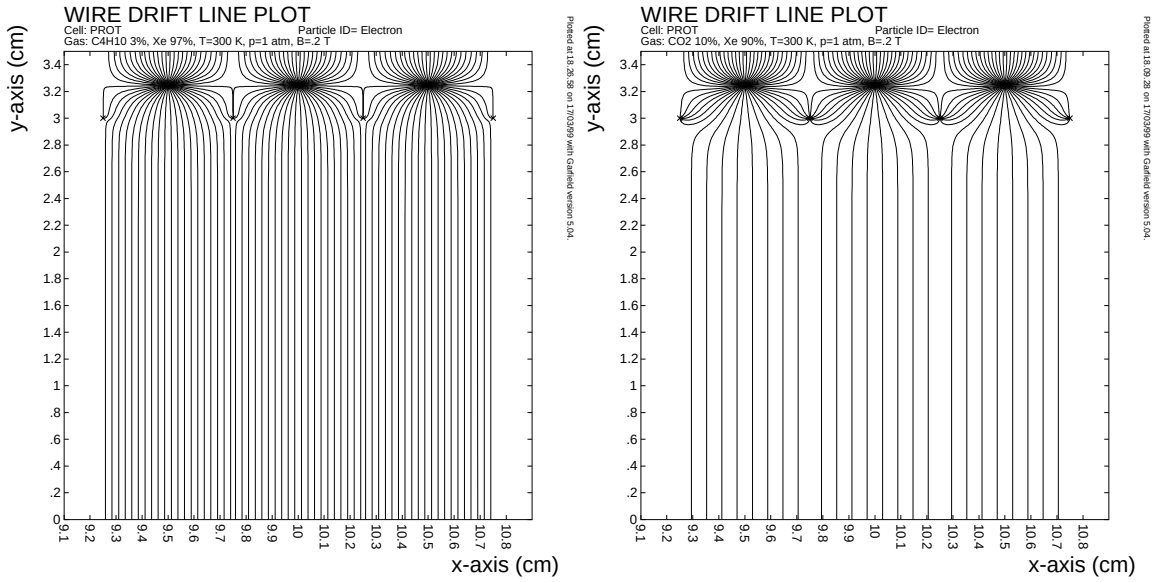

Figure 16: Drift lines for the proposed chamber geometry and field configurations with the gas mixtures Xe/C_4H_{10} (left panel) and Xe/CO_2 (right panel), respectively.

clusters produced at any location in the drift volume are collected on the anode wires without notable loss by charge collection on the cathode wires.

For efficient TR photon absorption the chamber gas has to be xenon rich. Two effects have to be taken into account when choosing the quench gas component. Due to the large flux of neutrons to be expected from Pb+Pb collisions at LHC the quench gas should ideally be free of hydrogen in order not to generate highly ionizing secondary protons inside the TEC's active volume. In that respect, a mixture of 90% Xe and 10% CO_2 at atmospheric pressure seems to be a reasonable chamber gas. Unfortunately, admixtures of CO_2 to noble gases are known to significantly increase the three body electron attachment which may result in some loss of electrons produced by the primary X-ray photoabsorption. If this issue turns out to be important an alternative choice could be 97% Xe and 3% C_4H_{10}, which is a gas mixture similar to the one considered for the PHENIX TRD. The question which gas mixture represents the better choice cannot be answered at the moment, since neither the secondary particle production by neutrons nor the signal loss by electron attachment have been quantified yet. These effects will be addressed in simulations and in our forthcoming R&D program (see below).

Calculations with MAGBOLTZ [28], taking into account the magnetic field, give a drift velocity of about 1.5 cm/μs for both gas mixtures resulting in maximum drift times of about 2 μs. The transverse and longitudinal electron diffusion constants have been calculated to be about 600 $\mu m/\sqrt{cm}$ and 170 $\mu m/\sqrt{cm}$, respectively, in the case of the Xe/C_4H_{10} gas mixture. The corresponding values for the Xe/CO_2 gas mixture are 230 $\mu m/\sqrt{cm}$ (transverse diff.) and 330 $\mu m/\sqrt{cm}$ (longitudinal diff.). The magnetic field results for both gas mixtures in a Lorentz angle of about 5° deflecting the drifting electrons along the wire direction.

For all TRD Monte Carlo calculations presented in this writeup we used Xe/C_4H_{10} as the gas mixture. Since electron attachment and neutron flux are not taken into account in the simulations, the TRD performance is completely determined by TR production in the radiator and TR absorption by xenon. Therefore, there is no significant difference between Xe/C_4H_{10} and Xe/CO_2 gas mixtures in the simulations.

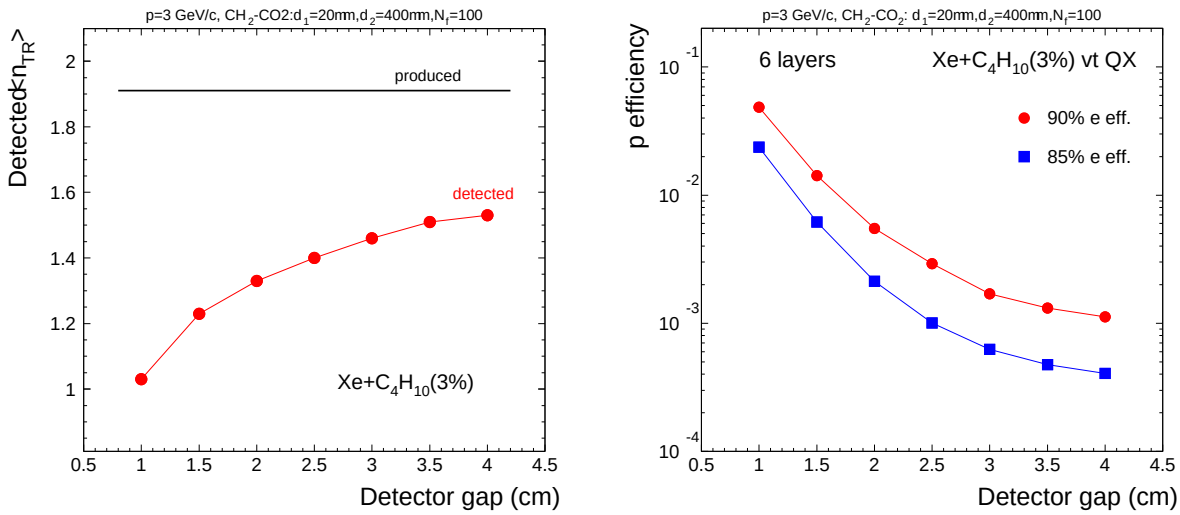

Figure 17: Average number of detected TR photons as function of the thickness of the TEC's gas volume for incident electrons of 3 GeV/c momentum (left panel) and pion efficiency as function of TEC thickness for 85 % and 90 % electron efficiency (right panel).

For many reasons the overall depth of the gas volume should be as small as possible but at the same time it has to be large enough to ensure efficient X-ray absorption and to allow for a better pion rejection by exploiting the position information of the clusters.

Fig. 17 shows in the left panel the simulated dependence of the average number of detected TR photons on the depth of the TEC gas volume for electron tracks normal to the TRD with a momentum of 3 GeV/c. The right panel presents the pion misidentification probability for electron efficiencies of 90% and 85%, obtained with a 6 layer TRD. Fig. 17 demonstrates that about 70% of the X-rays are absorbed already in the first 2 cm of the Xe/C_4H_{10} mixture. Nevertheless, a deeper gas volume will clearly help to distinguish TR signals from fluctuations in the energy loss of charged particles by ionization (cf. Fig. 5). Increasing the depth of the TEC's drift region beyond 3 cm improves the TRD performance marginally, therefore for the moment we consider 3 cm as the desirable depth of the drift volume. Given the large area covered by the TRD, the depth of 3 cm and the additional amplification region of the TEC with a depth of 5 mm result in an overall active volume of about 28 m^3 to be filled with the counting gas. In view of the price of xenon it is obvious that a careful design of a recirculating gas system, which has to ensure an efficient purification of the gas and a minimum leakage rate, is mandatory.

In order to define the necessary granularity of the TRD a full GALICE simulation has been performed. The event generator SHAKER [29] has been used with the assumption that in a central Pb+Pb collision at LHC 8000 charged particles are produced per unit of rapidity. Particles were generated within the pseudorapidity interval $|\eta| < 1.5$. The production of secondary particles in the material of the full ALICE setup including the TRD itself has been taken into account. The energy deposition in the TEC was treated identical as in the simulations explained above, but no transition radiation was considered. Fig. 18 shows the occupancy (defined as the number of time bins over the threshold over the total number of time bins) of the TEC as function of threshold for three values of the pad size, 3.0, 4.5 and 6.0 cm^2. The threshold is expressed in number of electrons, after gas amplification, considering a gas gain of $2{\cdot}10^3$. In these terms a value of 1/20 from the most probable value of the energy deposit of a MIP would correspond to about 2000 electrons per time bin. At this value, which is considered an optimal threshold for a reliable charge division for position

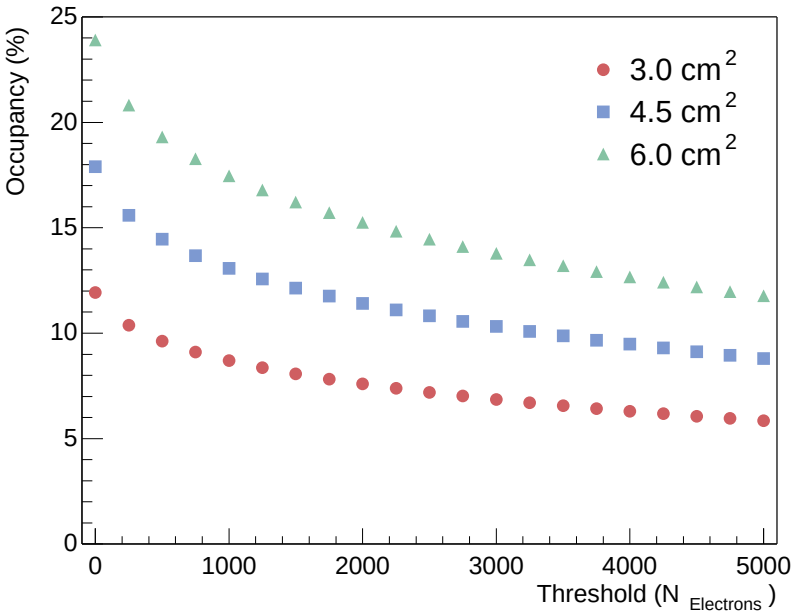

Figure 18: TEC occupancy as function of threshold for three values of the pad size, as obtained with a GALICE simulation.

reconstruction and tracking for MIPs, the occupancy for 4.5 cm^2 pads is around 12 %. For this pad size, which is our present choice (see the trigger requirements, Section 6) the expected noise is around 1000 electrons. A pad size of 4.5 cm^2 leads to a total of 1.2 million readout channels. The above occupancy calculations have been done for the first TRD layer. Due to the geometry, for the outer layers the same occupancy can be achieved with bigger pads. The design of the cathode pad planes allows to adjust the pad size in steps of 0.5 cm^2 (see below), by connecting together 9 or more individual chevron units (as sketched in Fig. 19).

Although particle production in the TRD is moderate, it contributes significantly to the occupancy in the TEC, especially in the outermost plane where roughly 30% of all hits are due to secondaries produced in the TRD itself. The influence of these secondaries on the other ALICE detectors is discussed in Section 3.6.

The shape of the individual cathode pads has to be optimized for position resolution in ϕ-direction while the resolution in z-direction is of less importance. We propose to use displaced single chevron pads [30] which, by geometric charge division, yield a rather precise centroid determination of spatially extended charge signals induced on the cathode plane. The general layout of a cathode pad plane with chevron-shaped pads is shown in Fig. 19.

Following the empirical Mathieson formalism [31] calculations have been performed of the charge distribution induced on the pad plane and the charge sharing between adjacent pads of w=10 mm width, made from units of length s=5 mm. This implies that the area of each individual unit is 0.5 cm^2. Based on these calculations we optimized the overlap factor f_{x} of the pads and the distance h between the anode wires and the cathode pad plane. The results are summarized in Fig. 20. To find the optimum overlap factor $f_{\mathrm{x}} = 1.0$ the differential nonlinearity (DFNL) has been calculated according to:

$$\mathrm{DFNL} = 2\,\frac{\mathrm{UIR}_{\max} - \mathrm{UIR}_{\min}}{\mathrm{UIR}_{\max} + \mathrm{UIR}_{\min}} \qquad \mathrm{UIR} = \left(\frac{\mathrm{d}\phi_{\mathrm{rec}}}{\mathrm{d}\phi}\right)^{-1} \tag{1}$$

Here, the UIR is the uniform irradiation response and ϕ_{rec} is the ϕ position reconstructed from the induced charge distribution. In practice, f_{x} should be increased to about 1.05 to

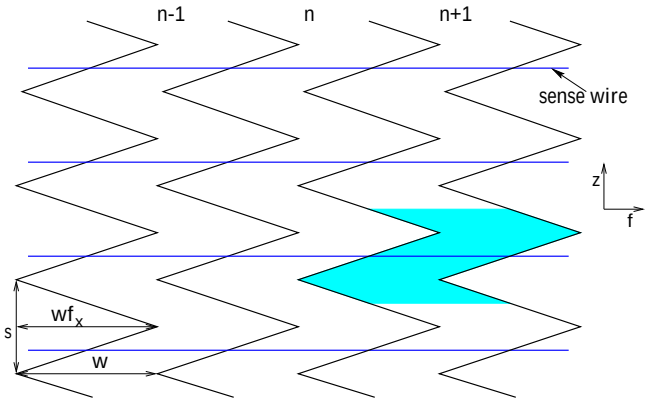

Figure 19: General layout of the chevron cathode pad planes. The blue shaded area corresponds to one individual unit. Here, w denotes the width, s the length, and f_x the so-called overlap factor of the pads. Anode wires with spacing s run in ϕ-direction. In z-direction several units of one row are coupled together to form one pad which corresponds to one readout channel.

take into account the finite separation between the individual chevron pads [30].

The calculation of the systematic position error $\Delta\phi = \phi_{rec} - \phi$ as a function of the true position ϕ for different values of the wire plane distance h shows that for h = 2.5 mm $\Delta\phi$ is less than 5 μm. In addition to this systematic contribution to the overall spatial resolution, the statistical contribution cannot be neglected. This term is to a large extent determined by the electron statistics and the overall noise behavior of the detector. Due to the small drift length, diffusion of the drifting electron cloud and the track angle with respect to the pad orientation play a minor role. The performance of existing similar wire chambers [32, 33] gives us confidence that an overall position resolution better than 200 μm can be achieved with the proposed design. To meet the requirements in terms of maximum occupancy we

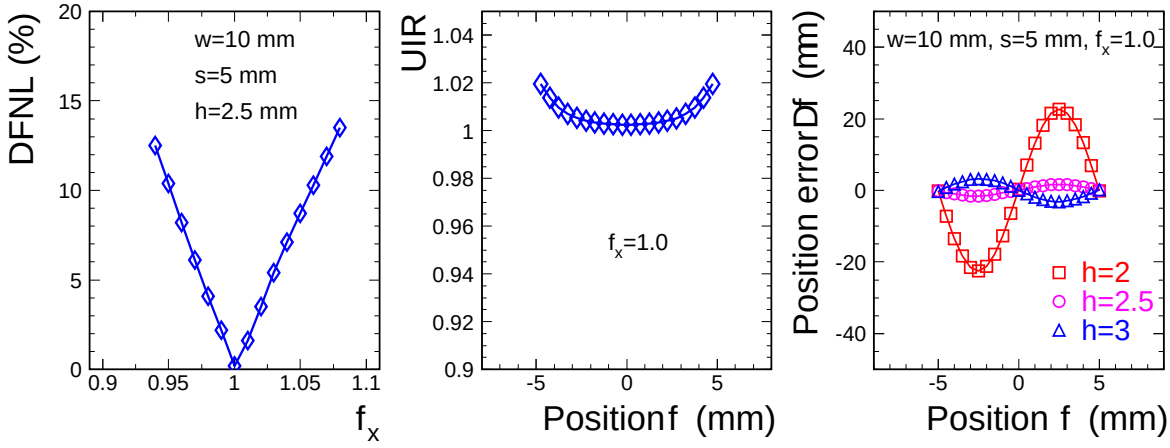

Figure 20: Optimization of the parameters of the chevron cathode pad planes. The differential nonlinearity as function of the overlap factor is shown in the left panel. As function of the true position in ϕ we plot the uniform irradiation response in the middle panel and the position error for different values of the distance between anode wires and pad plane in the right panel. Refer to the text for the definition of all quantities.

currently plan to couple together several chevron units in z-direction to form one readout pad. As mentioned above, the chosen chevron shape then allows to adjust the size of the individual readout nodes in steps of 0.5 cm^2.

3.6 Expected performance

A TRD has to be designed to minimize the probability to misidentify a pion as an electron at a fixed electron efficiency of, e.g., 90%. Since the design proposed for the ALICE TRD is similar to that of the PHENIX tracking TRD, we show in Fig. 21 the pion rejection power that has been determined in the PHENIX R&D program [34] together with results we have obtained in a TR simulation of the ALICE TRD design. For momenta above 2 GeV/c a pion rejection factor higher than 500 can be reached with the proposed design. From the simulation

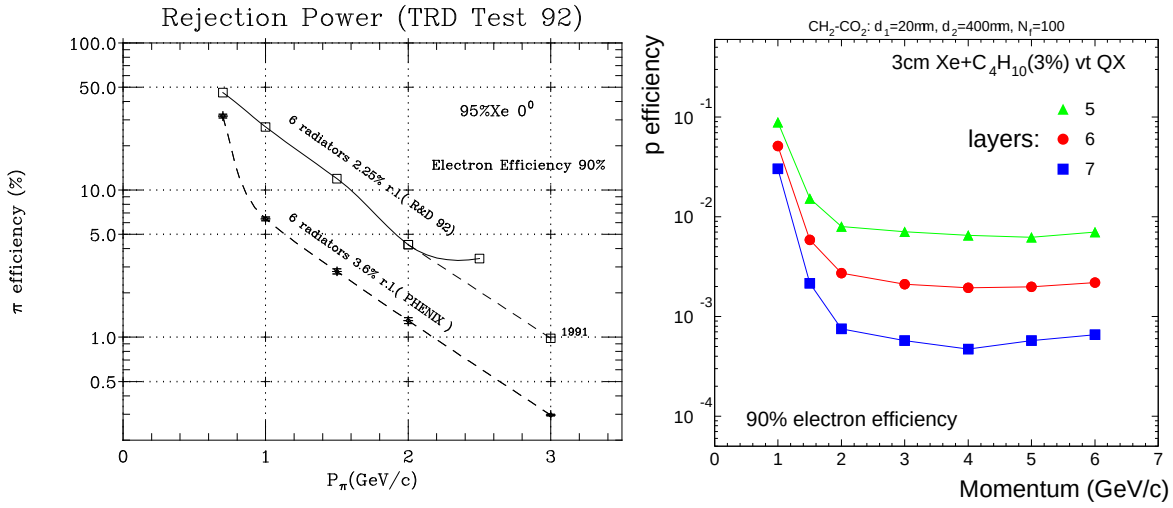

Figure 21: Probability to misidentify a pion as an electron as function of the momentum at a fixed electron efficiency of 90%. Results of the R&D program for the PHENIX TRD are shown in the left panel (taken from [34]). The right panel shows results from the simulation of the TRD proposed for ALICE for a total of 5, 6, and 7 radiator/TEC planes.

results one can, furthermore, conclude that the TRD performance depends strongly on the number of radiator/TEC planes. Reducing the TRD depth by one plane decreases the pion rejection capability by more than a factor of 3 for momenta above 2 GeV/c (see also Fig. 6).

A second important issue is the question whether secondary particle production in the TRD is an important source of background for the TRD itself and other ALICE detectors. While the effect on the TRD has been discussed already above, Fig. 22 summarizes the influence on the TPC and the HMPID. Again, these spectra have been obtained with a full GALICE simulation based on the primary production of 8000 charged particles per unit of rapidity.

Obviously, backscattering of secondaries from the TRD into the TPC can almost be neglected. Mainly pions of low momentum but also a few protons and even deuterons are observed. The overall increase of the TPC occupancy is less than 1% both on the particle and on the hit level if one adds the TRD to the ALICE setup. This is true even close to the outer border of the TPC. For the case of the HMPID the occupancy increase caused by the TRD still is only about 8%. It appears that the presence of the TRD in the ALICE setup does not do harm to the TPC or to the HMPID.

These results have been obtained with the initially considered version of the mechanical

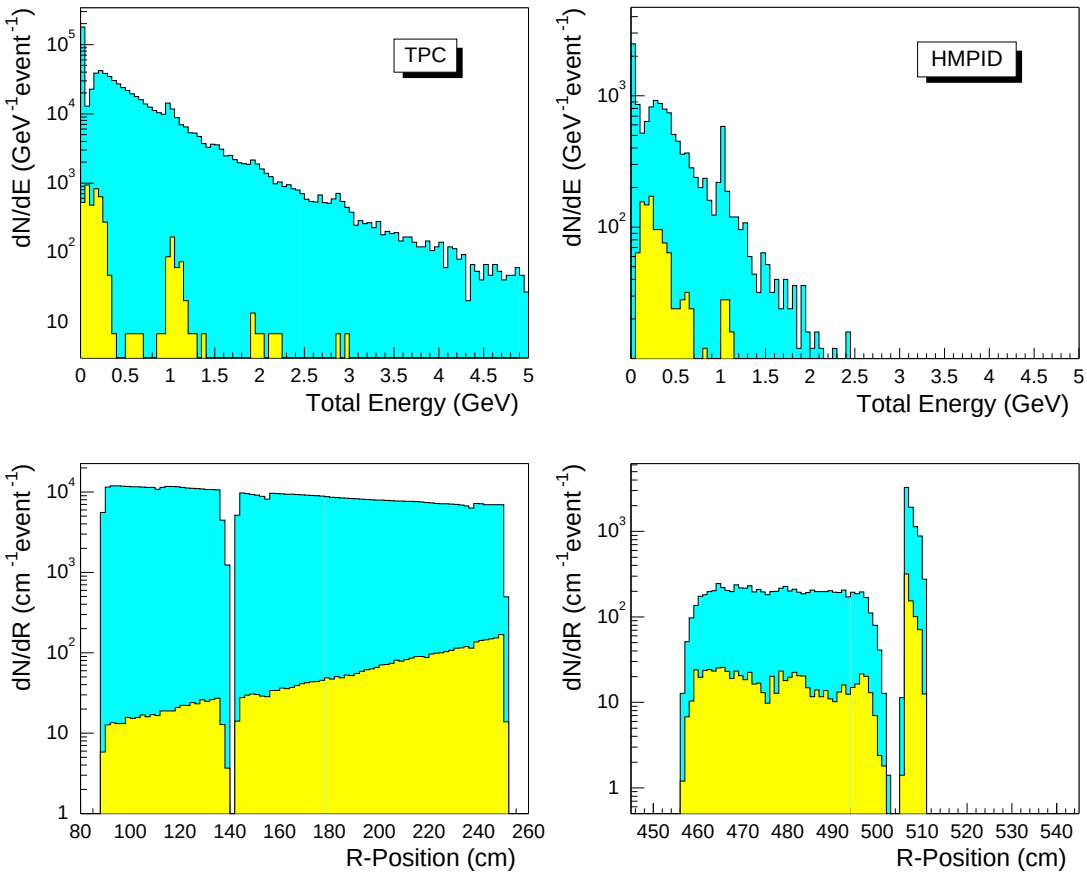

Figure 22: Particles seen in the TPC (left panels) and in the HMPID (right panels). The upper panels show the total energy distribution of particles per event. In the lower panels the hit distributions per event are plotted as function of the radial distance from the beam axis. In each panel the blue histograms represent all particles while the yellow ones reflect the contributions of secondary particles produced in the TRD.

support structure consisting of four segments along z-direction. With the present structure, divided according to the dead zones of the HMPID (cf. Section 3.3), the number of TRD secondaries in the HMPID will even decrease.

3.7 Forthcoming R&D program

Extensive R&D studies are foreseen to address the open questions in the TRD design and to optimize the detector parameters. For that purpose a TRD prototype with an active area of 47×50 cm^2 is currently being built at GSI. The prototype setup follows to a large extent the design of the radiator/TEC combination proposed for the ALICE TRD in this writeup. The radiator and wire chamber geometries will be identical. For the first tests the TEC's cathode pad plane will be built in the standard pc-board technique. A thin G10-NOMEX honeycomb pad plane will be introduced as a next stage. Otherwise, the layout of the pad plane corresponds to that described above. Since dedicated TRD electronics first needs to be developed, we will start our R&D program with a 100 MHz FADC system and appropriate discrete preamplifiers and shapers available at GSI. For in-beam tests of the prototype we plan to make extensive use of the pion beam facility which went into operation at GSI recently [35]. A secondary beam of pions, muons, and electrons is available with intensities up to

10^5/s. Particle momenta between 0.5 GeV/c and 2.8 GeV/c can be selected. The electron content in the mixed beams decreases in the relevant range of particle momenta from about 10% at 1.0 GeV/c to about 0.1% at 2.8 GeV/c. The first test experiments are planned for June 1999. Finally, we list the topics we want to address in the forthcoming R&D program by systematic studies:

- comparison of various radiator materials (foil stack or fiber radiators) and dimensions;
- test of alternative gases (e.g. He) for the radiator atmosphere;
- optimization of the TEC's gas mixture in terms of drift properties and electron attachment;
- optimization of the field configuration in the TEC;
- confirmation of the expected position resolution of the TEC;
- test and comparison of thick (pc-board) and thin (honeycomb) pad planes;
- development and test of front-end electronics;
- development and optimization of pattern recognition and trigger (see below) approaches.

4 Physics capabilities

4.1 Description of the simulation environment

In order to quantitatively evaluate the di-electron physics possibilities with the ALICE detector including the TRD, we have performed simulations with a large number of events. To obtain the necessary speed the detector was only included schematically, as discussed below[2].

In total, 10^5 events were generated with realistic particle multiplicities using the program SHAKER [29] with empirical parameterizations of the transverse momentum spectra of the various particle species. The rapidity distribution is assumed to be flat around midrapidity. The total charged particle density was chosen to be $\mathrm{d}N/\mathrm{d}y = 8000$ for central collisions. D and B mesons, which turn out to be important for the electron spectra, were added with multiplicities according to [5], e.g. no reduction due to parton energy loss was used. Similarly, J/Ψ and Υ yields were extrapolated from pp collisions without any suppression factor. In order to get acceptable statistical errors their yield was artificially enhanced to 100 per event. This enhancement was properly taken care of in the analysis steps by rescaling. The uncertainties in the yields of primary particles have to be kept in mind when discussing the results of the simulations.

Particles with rapidities of $|y| < 1.5$ were propagated through the detector by means of the GEANT 3.21 based program GALICE (version 2.05) with all the GEANT physics options turned off except for the finite lifetime of the particles. All decays were handled within GALICE by calling the proper JETSET subroutines. This allows to go beyond the 3 particle decay limitations of GEANT and is essential when including B and D meson decays in the simulation. The momenta and vertices of all charged particles and of their secondary decay products were registered keeping the parent information. This allows to trace back the composition of final spectra under complicated multidimensional cuts.

The detector response was modeled schematically by the following cuts and folding procedures:

1. Applying a polar angle cut of $45° < \Theta < 135°$.
2. Applying a vertex cut of $v_\mathrm{t} < 3$ cm to eliminate a large fraction of all photon conversions (v_t is the distance between the track vertex and the interaction point).
3. Folding the primary momenta with the detector resolution as given in the ALICE Proposal. For a nominal magnetic field of $B = 0.2$ T a mass resolution of $\sigma = 31$ (138) MeV/c^2 is obtained for the J/Ψ (Υ). The mass resolution improves to 16 (70) MeV/c^2 if the magnetic field is increased to $B = 0.4$ T. Thus for the high field setting the excited states of the Υ can be resolved.
4. Applying a minimum transverse momentum cut of $p_\mathrm{t} > 0.25$ GeV/c, motivated by the availability of particle separation within ALICE.
5. Removing electron tracks according to the finite detection efficiency ($\epsilon = 0.9$) when applying particle identification cuts ($\epsilon = 1$ for perfect particle identification).
6. Reassigning the particle identity according to the particle identification capabilities of the detector components. Several scenarios are shown in Fig. 23 and listed in Table 3.

[2]Note that the occupancy calculation, discussed in the previous section, contained a detailed detector description, including secondary particle production, and no track specific cuts.

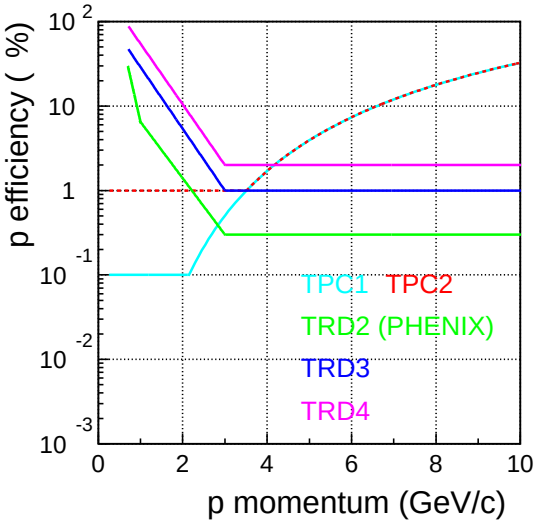

Figure 23: Pion rejection capabilities of the various detector components. The probability to misidentify a pion as an electron is plotted versus the pion momentum for an efficiency of 90% to detect the electron.

For the case where both TPC and TRD are available for ALICE the total detector response is a combination of the TPC and TRD performances. If not specified explicitly in the following the TRD scenarios are including the more realistic TPC2 performance parameterization with a pion rejection efficiency of 99% for pion momenta below 3 GeV/c. Note that the TRD2 option is a parameterization of the TRD response presented in Fig. 21 that was experimentally achieved within the PHENIX R&D program.

The resulting inclusive transverse momentum distribution of electrons is shown in Fig. 24. Major sources of electrons are π°, η, D and B mesons. They exceed the yield from interesting sources such as J/Ψ, Υ, Drell-Yan (DY), etc. by orders of magnitude. The aim of the simulation is to demonstrate how and to which extent one can extract physics signatures taking into account the full complexity of LHC Pb+Pb events.

Table 4 lists both the primary multiplicity of particles in the rapidity interval $|y| < 1.5$ and the number of electrons they contribute within the cuts listed in the figure caption, roughly corresponding to the acceptance of the detector.

With about 30 electrons with $p_{\mathrm{t}} > 0.25$ GeV/c (see Table 4) emitted per event the challenging problem at LHC is the control of the combinatorial background. According to Table 4 Dalitz decays of π° and semi-leptonic decays of D mesons contribute about 40% each to the total number of real electrons within one event. Conversion electrons generated from the decay

Option	Description	Comment
PERF	perfect particle identification	best case reference
TPC1	PID with TPC based on dE/dx only	optimistic parameterization
TPC2	PID with TPC based on dE/dx only	realistic parameterization
TRD2	PID with TPC&TRD(PHENIX prototype)	TRD Depth: 70 cm
TRD3	PID with TPC&TRD(reduced resolution)	TRD Depth: 40 cm
TRD4	PID with TPC&TRD(reduced resolution)	TRD Depth: 30 cm

Table 3: Particle identification scenarios considered in the simulation.

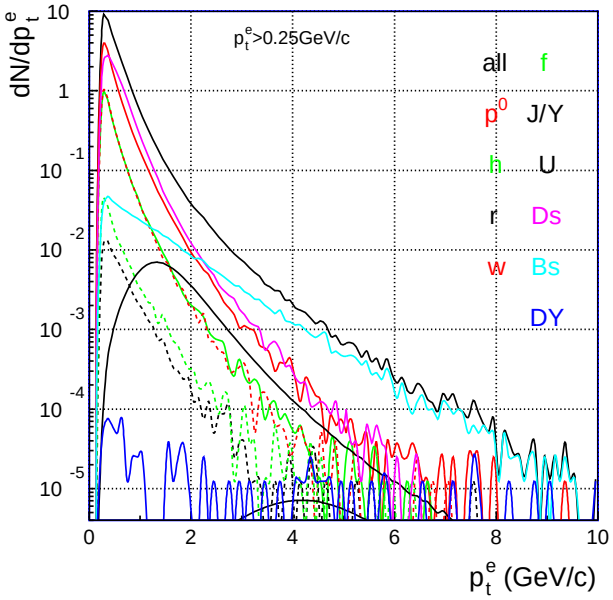

Figure 24: Transverse momentum spectrum of single electrons into the TPC acceptance for the reaction Pb+Pb at $\sqrt{s} = 5.5$ TeV.

Table 4: Integrated electron yields for the reaction Pb+Pb at $\sqrt{s} = 5.5$ TeV obtained under the following cuts:
$|y| < 1.5$,
$45° < \Theta < 135°$,
$0.25 < p_t < 15$ GeV/c,
$v_t < 3$ cm.

	SHAKER	$e^{\pm}$ after decays and cuts	
particle	# primaries	#	<p_t> (GeV/c)
ρ^o	6000	11.446	0.473
h	1005	2.686	0.465
$\rho^{\pm}$	2 × 6000	0	---
$p^{\pm}$	2 × 450	0	---
$K^{\pm}$	2 × 675	0.056	0.377
K^o	2 × 675	0.249	0.368
r	1800	0.061	0.639
w	1680	2.773	0.456
f	195	0.146	0.558
J/Y ($e^{\pm}$)	9.3×10^{-2}	0.101	1.593
U ($e^{\pm}$)	2.22×10^{-4}	0.0002	4.408
$D^{\pm}$	2 × 33	4.472	0.551
D^o	2 × 96	6.078	0.554
$D_s^{\pm}$	2 × 18	1.181	0.531
$B^{\pm}$	2 × 1.2	0.207	1.304
B^o	2 × 1.2	0.237	1.240
$B_s^{\pm}$	2 × 0.3	0.062	1.253
DY	0.0078	0.0012	2.999

photons are not included in the present analysis since they are originating from the interaction with detector material outside of our primary vertex window of $v_t < 3$ cm. The number of electrons is augmented by the number of pions that are misidentified as electrons and, consequently, pass the particle identification cuts. Therefore, the background depends on the pion rejection that one can achieve within a certain detector scenario.

As is visible from Fig. 25, applying the particle identification available from the TPC only results in a combinatorial background that is more than 2 orders of magnitude above the signal in the resonance peaks of J/Ψ and ϒ. (Note that the analysis of the continuum part of the correlations within one event (*comb.*) is indistinguishable from the results when combining electron candidates from different events (*mix.*).) Even applying the very optimistic version of the TPC1 response would not solve the problem. The combinatorial background due to misidentified pions essentially eliminates all di-electron physics capabilities with the TPC alone.

Therefore, an additional detector is necessary to perform the di-electron physics program outlined in the beginning of this report. As an example the results for the scenarios TRD2 and TRD4 are also shown in Fig. 25 demonstrating how additional pion rejection leads to a significant reduction of the combinatorial background. Depending on the quality of pion rejection a detector performance close to an ideal detector (PERF, black lines) can be reached. For the TRD2 case, resonance peaks are visible in the simulation even without any background subtraction. A signal can be derived as in the experiment by subtracting a mixed event background distribution (solid lines) from the invariant mass distributions where all e^+e^- pairs are included within one event (dashed lines). At this level unavoidable physics sources of electrons are dominating the combinatorial background. Within the current simulation scheme for the reconstruction of the invariant mass distribution of e^+e^- pairs the following processes are included in the simulation and can be evaluated quantitatively:

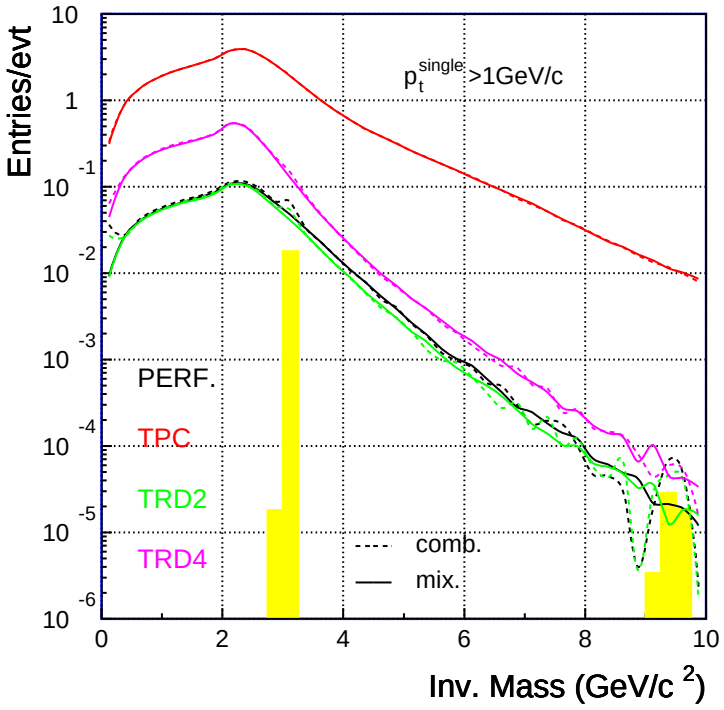

Figure 25: Invariant mass spectrum of e^+e^- candidate pairs. A $p_t > 1$ GeV/c cut was applied to all electron candidates. The lines correspond to different electron identification schemes shown in Fig. 23.

- particle identification;
- vertex distributions;
- transverse momentum cuts;
- Dalitz decays (π°, η, ...);
- semi-leptonic decays of D and B mesons.

The excellent impact parameter resolution of tracks (minimal distance to primary vertex in transverse ($d0$) and longitudinal direction ($z0$)) as shown in Fig. 26, in combination with the knowledge that the high yield of D and B mesons is contributing significantly to the high momentum tails of the electron spectrum (Fig. 24), allows to further reduce the combinatorial background. Fig. 27 shows a plot of $d0$, folded with resolution, for electrons from various sources with transverse momenta $p_{\rm t} > 1$ GeV/c.

Beyond a distance of 160 μm the spectrum is mainly determined by electrons from D meson decays. Finally, beyond distances of 300 μm electrons from B meson decays dominate. While this distribution suggests the exciting possibility to perform a direct measurement of the inclusive yield of open charm and open beauty (see Section 4.4), one can also turn things around and exploit the above impact parameter distributions to reduce the combinatorial background for all the sources originating from the primary vertex.

The resulting invariant mass spectrum, comparable to Fig. 25, with a momentum dependent vertex cut on the $\pm 2\sigma$ level in $d0$ and $z0$, is shown in Fig. 28. It demonstrates a) that the improvement for detector concepts that suffer from a large pion contamination (TPC) is marginal, and b) that for clean electron samples (PERF) a substantial reduction of the background can be achieved. Realistic TRD scenarios are located between those extremes. More details will be given in the following subsections, where the various physics signals are discussed, including the choice of transverse momentum cuts and the quality of Dalitz rejection strategies. Since the optimum cuts depend on the specific physics observable, no general numbers will be given here.

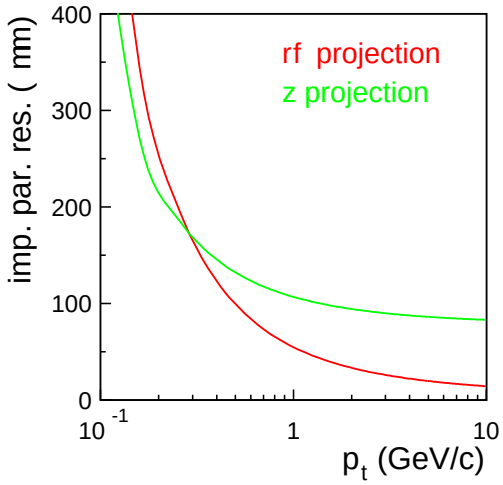

Figure 26: Bending ($r\phi$) and non-bending (z) projections of the impact parameter resolution for electrons (taken from the ALICE Proposal [1]).

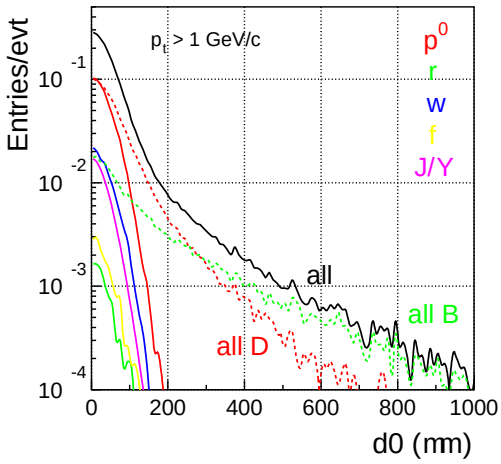

Figure 27: Distribution of minimum transverse distance to primary vertex for electrons with transverse momenta of more than 1 GeV/c originating from different parent particles. The effect of track resolution is included.

Numerical fluctuations are still visible even with 10^5 events in the region of invariant masses larger than 7 GeV/c^2 (dashed curves in Figs. 25 and 28). They can be recognized by comparing to the mixed event analysis, where the two electrons originate from different events. Much higher statistics is available for the mixed event analysis allowing for a more accurate determination of the background level. In this range the determination of the signal is most reliably done by directly combining the proper pairs as known by the parent identification. The directly computed signal is shown in Figs. 25 and 28 by the yellow areas. With sufficient

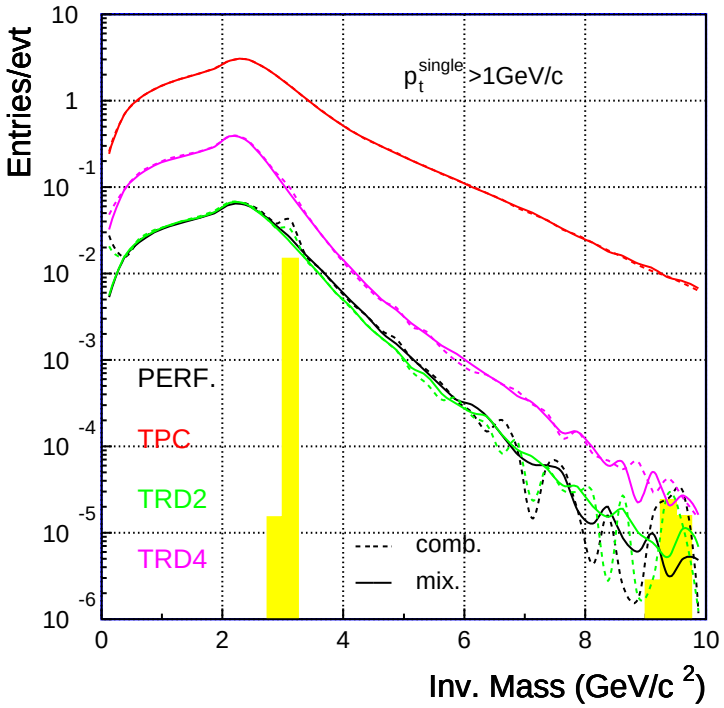

Figure 28: Invariant mass spectrum of e^+e^- candidate pairs with p_t dependent $\pm 2\sigma$ vertex cuts on $d0$ and $z0$. A p_t^{single} cut of 1 GeV/c was applied to all electron candidates. Different lines correspond to different electron identification schemes.

statistics, e.g. in the J/Ψ region, it was verified, that both methods, direct reconstruction and subtraction of combinatorics and mixed event spectra yield the same results.

4.2 Heavy vector meson resonances

J/Ψ and ϒ yields and their possible suppression relative to open charm or open beauty production are of prime interest for studying the properties of the QGP. Important information is expected in the p_t dependence of the signal (suppression). Since the signal is decreasing rapidly with p_t one has to confirm that the various scenarios cover a sufficiently large range in p_t to extract the physics signature.

Heavy vector meson detection capabilities of the detector were studied mostly for the J/Ψ for statistical reasons. Taking the integral results from Fig. 28 allows the statement that ϒs will be measurable at least with the same signal-to-background ratio, albeit with much reduced statistics (10^{-3}).

As can be seen from Fig. 24, rather high single leg momentum cuts can be used without compromising on efficiency. A more detailed analysis is shown in Fig. 29 where the signal and the signal-to-background ratio (S/B) are plotted versus the cut-off momentum. The signal was extracted by subtracting the invariant mass spectrum of the mixed event background from the combinatorial one within an event and integrating over a $\pm 2\sigma$ interval around the nominal mass. The signal was scaled to $5 \cdot 10^7$ central events, roughly corresponding to one year of ALICE running. A signal of about 10^6 J/Ψ decaying into the e^+e^- channel is expected (PERF) of which about $5 \cdot 10^5$ can be reconstructed making use of the TRD scenarios described earlier.

For all scenarios considered, the signal strength stays constant up to transverse momenta of $p_t = 0.8$ GeV/c. Having the PID capabilities of the TPC only does not allow to extract any reliable signal since the S/B is below 5% and it is therefore not plotted in Fig. 29. The S/B ratios vary significantly when choosing different pion suppression levels. With a momentum cut-off of $p_t = 1.0$ GeV/c the TRD3 (TRD2) parameterization allows to reach a S/B of

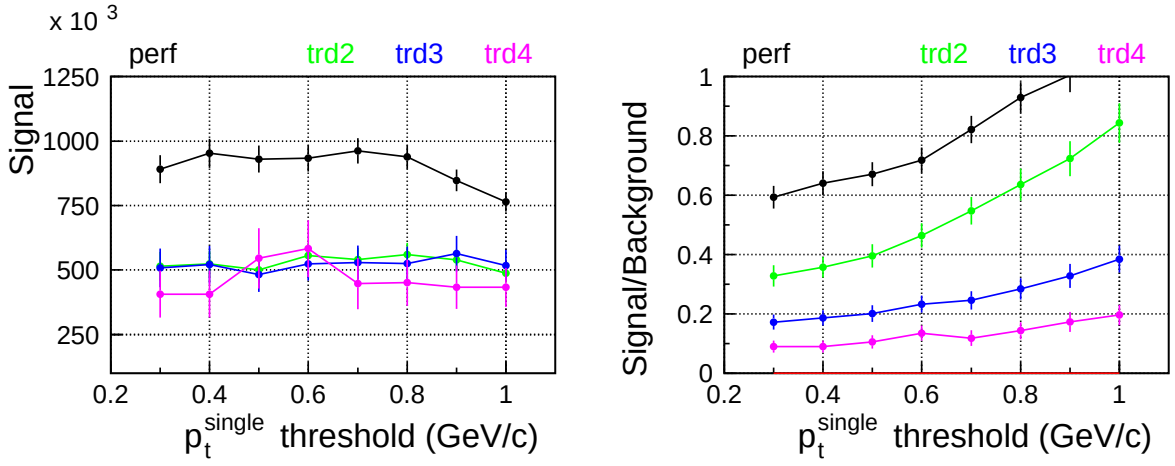

Figure 29: Single leg transverse momentum dependence of the signal and the signal-to-background ratio for the J/Ψ for various detector scenarios. The event sample consists of 10^5 central events. The data and the background were evaluated with 2σ cuts around the mean value. The signal is scaled to the statistics available within one year of ALICE operation with 40 central events taken per second.

0.39 (0.84) corresponding to 34% (73%) of the ideal case (PERF). Without vertex cuts the signal-to-background ratio would be worse by a factor of about 1.40 (1.55) (compare Figs. 25 and 28).

Good pion suppression is essential when measuring the J/Ψ p_t spectrum. In Fig. 30 we show how the performance of the considered detector versions depends on the e^+e^- pair momentum. The results were obtained using a single particle cut of $p_t > 0.8$ GeV/c. The full size TRD option traces the curve of the PERF parameterization while for reduced TRD substantial losses in the signal-to-background ratio are found. For the version TRD4 the S/B drops below 10% for J/Ψ momenta above 2 GeV/c. This makes a reliable measurement of the p_t dependence doubtful, especially since the J/Ψ could be in addition strongly reduced due to the presence of the QGP. Already the TRD3 version, however, shows a S/B ratio that is within the available accuracy independent of the J/Ψ transverse momentum and would thus allow to cover this important physics aspect. In order to visualize the quality of

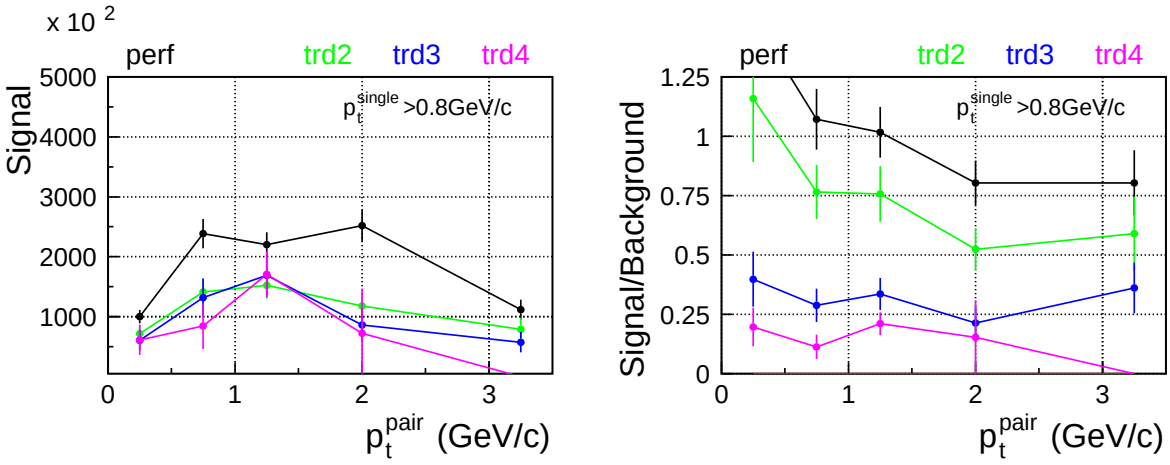

Figure 30: Pair transverse momentum dependence of signal and signal-to-background ratio for the J/Ψ for various detector scenarios. Conditions and color codes are the same as in Fig. 29.

reconstruction, Fig. 31 displays the invariant mass spectra in the J/Ψ region for a momentum interval of $2.5 < {p_t}^{\rm pair} < 4$ GeV/c for three different TRD scenarios. On the left side the TRD4 parameterization with a pion rejection of 98% was used, while the right side corresponds to the TRD2 situation where the pion rejection capability is 99.7%. Within the available statistics the left hand spectrum does not allow the extraction of any signal, thus demonstrating the importance of sufficient pion rejection at large momenta. It is also worth mentioning that the study of the momentum dependence of J/Ψ suppression will face decreasing signal strength and increasing background levels (see Fig. 2). Aiming to cover a substantial ${p_t}^{\rm pair}$ interval thus requires a maximum pion suppression. We note in passing that, at LHC energies, measuring the transverse momentum dependence of J/Ψ (and other quarkonia) production is particularly important as J/Ψ may be regenerated by collisions between D mesons. If this process is important then the D mesons will have thermal momentum distributions with typical hadronic temperatures (of order 160 MeV). Hence, one would expect a much softer transverse momentum spectrum for those J/Ψ mesons resulting from regeneration compared to those produced during the early phase of the collision.

Conclusions:

1. J/Ψ physics is not feasible with the TPC alone; additional particle identification appears

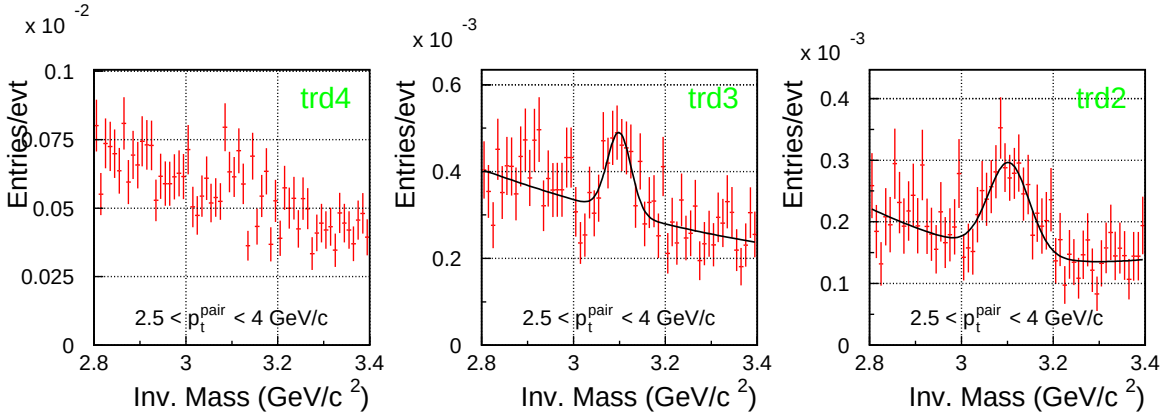

Figure 31: Invariant mass distribution of e^+e^- pairs in the J/Ψ region for large pair transverse momentum. Subtracted distributions are shown for the detector scenarios TRD4 (left), TRD3 (middle) and TRD2 (right). Error bars correspond to 10^5 events.

absolutely necessary.

2. Possible J/Ψ suppression requires a safety factor in the signal-to-background ratio and strongly favors the TRD performances like TRD3 or better.

3. D and B meson decays add substantial background. However, in the e^+e^- channel their contribution can be suppressed significantly by cutting out tracks with displaced vertices.

4. ϒ states are resolved with a signal-to-background ratio of 2:1 for the TRD2 option.

4.3 Light vector meson resonances

Light vector mesons (ρ, ω, ϕ) carry information about the restoration of chiral symmetry since their masses and decay width might be influenced by the properties of the surrounding medium. Since these medium modifications are also momentum dependent a sizeable fraction of the phase space (p_t) should be covered in order to reveal meaningful information.

Inspection of Fig. 1 and 24 demonstrates, however, that the reconstruction of light vector mesons is a very demanding task. The expected signal strength for the ω and ϕ meson is, because of the small di-electron branching ratio, an order of magnitude smaller than that for J/Ψ, with comparable background contributions. In addition, electrons originating from the light vector mesons have momenta very close to those generated in Dalitz decays of π^0 and η mesons. To which extent those Dalitz electrons are contributing to the background for the light vector mesons and to which extent they can be removed within the current detector concept has been studied in a scenario with perfect particle identification (PERF). The available statistics was not sufficient to model the experimental analysis strategy of subtracting invariant mass spectra from mixed events from the combinatorial e^+e^- pairs within one event. Rather, the input information of the number of detected pairs from the same parent had to be used in order to determine the signal strength (magenta area in Fig. 32). Note also that the results represent the best case for the application of Dalitz rejection, misidentified pions will further enhance the background and cannot be rejected by correlation techniques.

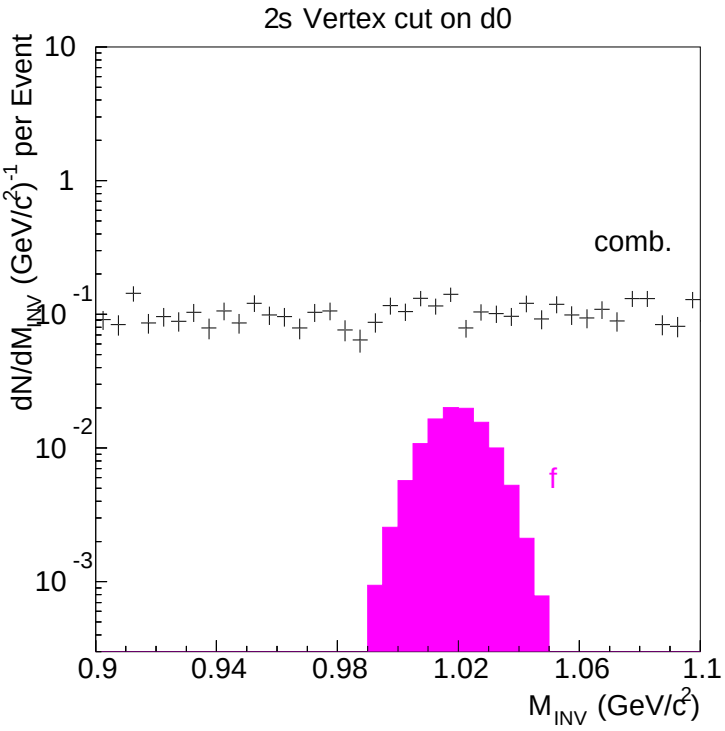

Figure 32: Invariant mass spectrum of e^+e^- pairs in the ϕ mass region. A p_t^{single} cut of 1 GeV/c is applied.

Dalitz strategies, as successfully implemented in current SPS experiments, try to remove those e^+e^- pairs that fulfill the kinematical criteria of this decay mode. Having found a Dalitz e^+e^- candidate pair, both electrons are removed from the sample before computing the invariant masses. Unfortunately, many of the electrons generated by Dalitz decays have momenta below 250 MeV/c, a threshold below which no particle identification is available within the studied detector scenarios.

The effect of those pairs detectable with momenta above 250 MeV/c is shown in Fig. 33 for an otherwise perfect detector environment. In Fig. 33 the most successful strategy that could be identified so far is used: the opening angle of the e^+e^- pairs (α_{DS}). The (relatively small) change of signal and the S/B ratio with opening angle demonstrate that removable Dalitz electrons have a minor influence on both quantities. Much more important are contributions from D and B mesons and the overall combinatorial background that is controlled by the lower transverse momentum cut-off. Increasing this lower cut-off value to 1 GeV/c increases the S/B ratio to about 10 % (Fig. 32) and allows the extraction of a signal, although within a restricted phase space. Typical expected signals and signal-to-background ratios including a $\pm 2\sigma$ cut on transverse and longitudinal impact parameter are given in Table 5 for the various detector scenarios. Signals are extrapolated to 10^7 central events (1/4 year of ALICE operation).

Conclusions:

1. Dalitz contributions are only part of the relevant background.

2. ϕ physics is doable only in restricted phase space (large p_t).

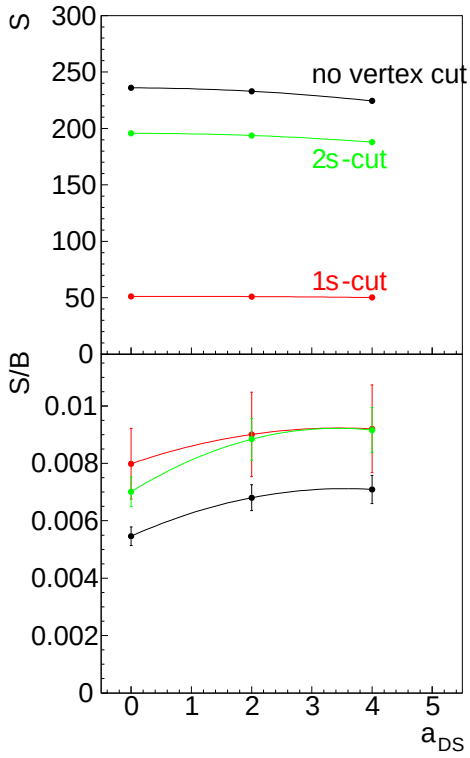

Figure 33: Signal and signal-to-background ratio for the ϕ mesons versus Dalitz opening angle cut in PERF scenario for an event sample of $5 \cdot 10^4$ central events. A lower single electron transverse momentum cut of $p_t > 0.5$ GeV/c was used for the final combinatorics. Pairs of e^+e^- with single transverse momenta $p_t > 0.25$ GeV/c and an opening angle of $\alpha < \alpha_{DS}$ were rejected. Results are shown for three different cuts on the transverse ($d0$) and longitudinal ($z0$) impact parameter of single tracks.

3. ω mesons can be detected with similar efficiencies as ϕ mesons.

4. ρ not yet studied, but probably hidden under background due to its large width.

4.4 Measurement of open charm and open beauty

Fig. 27 demonstrated that secondary vertices are populated according to particle species. Mesons with open charm and beauty are characteristically dominating the impact parameter distribution at values of $150 < d0 < 1000$ μm. These small distances are, due to the projected excellent performance of the Inner Tracker System of ALICE, measurable with the

	$p_t > 0.5$ GeV/c		$p_t > 1$ GeV/c	
Scenario	S (10^4)	S/B (%)	S (10^3)	S/B (%)
PERF	4.0	0.70	4.8	10.7
TPC2	3.2	0.03	4.5	0.2
TRD4	2.7	0.04	3.6	1.0
TRD2	2.7	0.08	3.6	6.4

Table 5: ϕ meson reconstruction efficiency and background contamination.

resolution plotted in Fig. 26. Having, in addition, the particle identification power of the TPC/TRD system allows to reconstruct impact parameter distributions for electron candidates.

A quantitative analysis of the signal and the signal-to-background ratio as function of the transverse impact parameter is shown in Fig. 34 for several lower transverse momentum cut-offs. Note that up to 10 electrons from D decays are found with a $p_t > 0.25$ GeV/c condition. Due to the variation of impact parameter resolution with p_t as shown in Fig. 26, a reasonable separation of the secondary vertices requires a cut of $p_t > 1$ GeV/c which still leaves about 0.15 D decays per event. At transverse impact parameter values of $d0 = 180$ μm a signal-to-total ratio of about 40% is extracted. Inspection of Fig. 27 allows the conclusion that the rest of the distribution is originating from semi-leptonic B decays.

Fig. 35 represents the same dependence for B mesons and shows saturation for the signal-to-total ratio value for large transverse impact parameter and large p_t. Large displaced vertex

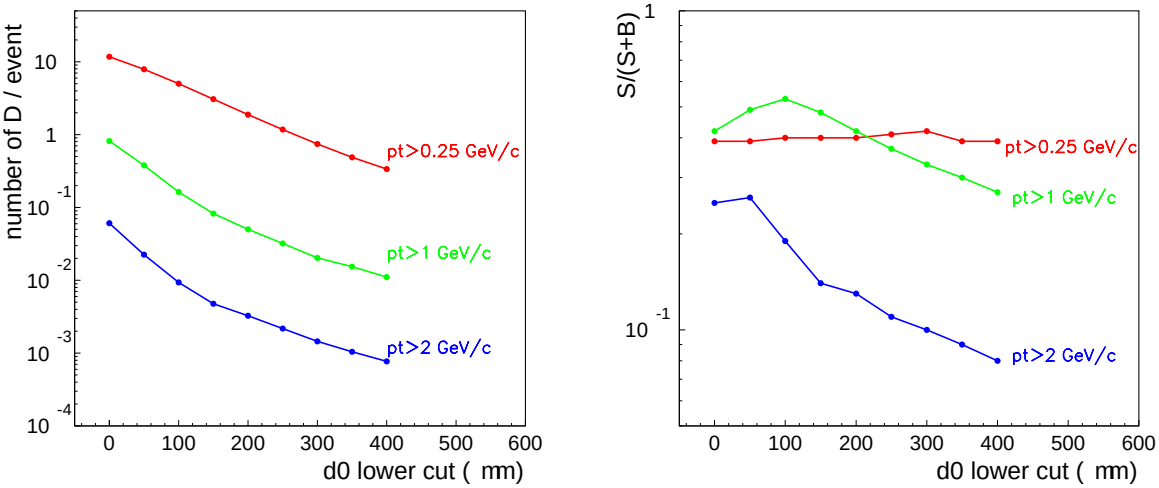

Figure 34: Signal and signal-to-background ratio for D mesons versus $d0$ lower cut.

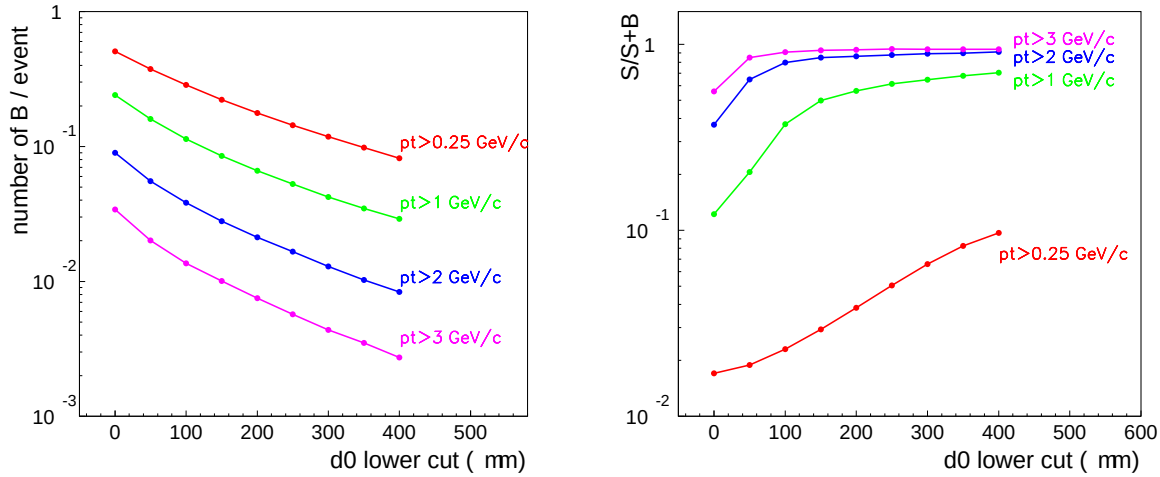

Figure 35: Signal and signal-to-background ratio for B mesons versus $d0$ lower cut.

distances are dominantly populated by large-p_t B mesons. Therefore, B meson production can be measured in an inclusive fashion. Since the B meson yield is largely unknown this information will be a necessary ingredient for the interpretation of the invariant mass spectra, especially in the continuum region.

The deconvolution of the $d0$ distributions and their p_t dependence will also allow to estimate the D meson yields, carrying an important physics information by themselves and being a substantial part of the continuum background. The correlation of the p_t of the electrons and their parents is quite strong, as shown in Fig. 36. This can be used to determine p_t spectra of D and B mesons.

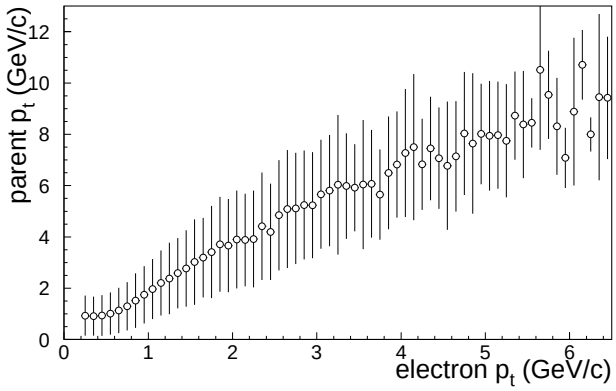

Figure 36: Correlation of electron p_t and parent p_t. The vertical bars represent the rms width of the distribution.

We have also investigated the importance of non-Gaussian tails due to single and plural scattering in the beam pipe and ITS. Due to the excellent electron identification of the TPC/TRD, the additional background originating from this effect is below 5 % and can be neglected.

Conclusions:

1. Secondary vertices can be exploited (making use of the ITS) in extracting an inclusive D and B meson yield.

2. The p_t dependence of the signal allows a deconvolution into D and B contributions and gives access to the primary p_t of D and B mesons.

3. Quantitative understanding of D and B yields is necessary before addressing quarkonia and continuum physics.

4.5 Measurement of J/Ψ from B meson decay

B mesons decay into J/Ψ mesons with a branching ratio of about 1%. Since B mesons are produced by a factor of 5 more abundantly than J/Ψ mesons, and since direct J/Ψ production might be further suppressed by QGP effects, secondary J/Ψ mesons are conceivably contributing a large fraction to the observable J/Ψ signal especially at large p_t (see also Section 1).

The impact parameter measurement with the ITS and the particle identification by the TPC/TRD allows to reconstruct the vertex of all e^+e^- pairs. Gating on large transverse

impact parameter and thus exclusively on electrons from B mesons results in the invariant mass spectrum shown in Fig. 37. A peak of secondary J/Ψ's is clearly visible with a

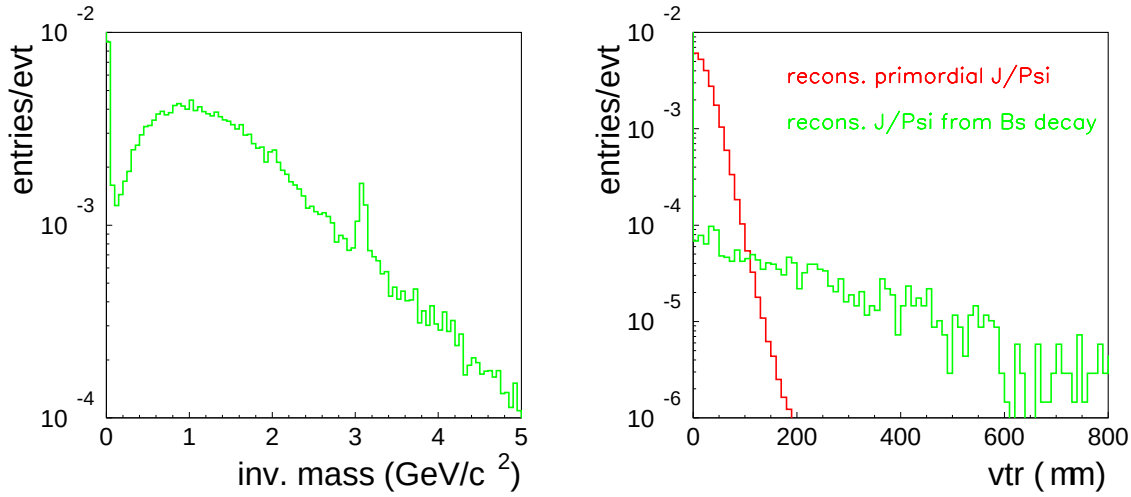

Figure 37: Invariant mass distribution of pairs with displaced vertices (left panel) and distance to primary vertex dependence of the J/Ψ signal (right panel). The secondary vertex distribution can be used to correct the J/Ψ signal originating from the primary vertex. With the open charm yields used in the current simulation this contribution amounts to 10%.

signal-to-background ratio of 3:1. Selecting pairs near the J/Ψ mass peak gives rise to the vertex distribution shown in the right side of Fig. 37. An exponential distribution is observed and will allow to experimentally establish the secondary J/Ψ yield. The simulation allows to deconvolute the vertex distribution even for the primary vertex and proves that the extrapolation method works.

With the multiplicities described in the introduction the ratio J/Ψ (primary) to J/Ψ (secondary) is 4:1 integrating over all $d0$ values. This yields a ratio of 10:1 within the primary vertex resolution that can be determined by extrapolating the measured secondary vertex distribution for J/Ψ. As discussed earlier, the uncertainty of open charm and open bottom production is very high. Without identifying the secondary J/Ψ's the signal of J/Ψ suppression in the QGP might be lost, since secondary decays could easily fill in on a few times 10% level. The identification and reconstruction of secondary J/Ψ mesons is even more important for the p_t dependence of the J/Ψ signal, since J/Ψ from B meson decays exhibit a much harder transverse momentum spectrum than the primary one. At large transverse momentum the ratio of primary to secondary J/Ψ can grow as large as 1:1. A trustworthy physics interpretation can clearly only be given once the secondary contribution is quantitatively known.

Conclusions:

1. The J/Ψ signal has to be corrected for secondary J/Ψ's.

2. Extrapolating the secondary vertex distributions for the J/Ψ signal allows to quantitatively determine the contribution to the primary yield.

4.6 Contribution of the muon channel

The results presented in previous sections were obtained by considering only the electron channel for the decay of particles. However, a large amount of muons are produced at the same time. In order to evaluate the contribution of the misidentified muons to the signal of B and D mesons a study was made including this channel in the simulation. As the mass of the muons is close to the one of the pions, the muons were treated in the same way as the pions, in terms of resolution and rejection in TPC/TRD. With a p_t cut of 1 GeV/c most of the misidentified muons are coming from open charm and open bottom decay. As shown in Table 6 the fraction of misidentified muons in the signal of both D and B mesons is very low (of the order of 1% with the identification performances of TPC alone). The introduction of the TRD allows to suppress this fraction down to 0.2%. According to these estimations one can conclude that the results on open charm and open bottom presented in the previous section will not be affected by the presence of misidentified muons.

$p_t > 1$GeV/c		nr. of part./evt	frac. of electron	frac. of mis.id. π	frac. of mis.id μ
B's	TPC	0.24	0.91	0.075	0.015
	TRD3	0.20	0.99	0.008	0.002
D's	TPC	0.86	0.85	0.14	0.01
	TRD3	0.68	0.973	0.025	0.002

Table 6: Fraction of electrons, misidentified pions and muons in TPC and TRD3 for B and D meson signal.

4.7 The di-electron continuum

The continuum in the invariant mass spectrum between J/Ψ and Υ (Fig. 28) carries contributions from very interesting processes, e.g. thermal plasma radiation and direct production (Drell-Yan). While the thermal radiation depends strongly on the initial conditions and the lifetime of the plasma and, therefore, has a very large uncertainty with the present understanding of the reaction mechanism, Drell-Yan production can be predicted (semi-) quantitatively and can be used as a reference for the extraction of continuum physics.

To address continuum dilepton physics the combinatorial background must be reduced as much as possible. After applying best particle identification cuts and cuts on the impact parameter to select tracks from the primary vertex there is only one remaining tool: the lower transverse momentum cut-off that is used for all single electrons, before pairs are built and the invariant masses are reconstructed. Once the average number of electron candidates is substantially below one electron per event the combinatorial background should be strongly reduced. This happens at rather large p_t values. As an example Fig. 38 displays the situation with a p_t cut-off of 3 GeV/c as obtained with the currently available statistics of 10^5 events. Particle identification was assumed to be perfect and a vertex cut at the $\pm 1\sigma$ level was applied. Even with these rather extreme cuts the combinatorial background extracted from a mixed event analysis to reduce the statistical fluctuations exceeds the Drell-Yan signal by an order of magnitude. Following common wisdom, a signal-to-background ratio of 1:10, however, seems to be manageable provided there are enough events to do a proper mixing

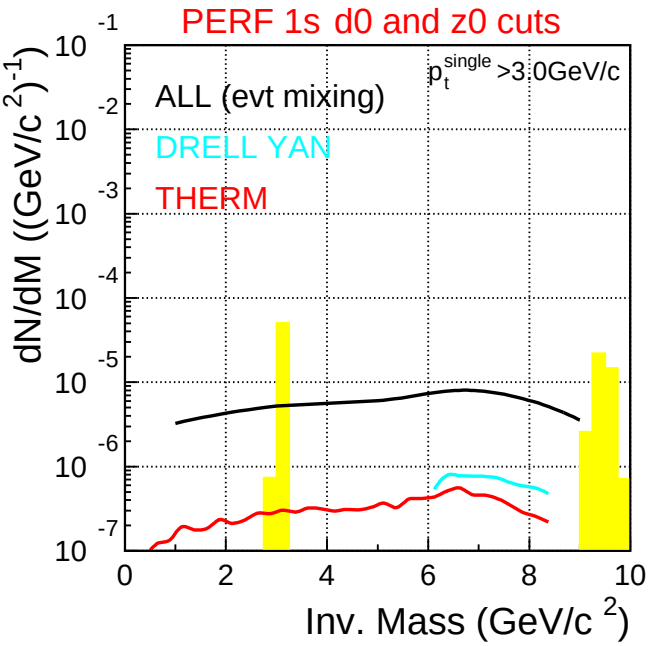

Figure 38: Invariant mass spectrum for e^+e^- pairs with single leg momenta larger than 3 GeV/c. Prediction for Drell-Yan and thermal radiation are given.

analysis. Therefore, a serious attempt for continuum physics defines strong requirements for a dilepton trigger.

As already stated in the introduction, the yield of thermal photons produced in the QGP phase is too uncertain to base any detector design on presently available predictions. Nevertheless, it is interesting to observe that, within certain scenarios [36], the yield of thermally produced photons is close to the Drell-Yan level. In that sense Drell-Yan production of virtual photons can be considered to be a well defined reference for dilepton continuum physics.

Summarizing this subsection, dilepton continuum physics at large p_t requires the best possible particle identification, optimum vertex resolution, and a dilepton trigger. With these tools at hand a signal-to-background ratio of 1:10 is estimated for Drell-Yan production. Certainly, further high statistics simulations are necessary to consolidate this finding.

4.8 Electron-muon coincidence measurements

Heavy mesons decay into e+X or μ+X with a branching ratio of ~12% for charm and ~10% for bottom. Therefore the complete ALICE device should allow to estimate correlated $D\bar{D}$ and $B\bar{B}$ cross-sections from electron-muon coincidence measurements. This consists in reconstructing unlike-sign electron-muon pairs where the electron is identified in the central part of ALICE and the muon is detected in the forward muon spectrometer. The signal then corresponds to unlike-sign electron-muon pairs where the electron and the muon arise from the decay of the two mesons of the same pair. Note that as compared to e^+e^- and $\mu^+\mu^-$ channels, the $e\mu$ channel gives a direct access to correlated $D\bar{D}$ and $B\bar{B}$ since neither the thermal radiation nor the Drell-Yan mechanism can provide correlated $e\mu$ pairs. This type of measurement has already been performed successfully in p+p reactions at $\sqrt{s} = 60$ GeV [37] and is planned to be done in heavy ion collisions with the PHENIX detector at RHIC [13].

Following the ideas from [38], fast simulations have been performed in order to estimate the capabilities of ALICE to measure $e\mu$ coincidence. We start by generating 10^5 (resp.

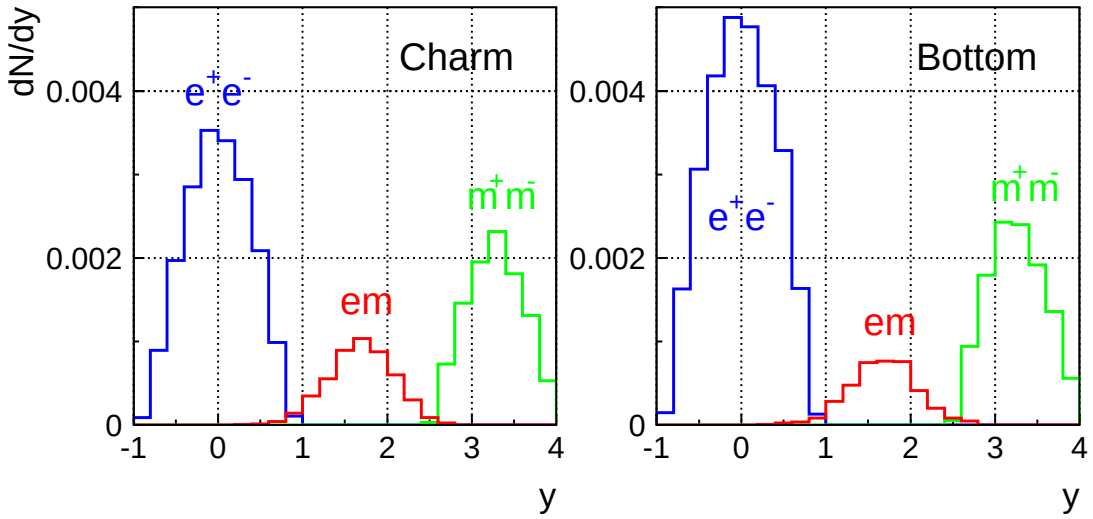

Figure 39: Rapidity distributions of correlated lepton pairs from charm (left) and bottom (right). The ALICE acceptance cuts described in the text are applied. The histograms are normalized to one Pb+Pb central event. The eμ spectra include both $e^+\mu^-$ and $e^-\mu^+$ components.

10^6) central Pb+Pb $\rightarrow$ c$\bar{\text{c}}$ (resp. b$\bar{\text{b}}$) by means of $10^5 \times 540$ (resp. $10^6 \times 7$) p + p $\rightarrow$ c$\bar{\text{c}}$ (resp. b$\bar{\text{b}}$) events computed with PYTHIA 5.7 [39]. This assumes that a Pb+Pb event is a superposition of a certain number of p + p events. The number of heavy quark pairs per event is obtained from PYTHIA predictions (using the MRSD-'1 parton distribution function) for p + p reactions at $\sqrt{s} = 5.5$ TeV and then extrapolated to central Pb+Pb events. Heavy quarks are then hadronized through a Peterson fragmentation function into heavy mesons which are decayed with JETSET 6.4. Energy losses of heavy quarks and rescattering effects of heavy mesons in the parton medium are neglected. In the last stage, the ALICE angular acceptance cuts are applied, i.e. we keep muons emitted with $2^\circ < \Theta_\mu < 9^\circ$ and electrons with $45^\circ < \Theta_e < 135^\circ$. In addition, a p_t threshold of 1 GeV/c is applied to both muons and electrons. The number of correlated eμ pairs per event after decays and cuts is about $1 \cdot 10^{-3}$ and $8 \cdot 10^{-4}$ for charm and bottom, respectively. Fig. 39 shows the rapidity distribution of these eμ pairs together with the ones of correlated e^+e^- and $\mu^+\mu^-$ pairs. It can be observed that the eμ pair rapidity distribution sits in a region located between the ones covered by e^+e^- and $\mu^+\mu^-$ pairs. Therefore the eμ channel would provide with a relatively high statistics i) an independent estimation of D$\bar{\text{D}}$ and B$\bar{\text{B}}$ cross-sections, and ii) a nice overlap between the central part and the forward part of ALICE rapidity coverage.

The dominant source of background to this signal comes from the non-correlated eμ pairs from charm and bottom. This is due to the relatively high number of c$\bar{\text{c}}$ and b$\bar{\text{b}}$ pairs per event. Fig. 40 shows the eμ signal and 1/(signal/background) as a function of a p_t threshold on the electron and muon of the pair. The additional cut $|\Delta\Phi| > 90^\circ$, where $\Delta\Phi$ denotes the difference in azimuthal angle between the leptons of the pair, was applied. This cut is motivated by the fact that the leptons from a correlated pair are strongly emitted back-to-back compared to the non-correlated lepton pairs whose $\Delta\Phi$ distribution is flat. Therefore applying $|\Delta\Phi| > 90^\circ$ allows to reduce the combinatorial background by a factor of 2 with essentially no loss of signal. It can be observed that a p_t threshold of 1 GeV/c on both legs of the pair leads to a very large signal ($\sim 40 \cdot 10^3$). On the other hand, since this signal does not appear in a narrow peak but it is spread over several GeV/c^2 in the invariant mass, the corresponding S/B of about 1/250 is definitively too low to extract any relevant information.

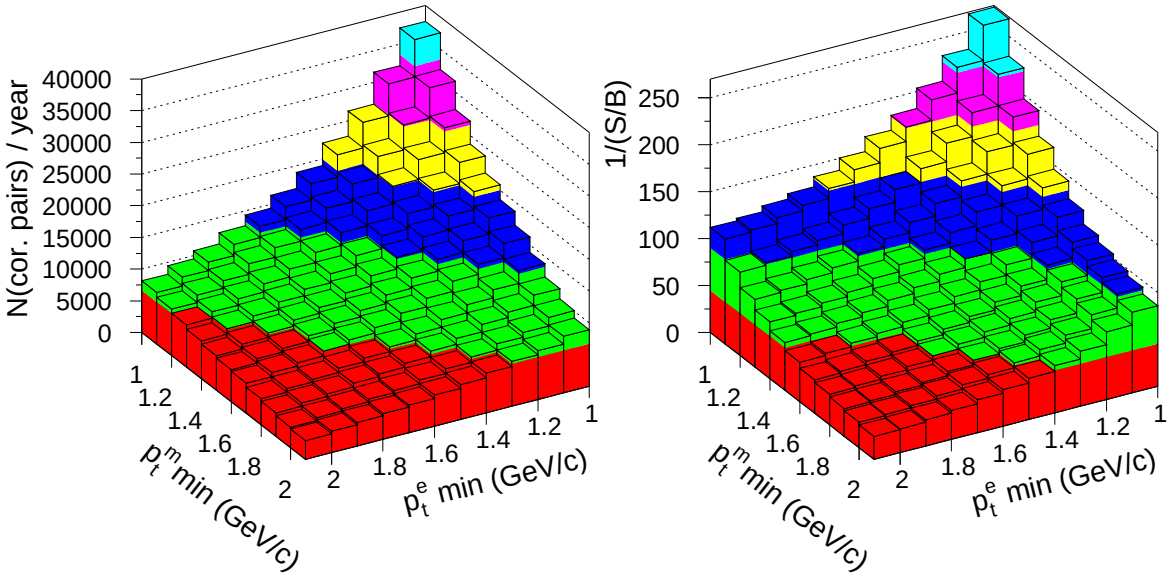

Figure 40: Number of correlated eμ pairs per year (left) and $1/(S/B)$ (right) as a function of p_{t} threshold on electron and muon. Only electrons and muons coming from D mesons decay are considered. Signal and background were extracted by integrating the eμ yield over the full invariant mass range. The signal was extrapolated to one year of ALICE running assuming a central event rate of 40 Hz and one month of heavy ion data taking.

Cutting stronger in p_{t} improves the situation drastically and with a p_{t} threshold of 2 GeV/c one would obtain $\sim$ 5000 correlated eμ pairs with a S/B of about 1/25. Similar conclusions are obtained for eμ pairs from bottom decay.

Fig.40 represents an ideal situation since the combinatorial background does not include electrons and muons from bottom decay and from other sources such as π^0 Dalitz and $\pi^{\pm}$, $\mathrm{K}^{\pm}$ decays. However, one could in principle disentangle charm and bottom contributions to the total eμ yield by using lower and upper cuts on the eμ invariant mass and/or on single leg lepton transverse momentum. On the other hand, with a 2 GeV/c p_{t} threshold on both electron and muon the background from π and K decays amounts to a S/B of $\sim$1/50. This can be improved for instance by rejecting electrons from π^0 Dalitz decays with an appropriate cutting strategy as described in Section 4.3, and by selecting large $d0$ impact parameters as described in Section 4.4. After further cuts and a like-sign subtraction, the eμ signal from correlated D$\bar{\mathrm{D}}$ and/or B$\bar{\mathrm{B}}$ should be visible.

4.9 Event rates

The feasibility of dilepton physics with ALICE depends on the total event rates that can be achieved. As outlined above, the most demanding requirements are obtained for the large invariant mass pairs, as, for example, the ones originating from Υ decays. The primary rates obtained for various centrality classes are summarized in Table 7.

The measurable rate R is given by folding in the geometrical efficiency for electron pairs ϵ_{geo} and the detection efficiency of single electrons ϵ_{det}: $R = \mathrm{d}N/\mathrm{d}y \cdot \epsilon_{geo} \cdot \epsilon_{det}$. The geometrical efficiency $\epsilon_{geo} = N^{acc}_{\mathrm{e^+e^-}}/(\mathrm{d}N/\mathrm{d}y)$ was determined by the Monte Carlo simulations to be $\epsilon_{geo} = 0.65$. The detector efficiency ϵ_{det} is the product of the single electron efficiencies (0.9) multiplied with the effective solid angle and amounts to $\epsilon_{det} = 0.75$.

Assuming that with a data taking rate of 40 Hz $4 \cdot 10^7$ events can be taken with a year of

Event class	$\sigma/\sigma_{geo}(\%)$	$\mathrm{d}N/\mathrm{d}y(\Upsilon \to \mathrm{e}^+\mathrm{e}^-)$
b=0	0	$7.4 \cdot 10^{-5}$
Highly Central	3	$6.4 \cdot 10^{-5}$
Central	10	$5.3 \cdot 10^{-5}$
Minimum Bias	100	$1.54 \cdot 10^{-5}$

Table 7: Υ production rates.

Event class	$\sigma/\sigma_{geo}(\%)$	untriggered	triggered
Highly Central	3	1240	1700
Central	10	1040	4680
Minimum Bias	100	300	13500

Table 8: Number of $\mathrm{e}^+\mathrm{e}^-$ pairs from Υ decay. These numbers include an 81% electron pair efficiency and a geometrical acceptance factor of 93% due to dead areas. An additional efficiency factor of approximately 80%, expected due to the performance of the trigger in the high multiplicity environment (see Section 6.2), is not included.

ALICE operations (10^6 s), the total number of Υ's in the event samples can be calculated. An event sample of $4 \cdot 10^7$ highly central events would contain 1240 $\mathrm{e}^+\mathrm{e}^-$ pairs from Υ decay. This number reduces to about 300 when the detector would be running in minimum bias mode only (see Table 8).

The low rates can be cured by implementing an $\mathrm{e}^+\mathrm{e}^-$ trigger. The event rates of the different event classes are listed in Table 9 for a luminosity of $L = 5 \cdot 10^{26}$ cm^{-2} s^{-1} and an interaction cross section of $\sigma^{\mathrm{PbPb}} = 8$ b.

The ratio of the primary Υ rates to the DAQ rate gives the maximum enhancement that can be obtained by the implementation of a dedicated trigger. The resulting total numbers are shown in the column labeled "triggered" in Table 8. With several thousand events containing Υ mesons a physics analysis along the lines of present J/Ψ studies will be doable.

The TRD as envisioned in this proposal covers the full TPC acceptance. Under the current ALICE funding scenario approximately 1/2 of this detector is funded. The physics which can be addressed with such a reduced size detector is still rich and will be an important part of the ALICE program but several of the rarer signals such as Υ and high p_{t} J/Ψ production as well as the thermal continuum cannot be studied anymore with significant precision. This is illustrated in Table 10. Note that all yields for J/Ψ and Υ production do not include any suppression factors as are expected for the LHC fireball scenario. The quoted numbers for the minimum bias measurement with an Υ trigger include the 80% trigger efficiency discussed above.

Level	Rate (Hz)
Min Bias	4000
Clean MinBias (Before/After Protection)	1800
Clean Central	180
Clean Highly Central	55
DAQ	40

Table 9: Rates for various event classes.

Process	Cut	$N_{full-size}$	$N_{half-size}$
Φ, central	$P_t^{single} \geq 1$ GeV/c	$2.2 \cdot 10^4$	$9 \cdot 10^3$
J/Ψ, central	$P_t^{single} \geq 1$ GeV/c	$3.3 \cdot 10^5$	$1 \cdot 10^5$
J/Ψ, central	$P_t^{single} \geq 0.8$ GeV/c $P_t^{pair} \geq 3$ GeV/c	$3 \cdot 10^4$	$9 \cdot 10^3$
Υ, central	$P_t^{single} \geq 3$ GeV/c	1240	360
Υ, min-bias triggered	$P_t^{single} \geq 3$ GeV/c	10880	3100
D $\rightarrow$ e	$P_t^{single} \geq 1$ GeV/c $d_0 > 150$ μm	$2.5 \cdot 10^6$	$1.5 \cdot 10^6$
B $\rightarrow$ e	$P_t^{single} \geq 3$ GeV/c $d_0 > 150$ μm	$4 \cdot 10^5$	$2.5 \cdot 10^5$
B $\rightarrow$ J/Ψ	$P_t^{single} \geq 1$ GeV/c	$4 \cdot 10^4$	$1.4 \cdot 10^4$
Thermal Continuum	$P_t^{single} \geq 3$ GeV/c $4 \leq m_{ee} \leq 6$ GeV/c^2	100	33

Table 10: Comparison of expected yields in full size and half size detector. All yields are for $5 \cdot 10^7$ events.

5 Electronics and readout

5.1 Signal processing and general layout

The signal collected by each readout channel is digitized and signal processing is based mainly on the hit position determined by the charge sharing ratio of a track segment. This is done on a per time bucket basis.

The choice of this method is natural, since the measurement of several energy deposition clusters along the track in each TRD layer enhances the track identification capability of the detector. Moreover, information on the correlation between the cluster energies and drift times is obtained, thus allowing a better pion rejection because of the difference in the patterns of energy deposition by TR photons and primary ionization.

The overall electronics chain, as it is considered now, includes a preamplifier and shaping amplifier, an ADC, and data processing and transmission components. The structure, as detailed below and in Section 6, will accommodate the need for an advanced trigger. The integration into the ALICE DAQ system requires, if any, minor modifications of the overall readout system and will make as much as possible use of the design elements adopted by the various ALICE sub-detectors. Accordingly, the design of the TRD electronics chain should greatly benefit from the R&D progress achieved so far. Basic target parameters of the system are summarized in Table 11.

Item	Value
No. of channels	1200,000
No. of samples/channel	30
Sampling rate	15-20 MHz
Shaping time	50-80 ns
ADC range	8 bits
FEE power consumption	60-80 mW/ch
Total data volume	36 Mbyte
- after zero-suppression	3-8 Mbyte

Table 11: Electronics parameters.

5.2 Sampling

Energy deposition from the TR photon is initially localized within a small spot of 1-2 mm. Diffusion of the electrons after a drift path of 1-3 cm in the Xe-rich gas will slightly increase the longitudinal size of the cluster but the charge will still be effectively localized within 2 mm. If the total drift time is sampled in 30 time buckets the particle tracks are recorded well enough to allow determination of position and angle of a given stiff track.

With a drift velocity of 15 mm/μs (refer to Section 3.5) a sampling frequency in the range of 15-20 MHz is adequate, and a shaping time in the range of 50-80 ns would match the width of the clusters and the digitization frequency range fairly well. Meeting these specifications does not present any unusual technological challenges.

5.3 Dynamic range and digitization accuracy

Transition radiation photons can have energies as high as 30 keV, which corresponds to about 1500 primary electrons being produced within a small region of 1-2 mm diameter[3]. Minimum ionizing particles (MIP) deposit, on average, about 10 keV along a 3 cm track within a TEC layer. Therefore TR photons can lead to clusters with a magnitude 50 times larger than a typical MIP cluster. Requiring the MIP cluster to be 20 times above threshold results in a dynamic range requirement of 10 bits.

However, for the position and angle determination of a minimum ionizing particle track 8 bits are sufficient. Furthermore, 8-bit ADCs are significantly cheaper than 10 bit ADCs. On the other hand a potentially very high TR photon peak shall be measured without overflowing the ADC. The proposed implementation uses a preamplifier with a dynamic range of 10 bits and two gains. If the high-gain part of the preamplifier reaches its maximum the output of the lower gain stage will determine the preamplifiers output. This can be realized for example by using an analog multiplexer selecting the appropriate internal amplifier stage. Which gain mode was selected at any time bucket is indicated by a specific digital output signal for each channel. The gain ratio between high-gain and low gain shall be 4. The advantage of this method is a linear ADC response allowing to calculate the $r\phi$ position of any hit using charge sharing ratios without the requirement of any non-linearity corrections.

For particle identification purposes, the requirements for the digitization accuracy are not very stringent. A precision at the level of about several percent is adequate. Therefore an 8-bit ADC is sufficient here.

We plan to test the first TRD prototype with a read-out system using an 8-bit ADC with 100 MHz frequency. The final design of the digitization system will be made taking into account the results of the tests.

5.4 Power consumption

The TRD material budget has to be kept as small as possible. Therefore, in order to minimize the material for cooling components, the power produced on the detector has to be minimized. It is important to have a preamplifier/shaper stage for each channel close to the corresponding pad. In order to be able to mass produce the electronics, 16 channels are grouped onto one multi chip module, where all chips are mounted as bare dies. Therefore the ADCs can be placed very close to the preamplifier, so that the driving requirements of the preamplifiers output stage can be kept small. We assume a power consumption of the preamplifier of about 10 mW/channel.

The technical development of fast low power 8-bit ADCs is very rapid as they are being used in mass markets such as mobile phones. One candidate, which is currently considered, requires an operating power of 40 mW at a digitization rate of 40 MHz. The ADC, however, has a power down mode, which could be utilized by using the fast pre-trigger. The wake-up time of this pipeline ADC corresponds to 2.5 clock cycles, which corresponds to about 70 ns latency, which would have to be counted into the pre-trigger latency. Whether powering the ADC on and off is feasible without introducing too large distortions into the analog front-end will have to be determined by further R&D. In the worst case the ADC would be kept continuously powered, resulting in a power consumption of about 40 mW. The power consumption stated in Table 11 assumes the ADC not being gated.

The digital tracking chip will implement a stand-by mode and thus contribute on average

[3]The range of a 20 keV electron in Xe at STP is 1.5 mm

very little to the total power consumption. The power needed during the 5 μs of the TRD electronics being active can be provided by appropriate capacitors, thus avoiding the requirement to have power cabling according to the worst power consumption. In addition, the power switching noise can be kept to a minimum.

The digital electronics, potentially including the ADC, will be idle in a stand-by mode until a fast pre-trigger wakes it up. One scenario would be to use an external multiplicity trigger, for example, based on scintillators. The total resulting latency of this pre-trigger will combine the decision-making period and some time for the electronics to become active. We expect that the total delay can be kept within 250 ns which corresponds to about 4 mm of the TEC drift length.

5.5 Cooling

The following factors determine the choice of the cooling method for the TRD front-end electronics: large overall amount of heat generated (up to 100 kW), large area from which the heat will have to be transferred, and relatively small, compared to the length of the detector, gap between the TRD layers. We intend to apply the system based on water cooling. The forced air cooling technique has also been considered for its obvious advantage of introducing no additional material within the TRD acceptance. Estimations have shown that effective cooling can not be achieved with such an approach without applying prohibitively high air pressure on the cathode planes of the gas chambers. Moreover, the configuration of the TRD and other ALICE subsystems makes it difficult to introduce an air supply duct of large cross-section required by the amount of air flow.

The water cooling will be free of these limitations and will provide effective cooling with relatively small amount of material. In order to maintain reasonably low temperature gradients of about 4° in the whole system, the total water flow rate close to 22 m^3/h is required. Water will enter the TRD from one end-cap side and will be collected into a discharge pipe on the other side of the detector. Additional lines, which are necessary to transfer water to the water pump and heat exchanger, will be designed in such a way that the overall pressure drop needed to recirculate water through the complete cooling system is minimized.

Each of the groups of 5 TEC, forming 108 planes, will be equipped with a pair of manifold pipes of 1 cm diameter running the water in z-direction. These pipes will serve as inlet and discharge ducts and will run down along the opposite sides of the chambers. The water flow between the two manifold pipes will be divided into an array of flat cooling pads about 1 m long running at constant z in 9 cm steps. We foresee that the packaging of the front-end electronics on the cathode boards of the gas chambers will be arranged in such a way that the heated components will be placed along straight lines, so that one cooling pad would remove the heat from 12-15 FEE cards depending on the width of the chamber.

Each pad will be made of a polyethylene mesh 1 mm thick welded in between two polyethylene sheets such that water would flow at moderate speeds through this sandwich. The pads can be made 1 cm wide, so that they cover about 10% of the total area. We estimate that average amount of material added by the cooling pads and the manifold pipes amounts to 0.07% per layer (see Table 2).

The current scheme foresees that after flowing through one plane of electronics the temperature rise of water will be about 4°. We estimate that in this case the heat produced by 15 FEE cards (up to 20 W) can be absorbed by water in one cooling pad with the water flow of 1.2 cm^3/s per pad. The flow is laminar, and the pressure required to force water through straight section of 1 m length is less than 0.02 bar.

The flow through the manifold pipes is about 56 cm^3/s per pipe, and even a diameter of 1 cm will not be large enough to preserve laminar flow conditions. The pressure drop for a turbulent flow in the straight 7 m long section of such conditions is about 0.06 bar. Taking into account the additional pressure drop due to the bends and fittings with contraction or enlargement transitions, we estimate that combined pressure drop required to force water through one plane is about 0.1 bar.

At the stage when individual TEC are assembled, the cooling pads and subsections of the manifold pipes will be pre-mounted, and input and output of the cooling pads will be welded to the manifold subsections. Later, during the installation of the complete TRD, the manifold subsections will be connected to each other to form integrated system.

6 Trigger

The TRD subsystem can be used to increase data accumulation rate for di-electron events by providing a trigger signature for high transverse momentum electron pairs where statistics under normal running conditions is marginal (see Table 8). The TRD allows to efficiently select events which contain electron-positron pairs with each of the leptons having a certain minimum transverse momentum, typically in the order of 3 GeV/c. Simulations along the lines discussed in Section 4 but including conversions show that 5% of central Pb+Pb events contain such a pair.

6.1 Trigger concept

The method to select high momentum electrons is based on the deflection of charged particles in the magnetic field. High momentum tracks have a small deflection with respect to a straight line pointing to the primary vertex in the transverse plane. Fig. 41 shows the typical deflections measured within one TRD readout chamber (TEC) versus the transverse momentum. Particles with a transverse momentum larger than 3 GeV/c are deflected by less than 1.5 mm from the straight line. The deflection is obtained from the tracks observed within a single TEC. A typical event is presented on the right hand side of Fig. 41, where the pulse height information from the FADC is shown for all pads within a pad row (of one readout chamber). The polar angle was chosen at 75°. Tracks are easily identified in this representation, especially when the occupancy is kept low. Fig. 41 corresponds to a pad size of 4.5 cm^2 (1.2 Mchannels).

The trigger scenario described below is designed to find all charged particle tracks with a certain limit on the deflection. It extracts the position, the angle and the average energy deposit for all stiff tracks and transfers this information to a track matching unit, where due

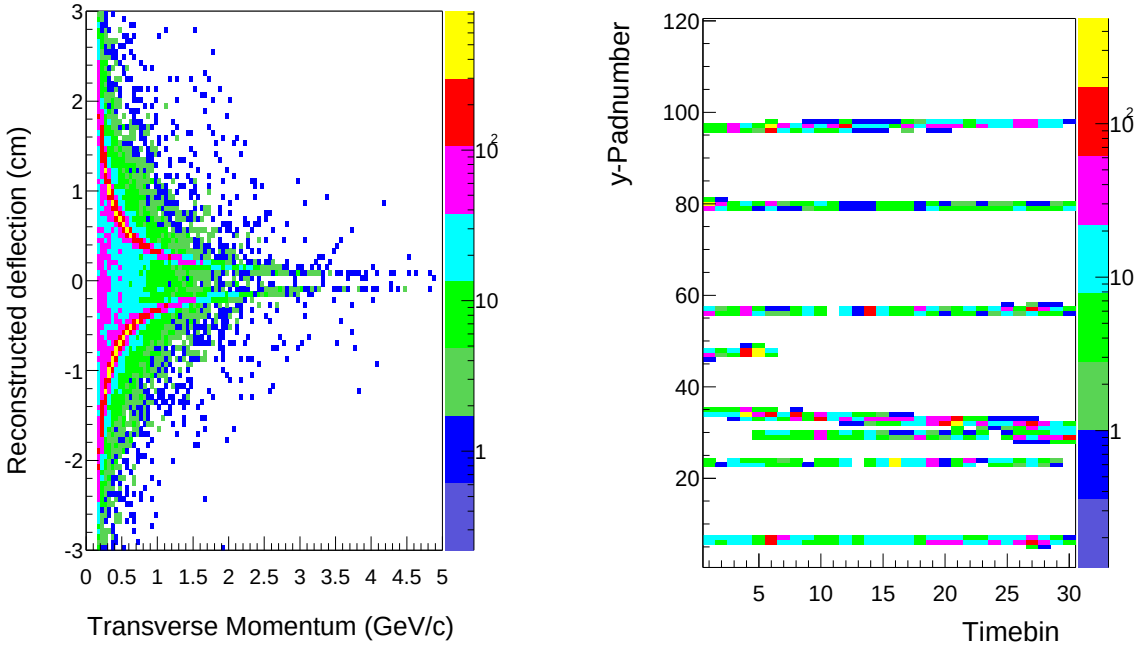

Figure 41: Reconstructed deflection versus transverse momentum (left) as obtained from digitized tracks (right).

to the spacing of the TRD layers, much larger deflections (1.8 cm for p_t = 3 GeV/c) are obtained and cuts can be applied on global deflection and energy deposit. A total reduction from $1.6{\cdot}10^4$ primary tracks per event to $1{\cdot}10^{-1}$ candidate per event is required to match the rates presented in Table 9.

6.2 Trigger performance simulation

In order to test the feasibility of a fast trigger derived from the TRD, a full scale Monte Carlo simulation (based on GEANT and AliRoot) has been performed for central Pb+Pb collisions including all background processes occurring in the detector material. The energy loss along the track was modeled taking into account the fluctuations [16] as discussed in Section 3.2. The charge was distributed onto the pads according to the pad response function for pads with the characteristics described in Section 3.5 and digitized with a resolution of 8 bit. Electronic noise of up to 1000 electrons per pad was found to be negligible since with the assumed gain and conversion factors it converts to 0.3 ADC channels.

Track finding was implemented by inspecting three neighboring pads centered around the primary peak at the entrance of the TEC. A position (in ϕ direction) was determined from charge sharing for each time bin and and used in a linear regression to obtain the inclination angle. The deflection is computed as difference of the straight line fit to the straight line from the initial incident point at the chamber to the interaction vertex, taken at the pad plane of the TEC.

The trigger tracking efficiency can be defined by the number of reconstructed tracks fulfilling the maximum deflection criterium divided by the number of primary tracks within the corresponding transverse momentum bin. Trigger tracking efficiencies of a single TRD layer obtained within this scenario are plotted in Fig. 42 for tracks with transverse momenta of more than 3 GeV/c. A maximum deflection of d_{max}=2 mm was used in the simulation. Two different granularities, corresponding to occupancies of 12% and 24% for central collisions (see Fig. 18) are shown as function of the secondary track multiplicity. Within the full simulation

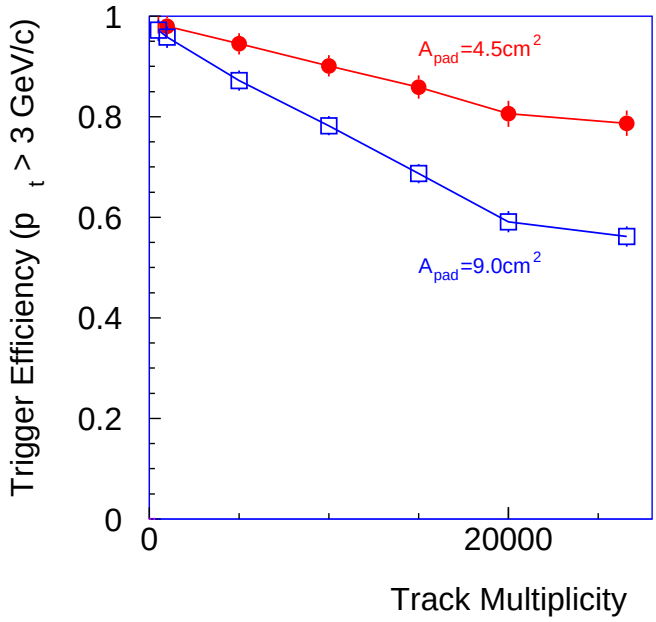

Figure 42: Trigger efficiency for high momentum tracks (p_t > 3 GeV/c) versus total track multiplicity.

a total of about 26000 tracks is produced for central collisions. Under these conditions for a pad size of $A_{pad} = 4.5$ cm^2 a tracking efficiency of 78% is achieved within a single layer, as compared to only 56% for half the granularity. This points to the necessity (as for the TR recognition, see Section 3.2) to keep the occupancy low in order to achieve an acceptable tracking efficiency. The efficiency is improving almost linearly when reducing the track multiplicity. This result was obtained by propagating only part of the primary tracks generated for Pb+Pb collisions through the detector material. For minimum bias Pb+Pb collisions the average multiplicity is about 13000 and single layer tracking efficiencies of 88% (74%) can be expected for pad sizes of $A_{pad} = 4.5$ (9.0) cm^2, respectively. For track multiplicities in the order of 1000, corresponding to the C+C collisions, values of 98% (96%) are obtained.

The suppression of low momentum fake tracks can be expressed by the selectivity of the trigger: out of 16000 primary tracks per event for central collisions, the algorithm described above recognizes about 10000 tracks, of which about 900 pass the maximum deflection limit of 2 mm. According to the simulations about 98% of these tracks still originate from (mostly) secondary low momentum particles scattered into the required direction. Those candidates can be quantitatively removed by the track matching units combining the information from different TRD layers and thus operating with longer lever arms. About 17 track candidates with $p_t > 3$ GeV/c remain per central collision that can be subjected to the transition radiation selection. According to the response studies presented in Section 3.2, a simple pulse height measurement allows for a pion suppression of 0.46 at the level of one layer.

The overall efficiency of finding electron tracks is given by requiring at least 4 matching track segments out of six layers. For a single layer efficiency of 78% in central Pb+Pb collisions this amounts to an overall efficiency of 88%. Note that for the reduced granularity of $A_{pad} = 9$ cm^2 one obtains an overall efficiency of 44%. With 4 available segments the pion background can be reduced by at least a factor of 22 resulting in a candidate finding probability of 0.39 per central collision for single high p_t electron tracks. Requiring pairs reduces the fake trigger rate to 0.15 per central collision while good pairs are accepted with an efficiency of 63%. The background rate can be further reduced by slightly decreasing the global deflection limit, e.g. increasing the transverse momentum threshold. For $p_t > 3.2$ (3.5) GeV/c background trigger probabilities of $9 \cdot 10^{-2}$ ($5 \cdot 10^{-2}$) are obtained. Another possibility to reduce the background trigger rate is to somewhat release the condition on electron efficiency that is currently kept at 90%. According to Fig.7 decreasing the electron efficiency from 0.9 to 0.85 results in an improvement of about a factor of 2 in the background rate at the expense of the true pair efficiency dropping from 63% to 56%.

With these numbers the trigger is close to the theoretical rates obtained from the nominal operation of the TRD (see Section 4.9). Further improvements are possible by refining the track finding and fitting algorithm. Especially a treatment of crossing tracks as possibly recognized by the width of the pad clusters should improve the track quality and the overall efficiency. Details need to be worked out in combination with the prototype developments of the chambers by properly modeling the response of the readout chambers.

6.3 Trigger implementation

As outlined in Section 4.8 pre-trigger rates of up to 1800 Hz are required, which exceed the capabilities of the TPC. Therefore the TRD has to operate as part of the L0 trigger system. A total time budget of 5.5 μs for the TRD L0 decision was assumed to be a tolerable loss for the TPC (about 7% of its active volume). This tight time budget requires most of the logic to be implemented as part of the on-detector components. Within each detector layer potential high p_t track candidates are selected by implementing an ϕ angle cut and shipped

to one out of 6 track matching stages.

The track parameters of the candidates fit into a 32-bit word ($r\phi$ position: 11 bits, corrected ϕ angle or displacement: 5 bits, z position: 6 bits, amplitude: 8 bits, and two bits of TR quality) are then transmitted by one link per detector to a track matching stage. At this point three track matching units, covering an azimuthal angle of 120° each, are assumed per detector side. They should be mounted on the end-caps as close as possible to the detector in order to minimize cable delays.

We expect that highly ionizing hadrons will be efficiently rejected by the p_t selection cut and only the hits from high p_t pions and electrons will pass the on-detector cuts. The optimal strategy of rejecting pion hits in each TRD layer while keeping high overall efficiency to electrons will be chosen after the prototype tests. For example, we can choose to operate with less than 90% electron efficiency within each TRD layer but require at least 4 out of 6 layers to provide information about the electron track. We anticipate that, in this case, significant pion suppression factor by individual TRD layers can be achieved. This will allow to reduce the number of candidates from misidentified pions.

The number of such candidates can be estimated based on the expected yield of high p_t charged particles per Pb+Pb central event, and the potential pion rejection capability by a single TRD layer. Simulations using the SHAKER+GALICE program show that, within the TRD acceptance, the number of charged particles with p_t exceeding 2.0, 2.5, and 3.0 GeV/c amounts to about 750, 250, and 150 respectively (dominated by pions). In the following we assume that 1000 track candidates will pass the on-detector cuts in each layer, which corresponds to 12 candidates per detector.

The data from each detector element can be trivially ordered in z/$r\phi$ so that a pipelined processing at the next stage can begin as soon as the first words arrive, thus reducing the overall latency. Fig. 43 shows the corresponding time line. Assuming a high maximum of 25 candidates per data-transfer link and event, each link would transmit up to 100 bytes per event to the TRD track matching unit. Assuming a data transmission time of about 1 μs this corresponds to a band width of 100 MB/s. This can be implemented for example as 8-bit bi-phase 50 MHz link. Note that this digital data transmission will occur during a time when the TRD detector is not active anymore and the TPC is not yet triggered.

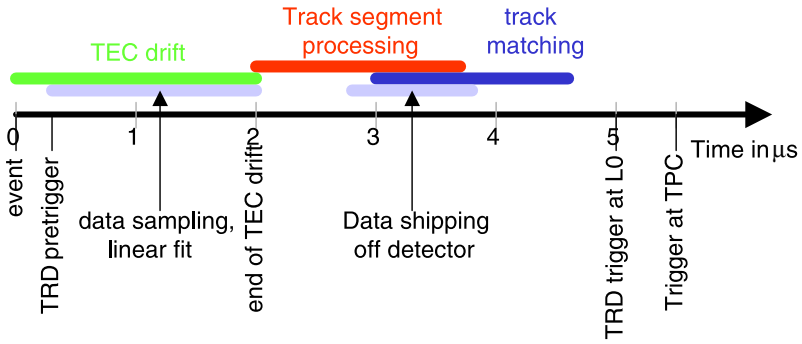

Figure 43: TRD time-line.

The architecture of the on-detector electronics is sketched in Fig. 44. The detector signals are amplified by a shaping preamplifier (refer to Section 5) and then digitized by a fast 8-bit ADC. The development of commercial, fast, 8-bit pipeline ADCs with low power consumption and power down functionality is driven by the increasing demand for hand held devices such as digital cameras and mobile telephones. During the past years the price-to-performance

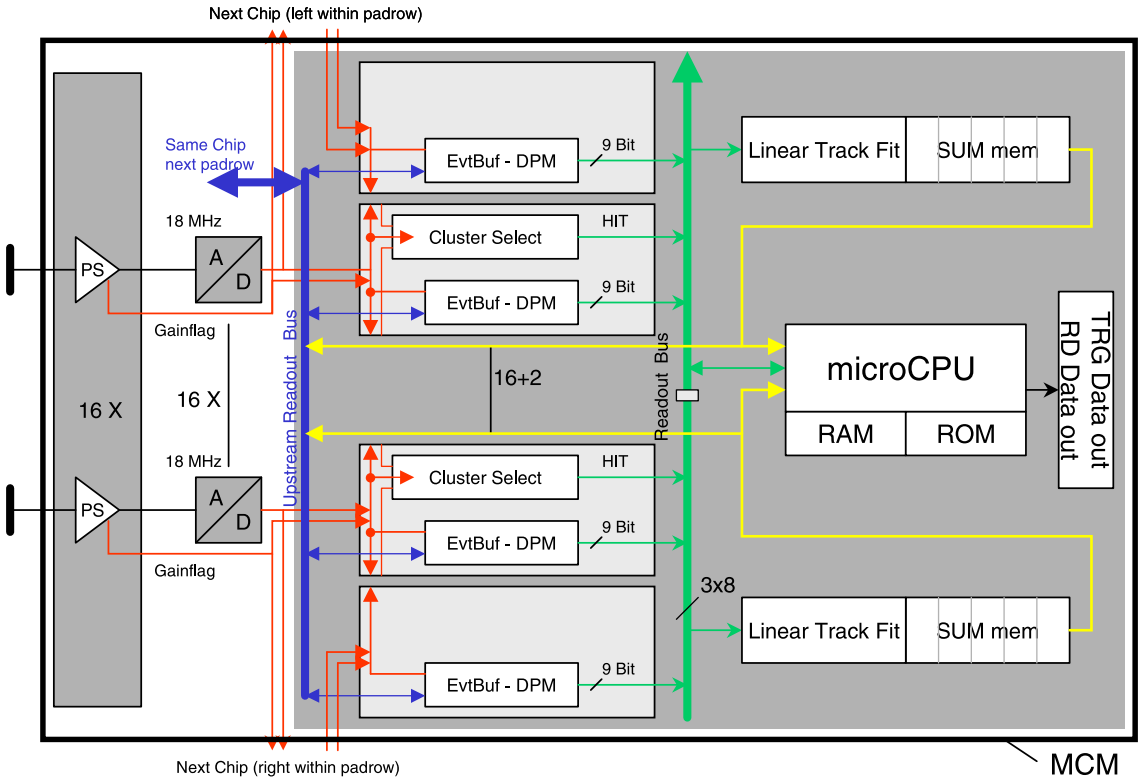

Figure 44: Functional blocks of the on-detector hit logic.

ratio has improved considerably. Therefore it appears logical to use a commercial ADC. The overall architecture of a device as sketched in Fig. 44 will be implemented as multi-chip-module (MCM), which can be mass produced. It is mounted on the detector using low profile mezzanine connectors like those used in portable computers for memory expansion modules. The ADC will have to be acquired as bare die. The advantage is that there will be no other logic on the detector except for slow control functionality. The digitized amplitudes are stored and processed by a digital custom chip, which is detailed below. The pin count of this digital chip can be kept relatively small by multiplexing multiple ADCs onto one internal digital readout bus. The MCM requires 16 ADC chips plus a 16 channel custom preamplifier and a custom digital processing chip. The MCM will implement separate power planes for digital and analog power. The layout can be chosen such that the digital and analog parts are well separated.

The digital processing chip performs two functions. First it searches for stiff or high p_t tracks and then it searches for TRD signatures at those identified tracks. However in order to keep a large degree of flexibility the overall architecture is chosen such that all stiff track candidates can be shipped to the TRD track matching stations. The actual track fitting and the selection of TR candidates is done by a programmable state machine labeled microCPU. A prototype design already exists that can be programmed in Java byte code. The same programmable unit can be used to perform intelligent readout of the detector, thus minimizing the data volume sent to DAQ.

The tracking both on the detector and in the track matching stations can be implemented relatively elegantly since all good tracks have to be stiff. Therefore the track candidates do not have to be searched like in case of the TPC. Every $r\phi$ hit position is determined due to the charge sharing ratio and then stored in an array corresponding to the appropriate pad.

If a track is very stiff all time buckets of this track should lie above one pad, resulting in a large number of hit positions being produced. The next step is to perform a straight line fit on those hits in order to determine the exact position and slope of the track (refer to Section 6.3.1). The resulting χ^2 and slope can be used to cut on good, stiff tracks. Tracks with a large $r\phi$ angle will cross over several pads and thus yield a small number of track candidates per pad. Bent tracks will yield a poor χ^2.

In order to have good fit quality not all hits are used towards the track fitting. Ideally all multi-hit clusters should be disregarded as the charge sharing ratio will yield a distorted position. Therefore some cuts are placed onto all hit candidates, trying to reject most bad clusters. First, the sum of three neighboring pads has to be larger than a certain threshold to guarantee a good signal-to-noise ratio. Second, the measured amplitude of the pad has to be larger than the amplitude of both of its neighbors. The functional block in Fig. 44 labeled `ClusterSelect` performs the quality cuts discussed above. Further algorithms are currently being investigated.

For any given track one pad takes at least 50% of the charge, which allows identification of the center pad of the three adjacent pads firing for a given track. On average 2.4 pads are hit by a track, and no more than three pads fire for any single hit cluster. A cluster can span over two readout chips but there is no more than one channel missing at any readout chip. Therefore, the first and the last channels are duplicated into two readout chips. This is indicated in Fig. 44 by the two additional Event Buffers, which are fed by the ADCs of the neighboring MCMs. Therefore in case of a cluster sitting right at the edge of this granularity one chip will see a single isolated channel firing and the other will have the whole cluster.

Towards the edge of the detector tracks have a polar angle of about 45°, and tracks may span over two pad rows. Therefore, it is necessary for the digital logic to be able to access the appropriate channels of the next pad row downstream. This is indicated in Fig. 44 by the bus labeled `UpstreamReadoutBus`. The implementation of the event buffer as dual ported memory grants full asynchronous access to the upstream node.

In order to keep the design as flexible and configurable as possible, a simple micro coded state machine will be used (labeled `microCPU` in Fig. 44) to calculate the various parameters and to implement the cuts. It could be run at 2-3 times the digitization speed and thus allow 100-200 operations during a 2 μs interval. The advantage of this approach is twofold. First, the trigger can be kept fairly simple. Further, the actual trigger algorithm can be adopted and modified even during the run time. Finally, once a trigger is generated, the same state machine, if designed appropriately, could be used to perform an intelligent readout of the data so that the detector will produce calibrated positions, angles and amplitudes.

The readout logic of the event buffers is designed such that the pre-selected group of three pads can be addressed relative to the center pad (address -1,0,1). This avoids the requirement for any searching or table lookup functionality. In other words, any further processing of the signal will only address three pads (-1,0,1) and the pre-selection logic will automatically refer to the appropriate channels. In order to determine an absolute detector coordinate some Control and Status Register space will provide the actual channel ID of the TR track candidate.

It is foreseen to have three TRD track matching stations at each end of the detector, each covering an azimuthal angle of 120°. Consequently, the outputs of all TEC detectors are fed into six tracking units which are mounted on the end-caps. This allows to keep all cables shorter than 8 m. The signaling can be done using a technique which implements low-power high-speed differential transmission up to 400 Mbit/s (LVDS, IEEE 1596.5). This trigger stage, where tracks are determined from the pre-selected hit candidates, can be implemented

using field programmable gate arrays (FPGA, such as Xilinx). It matches the pre-selected tracks with TR signature requiring, e.g., at least 4 out of 6 detectors to have fired, and calculates a new $r\phi$ angle based on the longer leverage arm of 6 detector elements. Given the high selectivity of the on-detector electronics and the limited angle distribution we estimate that this processing can be done in about 1 μs.

The final coincidence condition, requiring the transfer of very few bits only, will be implemented in FPGAs also. These components will be located at a position to minimize overall cable length. It is therefore most likely going to be close to the ALICE L0 trigger system.

6.3.1 Linear fit implementation

The number of operations necessary to calculate the charge sharing ratios and the sums for the linear fit of at least 1-2 tracks would significantly exceed the available clock cycles. On the other hand, it would be relatively inaccurate to pre-select track candidates and then determine the angle of the track by just using two or three space points. This problem is even worse taking into account that due to energy loss fluctuations (refer to Fig. 5) not all hits of a good track have an adequate amplitude to determine a good position.

Fig. 45 sketches an algorithm allowing to perform a linear fit for all potential track candidates of any given group of 16 channels. The logic sketched here requires little silicon real estate. First, a good hit candidate is determined for each channel and time bin (`ClusterSelect`). Given the criteria defining a good hit there can be up to 8 candidates per group of 16 channels. On average there are 1.2 candidates. The pad space is broken up into two groups of 8 pads. Each group implements its own linear fit logic block. If there are multiple hits per time bin they are processed sequentially. About 3% of all cases will result in more than 4 hits per 16 channels. Therefore one implementation could be to run the linear fit logic at twice the digitization rate. First design studies indicate that this logic could run at clock rates up to 80 MHz. In this case all potential hits could be processed. The trade-offs here are higher clock rates and the corresponding risk of coupling of digital noise into the analog front-end, which is active during this time.

The digitized amplitudes are readout using three 8-bit buses. Dependent upon which pad is the center channel the three channels need to be rotated left or right in order to always have the center and left/right channels at the same output bus. This is sketched by the first functional block of Fig. 45. The next unit calculates the charge sharing ratio. Given the detector resolution of better 200 μm and the pad pitch of 10 mm, 5 bits plus sign are adequate to encode the hit position. The coordinate system here uses y as position along the pad row and x as drift direction. The index t denotes the time bin number.

The next stage calculates the individual sums for the linear fit. Note that the x position is simply the time bin number. Only three 5-bit multipliers are required here.

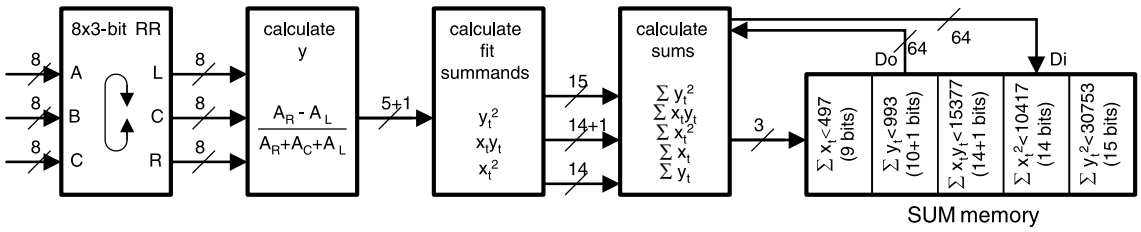

Figure 45: TRD linear fit implementation.

There are 5 sums required to allow calculating the straight line parameters and the χ^2. In the given case 64-bits are required to store all sums of the fit. These sums are accumulated for each pad and stored in a SUM memory as indicated. This is implemented by the last building block by using a 64-bit wide memory, which is addressed by the pad number. Since the memory has independent data in- and outputs a read-modify-write cycle can be easily implemented, which first reads the memory content and then stores the sum of the calculated parameters and the old memory content back into the same cell. Every time a summand is added to a pad an appropriate pad hit counter is incremented.

The functionality sketched here is performed during the drift time and thus concludes 2 μs after the interaction. Good track candidates are selected now by requiring the pad hit counter to be larger than a given threshold (e.g. 5-10). The remaining track parameters, which can be determined directly by the sums stored in the sum memory is now performed by the microCPU.

In order to determine the track parameters no more than 26 bits are required for the binary operations. To calculate the slope and straight line intersect a total of 4 multiply, 2 divide and 3 add operations are required. Note that those operations do not have to be executed sequentially but may be executed in parallel. The χ^2 is calculated only for stiff candidates with an appropriate cut on the maximum slope. In order to calculate the exact fit error 7 multiply, 5 add, and one shift operation is required.

6.3.2 Data acquisition

Once a TRD trigger is accepted the TPC is activated and thus there is a large amount of time available to the TRD for readout. The microCPU can easily perform this task, since no other triggers can be fired during that time. A zero suppressed TRD raw data event has a size of about 8 MB, i.e. less than 15 kB per detector module. Given a 100 MB/sec link, the data transmission would take 150 μs. The simplest implementation uses the now idling links to the TRD track matching stations, which implement some elasticity buffers and an up-stream link to DAQ. Taking into account a maximum trigger rate of 40 Hz the total aggregate zero suppressed data rate originating from the TRD is 40 MBytes/s, which can be easily shipped using one gigabit fiber per TRD tracking unit.

This data rate can be reduced considerably by transmitting track coordinates rather than raw data. For example a track can be encoded for readout in 48 bits: ($r\phi$ position: 12 bits, corrected ϕ angle or displacement: 7 bits plus sign, fit χ^2: 4 bits, z position: 6 bits, amplitude: 10 bits, generic quality flags: 5 bits, and two bits of TR quality). This corresponds to 270 bits of raw data or a reduction factor of five for every good track. This encoding could be used for tracks with very good fit quality only in order to avoid loosing information.

7 Budget

The overall cost estimate for the full TRD detector is shown in Table 12. This cost estimate is not generally based on firm quotes from industry. However, as can be seen from the table, much of the detector costs will be in electronics: to keep the occupancy low enough even for the highest foreseeable particle densities the full detector will have 1.2 M electronic channels. Therefore, considerable effort went into the specification of the electronics chain. Based on these specifications we have obtained preliminary price quotes from various industrial vendors which form the basis of the cost estimate. The cost of mechanical items is based on our experience with the recent building of similar components in experiment NA45. We note that the overall cost of the detector exceeds the currently available funds of 7 MCHF. If no additional funds can be secured then in the first stage we will build a TRD which is reduced in size such that the budget is commensurate with the available funds. This implies

DETECTOR		Price (kCHF)
Gas System		150
Gas (Xenon only, $24m^3$)		500
Radiator		560
Readout Chambers ($5 \times 18 \times 6 = 540$)		2750
ELECTRONICS		
Chip development and production	CHF per channel	
preamp	0.52	
pipeline ADC	< 2.0	
digital chip	0.6	
sum (based on 1.2Mch)		3750
FEE Boards	CHF per board	
board	4.3	
parts/fitting, front and back connector	10	
production	< 25	
sum (1.2M/16=80k)		3200
Motherboard	CHF	
board	315	
clock interface	100	
sum ($5 \times 18 \times 6 = 540$)		225
Link to trackfinder (540)		28
Trackfinder (2×3)		120
Link to DAQ		140
Cooling		200
Power supplies		
HV		40
LV		150
Slow control		
common part		50
on detector (Motherboard)		138
Prototyping		1000
SUM		13.000

Table 12: TRD cost estimate

cutting the detector size approximately in half. However, since the cost of some items such as detector prototyping and electronics will not vary linearly with size or number of channels in the detector, a careful optimization procedure has to be applied for such a solution.

We foresee an R&D stage of about 1 year, starting from May 1999, to define in detail all detector and electronics parameters. The prototype construction is well advanced and first in-beam tests of a TRD prototype including pad plane read-out and flash ADC electronics will take place at GSI in June of 1999. A Technical Design Report for the TRD should be finished in summer of 2000.

References

[1] Proposal to the LHCC, CERN/LHCC 95-71.

[2] Addendum 1 to the ALICE Proposal, CERN/LHCC 96-32.

[3] H. Appelshäuser et al., NA49 Collaboration, Phys. Rev. Lett. **82** (1999) 2471.

[4] L. Gerland, C. Spieles, M. Bleicher, H. Stöcker, C. Greiner, Proc. of the Winter Meeting on Nuclear Physics, January 1996, Bormio, Italy, nucl-th/9606001.

[5] R. Gavai, D. Kharzeev, H. Satz, G. A. Schuler, K. Sridhar, R. Vogt, Int. J. Mod. Phys. **A10** (1995) 3043.

[6] S. Gavin et al., Phys. Rev. **C54** (1996) 2606.

[7] P. Braun-Munzinger, A.Drees, D. Miśkowiec, C. Lourenço, Eur.Phys.J. **C1** (1998) 123.

[8] E. Scomparin et al., NA50 Collaboration, Strangeness in Quark Matter 98 Conference, Padova, July 20-24, 1998, http://www.cern.ch/NA50/papers.html.

[9] E. Shuryak, Phys.Rev. **C55** (1997) 961.

[10] Z. Lin, R. Vogt, X. N. Wang, Phys.Rev. **C57** (1998) 899.

[11] C. M. Ko, X. N. Wang, X. F. Zhang, nucl-th/9808032.

[12] P. Braun-Munzinger and K. Redlich, in preparation.

[13] PHENIX Collaboration, PHENIX Conceptual Design Report, BNL-48922, 1993.

[14] B. Dolgoshein, Nucl. Instr. and Meth. in Phys. Res. **A326** (1993) 434.

[15] W. W. M. Allison and J. H. Cobb, Ann. Rev. Nucl. Part. Sci. **30** (1980) 253.

[16] V. C. Ermilova et al., Nucl. Instr. and Meth. **145** (1977) 555.

[17] F. Lapique and F. Piuz, Nucl. Instr. and Meth. **175** (1980) 297.

[18] W. Blum and L. Rolandi, Particle Detection with Drift Chambers, Springer-Verlag, 1994

[19] C. Caso et al., Eur. Phys. J. **C3** (1998) 1.

[20] G. Bassompierre et al., Nucl. Instr. and Meth. in Phys. Res. **A411** (1999) 63.

[21] E. O'Brien et al., IEEE Trans. in Nucl. Sci. **40** (1993) 153.

[22] R. D. Appuhn et al., Nucl. Instr. and Meth. in Phys. Res. **A263** (1988) 309.

[23] M. Holder and H. Suhr, Nucl. Instr. and Meth. in Phys. Res. **263** (1988) 319.

[24] M. Clemen et al., Proc. of Symposium on Particle ID at High Luminosity Hadron Colliders, FNAL(1989), 339.

[25] K. Ackerstaff et al., Nucl. Instr. and Meth. in Phys. Res. **A416** (1998) 230.

[26] M. Castellano et al., Comp. Phys. Comm. **61** (1990) 395.

[27] R. Veenhof, GARFIELD, CERN Program Library entry W5050.

[28] S. F. Biagi, Nucl. Instr. and Meth. in Phys. Res. **A283** (1989) 716.

[29] F. Antinori, Internal Note ALICE 93–9.
N. van Eijndhoven et al., Internal Note ALICE 95–32.

[30] B. Yu et al., IEEE Trans. in Nucl. Sci. **38** (1991) 454.

[31] E. Mathieson et al., Nucl. Instr. and Meth. in Phys. Res. **A270** (1988) 602.

[32] R. Debbe et al., IEEE Trans. in Nucl. Sci. **37** (1990) 88.

[33] M. Richter, CERES TPC upgrade, private communication.

[34] E. O'Brien et al., Nucl. Phys. **A566** (1993) 615.

[35] V. Metag, π-N Newsletter 11 (1995) 159.

[36] K. Gallmeister et al., hep-ph/9809318.

[37] A. Chilingarov et al., Phys. Lett. B83 (1979) 136.

[38] Z. Lin and R. Vogt, hep-ph/9808214 and Nucl. Phys. **B544** (1999) 339.

[39] T. Sjöstrand, Comput. Phys. Commun. 82 (1994) 74,
http://www.thep.lu.se/tf2/staff/torbjorn/Pythia.html.